



**NAVAL
POSTGRADUATE
SCHOOL**

MONTEREY, CALIFORNIA

THESIS

**ANALYSIS OF SCIENCE ATTITUDES FOR K2 PLANET
HUNTER MISSION**

by

Eric S. Kinzbrunner

March 2015

Thesis Co-Advisors:

Mark Karpenko
James Luscombe

Second Reader:

Isaac M. Ross

Approved for public release; distribution is unlimited

THIS PAGE INTENTIONALLY LEFT BLANK

REPORT DOCUMENTATION PAGE

Form Approved OMB No. 0704-0188

Public reporting burden for this collection of information is estimated to average 1 hour per response, including the time for reviewing instruction, searching existing data sources, gathering and maintaining the data needed, and completing and reviewing the collection of information. Send comments regarding this burden estimate or any other aspect of this collection of information, including suggestions for reducing this burden, to Washington Headquarters Services, Directorate for Information Operations and Reports, 1215 Jefferson Davis Highway, Suite 1204, Arlington, VA 22202-4302, and to the Office of Management and Budget, Paperwork Reduction Project (0704-0188) Washington DC 20503.

1. AGENCY USE ONLY (<i>Leave blank</i>)	2. REPORT DATE March 2015	3. REPORT TYPE AND DATES COVERED Master's Thesis
4. TITLE AND SUBTITLE ANALYSIS OF SCIENCE ATTITUDES FOR K2 PLANET HUNTER MISSION		5. FUNDING NUMBERS
6. AUTHOR(S) Eric S. Kinzbrunner		
7. PERFORMING ORGANIZATION NAME(S) AND ADDRESS(ES) Naval Postgraduate School Monterey, CA 93943-5000		8. PERFORMING ORGANIZATION REPORT NUMBER
9. SPONSORING /MONITORING AGENCY NAME(S) AND ADDRESS(ES) N/A		10. SPONSORING/MONITORING AGENCY REPORT NUMBER

11. SUPPLEMENTARY NOTES The views expressed in this thesis are those of the author and do not reflect the official policy or position of the Department of Defense or the U.S. Government. IRB protocol number ____ N/A ____.

12a. DISTRIBUTION / AVAILABILITY STATEMENT Approved for public release; distribution is unlimited	12b. DISTRIBUTION CODE A
--	-----------------------------

13. ABSTRACT (maximum 200 words)

NASA designed the Kepler spacecraft to detect extrasolar planets, but after several successful years, with many new discoveries, two out of four reaction wheels failed. NASA repurposed Kepler to continue science under the new mission, K2. The physics of how Kepler detects planets, the transit method, is first described. As part of this description it is shown that pointing noise is the limiting factor of Kepler's ability to detect planets. The second part of this thesis uses a flat plate solar torque model of Kepler in order to assess the capabilities of the spacecraft in other "off ecliptic" attitudes. This analysis concluded that the controllability of the failed spacecraft in the presence of the solar torque is the main driver for the new K2 mission attitude and that conducting science out of ecliptic plane attitudes present challenges from the control point of view.

14. SUBJECT TERMS Kepler, solar torque, spacecraft, photometric precision, planet detection, K2, flat plate Kepler model, solar radiation pressure, star classification, transit method, planet definition		15. NUMBER OF PAGES 149	
16. PRICE CODE			
17. SECURITY CLASSIFICATION OF REPORT Unclassified	18. SECURITY CLASSIFICATION OF THIS PAGE Unclassified	19. SECURITY CLASSIFICATION OF ABSTRACT Unclassified	20. LIMITATION OF ABSTRACT UU

THIS PAGE INTENTIONALLY LEFT BLANK

Approved for public release; distribution is unlimited

ANALYSIS OF SCIENCE ATTITUDES FOR K2 PLANET HUNTER MISSION

Eric S. Kinzbrunner
Lieutenant, United States Navy
B.S., United States Naval Academy, 2005

Submitted in partial fulfillment of the
requirements for the degree of

**MASTER OF SCIENCE IN ASTRONAUTICAL ENGINEERING
and
MASTER OF SCIENCE IN PHYSICS**

from the

**NAVAL POSTGRADUATE SCHOOL
March 2015**

Author: Eric S. Kinzbrunner

Approved by: Mark Karpenko
Thesis Co-Advisor

James Luscombe
Thesis Co-Advisor

Isaac M. Ross
Second Reader

Garth Hobson
Chair, Department of Mechanical and Aerospace Engineering

Andres Larazza
Chair, Department of Physics

THIS PAGE INTENTIONALLY LEFT BLANK

ABSTRACT

NASA designed the Kepler spacecraft to detect extrasolar planets, but after several successful years, with many new discoveries, two out of four reaction wheels failed. NASA repurposed Kepler to continue science under the new mission, K2. The physics of how Kepler detects planets, the transit method, is first described. As part of this description it is shown that pointing noise is the limiting factor of Kepler's ability to detect planets. The second part of this thesis uses a flat plate solar torque model of Kepler in order to assess the capabilities of the spacecraft in other "off ecliptic" attitudes. This analysis concludes that the controllability of the failed spacecraft in the presence of the solar torque is the main driver for the new K2 mission attitude and that conducting science out of ecliptic plane attitudes present challenges from the control point of view.

THIS PAGE INTENTIONALLY LEFT BLANK

TABLE OF CONTENTS

I.	INTRODUCTION.....	1
A.	KEPLER MISSION AND SPACECRAFT	1
B.	THE K2 MISSION.....	10
C.	THESIS OBJECTIVE AND SCOPE	12
II.	PLANET HUNTING	15
A.	DEFINING A PLANET	15
1.	International Astronomical Union	15
2.	IAU Planet Definition	16
3.	Planet Definition Relevant to Kepler Mission	16
B.	STAR CLASSIFICATION	17
1.	Apparent Magnitude	17
2.	Absolute Magnitude.....	18
3.	Spectral Classification	19
4.	Apparent Magnitude and its Relevance to Kepler	22
C.	PLANET DETECTION METHODS.....	23
1.	Radial Velocity	25
2.	Astrometry	25
3.	Direct Imaging.....	25
4.	Gravitational Microlensing	25
5.	Transit Method.....	26
D.	SUMMARY	26
III.	THE TRANSIT METHOD FOR PLANET DETECTION	29
IV.	KEPLER SCIENCE REQUIREMENTS	33
A.	PHOTOMETRIC PRECISION REQUIREMENTS	33
B.	CCD SIGNAL.....	34
1.	PSF	34
2.	PRF	37
3.	Total Signal.....	37
C.	NOISE	38
1.	Signal Noise.....	38
a.	<i>Shot Noise</i>	38
b.	<i>Stellar Variability</i>	39
c.	<i>Summary</i>	39
2.	Instrument Noise.....	39
a.	<i>Read Noise and Dark Current Noise</i>	39
b.	<i>Pointing Noise</i>	40
c.	<i>Summary</i>	53
D.	ANALYSIS OF KEPLER'S NOISE FLOOR	53
1.	Case 1: Original Kepler Mission	53
a.	<i>Signal</i>	54
b.	<i>Shot Noise</i>	54

c.	<i>Stellar Variability</i>	54
d.	<i>Read Noise</i>	54
e.	<i>Dark Noise</i>	55
f.	<i>Pointing Noise and Pointing Requirements</i>	55
g.	<i>Total Noise and SNR</i>	56
h.	<i>Summary</i>	57
2.	Case 2: Original Estimates of ADCS Degradation	57
3.	Case 3: The K2 Mission	59
E.	SMALLEST DETECTABLE PLANET	60
F.	SUMMARY	63
V.	SOLAR TORQUE ON SPACECRAFT	65
A.	TORQUE	65
B.	SPACE ENVIRONMENTAL DISTURBANCE TORQUE	65
C.	RADIATION DISTURBANCE TORQUE	67
1.	Force Due to Electromagnetic Radiation.....	67
2.	Irradiance of Sun	69
3.	Force from Direct Solar Photon Radiation	70
4.	Defining the Sun-Vector	73
a.	<i>Definition Based on Direction Cosine Matrix</i>	73
b.	<i>Definition Based on Trigonometry</i>	79
c.	<i>Comparison between Sun-Vector Based on DCM and Trigonometry</i>	81
5.	Moment Arm	81
6.	Solar Torque.....	81
D.	SUMMARY	82
VI.	KEPLER SOLAR RADIATION PRESSURE MODEL	83
A.	SIZING OF KEPLER	83
B.	FLAT PLATE MODEL	88
C.	RESULTS FROM FLAT PLATE SRP MODEL	91
D.	MATCHING THE DATA	94
E.	SUMMARY	100
VII.	POINTING CAPABILITY USING TWO WHEELS	101
A.	SOLAR TORQUE RELATIVE IN THE REACTION WHEEL PLANE	101
B.	VALIDATING RESULTS	110
C.	FURTHER ANALYSIS	111
D.	POSSIBLE SCIENCE	117
E.	SUMMARY	120
VIII.	CONCLUSION	121
	LIST OF REFERENCES	123
	INITIAL DISTRIBUTION LIST	129

LIST OF FIGURES

Figure 1.	Kepler field of view, from [3].....	2
Figure 2.	Depiction of original Kepler L2 orbit, from [2].....	3
Figure 3.	Kepler's heliocentric orbit, after [6]	3
Figure 4.	Kepler flight system, showing integrated photometer and spacecraft, after [3].....	4
Figure 5.	Kepler photometer architecture, from [3]	6
Figure 6.	Exoplanet discoveries 1995–2014, from [12].....	8
Figure 7.	Comparison of size of exoplanet discoveries, from [12]	9
Figure 8.	Schematic view of two possible point-drift mode observations on a CCD, from [14]	10
Figure 9.	Conceptual illustration of K2, from [16]	11
Figure 10.	Comparison of different filters, from [27]	18
Figure 11.	Hertzsprung-Russell diagram of temperature vs. luminosity of stars, from [25]	21
Figure 12.	Methods for detecting exoplanets, from [18].....	24
Figure 13.	Gravitational microlensing example, from [31].....	26
Figure 14.	Light curve from star with orbiting planet HD 209458, from [18].....	29
Figure 15.	Schematic of a transit, after [18].....	30
Figure 16.	Light diffracting by small aperture, from [39].....	35
Figure 17.	Airy disk diffraction from circular aperture, from [39]	35
Figure 18.	Sample best focus axial point spread function (PSF) of the <i>Kepler</i> optics, from [40]	36
Figure 19.	Image centered on pixel	41
Figure 20.	Rotation of pixel around z -axis and y -axis.....	42
Figure 21.	Overlay of original circle with distorted ellipse	43
Figure 22.	Kepler photometer, after [3]	44
Figure 23.	Estimating A_{lost} due to cross-boresight axis rotations	45
Figure 24.	Simple representation of a telescope, (not to scale).....	46
Figure 25.	Solving for Δy , (not to scale).....	48
Figure 26.	Image centered on a pixel away from the center of the focal plane array	49
Figure 27.	Image shifted after rotation of $\Delta\phi$	50
Figure 28.	Visualization of A_{lost}	51
Figure 29.	Planet detection ability for different drift rates per LC.....	61
Figure 30.	Predicted photometric precision vs. actual data, after [46].....	62
Figure 31.	Example of force inducing a counter-clockwise torque	65
Figure 32.	Effects of major environmental disturbance torques on spacecraft, from [49]	66
Figure 33.	Schematic of Compton scattering.	68
Figure 34.	Depiction of the three main types of incident solar radiation effects: (a) absorbed radiation; (b) specularly reflected radiation; (c) diffusely reflected radiation, after [51]	71

Figure 35.	Angle between Sun vector, \hat{S} , and the normal, \hat{n} , to the surface.....	72
Figure 36.	Depiction of Frame O in different orientations in Kepler's heliocentric orbit	73
Figure 37.	Definition of Frame B , centered on the spacecraft body, from [3]	74
Figure 38.	First rotation - rotation by ϕ around the x -axis	75
Figure 39.	Second rotation - rotation by ψ around the z' -axis	75
Figure 40.	Third rotation— rotation by θ around the y'' -axis	76
Figure 41.	Validation rotations.....	78
Figure 42.	Trigonometric derivation of the Sun vector.....	79
Figure 43.	Different test orientations	80
Figure 44.	Cut-away of Kepler spacecraft, from [3]	83
Figure 45.	Image of Kepler figure in Microsoft Visio with dimensioning line, after [3].....	84
Figure 46.	Dimensioned Kepler schematic, after [3]	85
Figure 47.	Kepler flight system, showing integrated photometer and spacecraft, from [3].....	86
Figure 48.	Second dimensioned Kepler schematic, after [3]	87
Figure 49.	Schematic of flat plate, after [48]	89
Figure 50.	Hexagonal pattern of solar panels.....	90
Figure 51.	Solar torque ($\mu\text{N}\cdot\text{m}$) around the x -axis (a) flat plate model with $c_p=[2.10,0.752,0.0]$ m, (b) Ball model, after [13]	91
Figure 52.	Solar torque ($\mu\text{N}\cdot\text{m}$) around the y -axis (a) flat plate model with $c_p=[2.10,0.752,0.0]$ m, (b) Ball model, after [13]	92
Figure 53.	Solar torque ($\mu\text{N}\cdot\text{m}$) around the z -axis (a) flat plate model with $c_p=[2.10,0.752,0.0]$ m, (b) Ball model, after [13]	92
Figure 54.	Solar torque ($\mu\text{N}\cdot\text{m}$) around the x -axis (a) flat plate model with $c_p=[3.11,0.368,-0.0379]$ m, (b) Ball model, after [13].....	96
Figure 55.	Solar torque ($\mu\text{N}\cdot\text{m}$) around the y -axis (a) flat plate model with $c_p=[3.11,0.368,-0.0379]$ m, (b) Ball model, after [13].....	96
Figure 56.	Solar torque ($\mu\text{N}\cdot\text{m}$) around the z -axis (a) flat plate model with $c_p=[3.11,0.368,-0.0379]$ m, (b) Ball model, after [13].....	97
Figure 57.	Absolute error ($\mu\text{N}\cdot\text{m}$) of solar torque around the x -axis (a) flat plate model with $c_p=[2.33,0.752,0.0]$ m (b) flat plate model with $c_p=[3.11,0.368,-0.0379]$ m	98
Figure 58.	Absolute error ($\mu\text{N}\cdot\text{m}$) of solar torque around the y -axis (a) flat plate model with $c_p=[2.33,0.752,0.0]$ m (b) flat plate model with $c_p=[3.11,0.368,-0.0379]$ m	98
Figure 59.	Absolute error ($\mu\text{N}\cdot\text{m}$) of solar torque around the z -axis (a) flat plate model with $c_p=[2.33,0.752,0.0]$ m (b) flat plate model with $c_p=[3.11,0.368,-0.0379]$ m	99
Figure 60.	Schematic of reaction Kepler reaction wheels, after [13].....	101
Figure 61.	Schematic of reaction wheel plane	102
Figure 62.	Cosine of the angle between RW plane normal and the solar torque vector ..	103
Figure 63.	Projections of solar torque onto unit vector normal to reaction wheel plane	104
Figure 64.	In-plane solar torque ($\mu\text{N}\cdot\text{m}$)	105

Figure 65.	Out of plane solar torque ($\mu\text{N}\cdot\text{m}$)	106
Figure 66.	Time it takes to rotate around the x -axis by 0.009 arcsec for flat plate model.....	108
Figure 67.	Time it takes to rotate around the y -axis by 0.009 arcsec for flat plate model.....	109
Figure 68.	Time it takes to rotate around the x -axis by 0.009 arcsec for Ball model.....	110
Figure 69.	Time it takes to rotate around the y -axis by 0.009 arcsec for Ball model.....	111
Figure 70.	Pointing error around x -axis for SC (arcsec)	112
Figure 71.	Pointing error around y -axis for SC (arcsec)	112
Figure 72.	Pointing error around x -axis for LC (arcsec)	113
Figure 73.	Pointing error around y -axis for LC (arcsec)	113
Figure 74.	Pointing error around x -axis for SC using momentum bias, (arcsec)	116
Figure 75.	Pointing error around x -axis for LC using momentum bias, (arcsec).....	116
Figure 76.	Possible planet detection ability with drift rates per LC for Case 1, Case 3, uncontrolled and momentum bias with flat plate model.....	118
Figure 77.	Predicted photometric precision with momentum bias curve vs. actual data, after [46]	119

THIS PAGE INTENTIONALLY LEFT BLANK

LIST OF TABLES

Table 1.	Temperature ranges of Harvard sequence, after [29].....	20
Table 2.	Case 2: signal and noise values for 12th magnitude star	58
Table 3.	Case 3: signal and noise values for 12th magnitude star	59
Table 4.	Analysis of the different orientations in Figure 3.4	79
Table 5.	Analysis of the different orientations in Figure 3.4	81
Table 6.	Estimated Kepler dimensions	88
Table 7.	Parameters for the flat plate SRP model	91
Table 8.	Test cases to validate results in Figure 53	94
Table 9.	Summary of comparison of flat plate models	99
Table 10.	Kepler RW vectors, after [13].....	103
Table 11.	Uncontrolled pointing errors for short and long cadences.....	114
Table 12.	Constants needed for momentum bias angular rate estimate.....	115
Table 13.	Significant results for pointing error using momentum bias	117

THIS PAGE INTENTIONALLY LEFT BLANK

LIST OF ACRONYMS AND ABBREVIATIONS

ADCS	attitude determination and control system
AU	astronomical unit
CCD	charge-coupled device
FGS	fine guidance sensors
IAU	International Astronomical Union
LC	Long Cadence
LOS	line-of-sight
NASA	National Aeronautics and Space Administration
PPM	parts per million
RW	reaction wheels
SC	Short Cadence
SRP	solar radiation pressure

THIS PAGE INTENTIONALLY LEFT BLANK

ACKNOWLEDGMENTS

I would first like to thank the Creator who provided us with this vast and wondrous universe that allows for such amazing human ventures as the Kepler mission; no matter how much we think we know, each step teaches us how much more there is to learn.

I would like to thank Professor Luscombe for helping me with the physics portion of this thesis. Particularly, I am grateful to Professor Luscombe for finding time to discuss the mundane topics like this thesis, in between the lively mind-bending adventures into the world of string theory, super-symmetry, dark matter, quantum mechanics and other creative theories that attempt to understand the universe's mysteries and the puzzle God provided.

I would also like to thank Professors Karpenko and Ross for guiding me through the engineering portions of this thesis and for reminding me to use tried and tested equations to understand the answer, instead of using the answer to try and redefine physics. I especially would like to thank Professor Karpenko for reading my thesis numerous times and providing lots of constructive feedback to help produce the best thesis possible; thank you for finding the time in your busy schedule to assist me with my thesis and my intellectual growth.

I express my gratitude to the NPS thesis processing staff, who works tireless hours to ensure my thesis is ready for release, and my fellow students in the 591 curriculum, for challenging me to always do better and for providing plenty of opportunities to chat when I wanted to take a break from writing this tome.

Last, but not least, I am indebted to my wife, Suri, for taking care of the family and the house during our time at NPS, especially the last quarter when I spent extra hours at work writing this thesis. I want to say thank you for doing a great job with home schooling; maybe I won't object if you want to do it again. Also, I thank my children, Avi, Eli, Shimmy, and Yudi, for being kids, fixing my martial arts, especially my horse stance, and always making me read even after I fall asleep. תושלב"ע

THIS PAGE INTENTIONALLY LEFT BLANK

I. INTRODUCTION

NASA began the Discovery Program in 1992 to “unlock the mysteries of the solar system” [1]. In 1995, two scientists, “Mayor and Queloz reported detection of the first extrasolar planet orbiting a solar-like star” [2]. NASA outlined the goal to find more habitable extrasolar planets in its 1998 Strategic Plan [2]. As a result of these science visions, NASA created the Kepler spacecraft, which NASA stated was “designed to detect transits of Earth-size planets in the ‘habitable zone’ orbiting 9 $<mv<15$, F through M type dwarf stars... in the constellations Cygnus and Lyra” [3]. As outlined by NASA’s Discovery program, Kepler had the scientific objective to “yield a broad understanding of planetary formation, the frequency of formation, the structure of individual planetary systems and the generic characteristics of stars with terrestrial planets” [4].

A. KEPLER MISSION AND SPACECRAFT

The Kepler spacecraft launched on March 7, 2009, had a mission to find extrasolar Earth-like planets, mainly using the transit detection method [3]. The predicted number of planets that are in the habitable zone and can be detected is about 1% of all estimated planets in the habitable zone [5]. Therefore, a location needed to be chosen with a large group of main sequence, Sun-like stars, to provide a statistically useful amount of possible detections. Another constraint on the search area was due to the fact that Earth-like planets are expected to have no more than one transit a year, and on average that transit will only last about 6.5hr [3]. Because of this limited window of opportunity, it was also necessary to pick a grouping of stars and an orbit that would not be obstructed by the Earth, Sun or the Moon. The star field chosen that best met the above criteria was a group of approximately 160,000 stars between the constellations of Cygnus and Lyra, centered on a right ascension of 19h 22m 40s and a declination of +44d 30m 00s as shown in Figure 1..

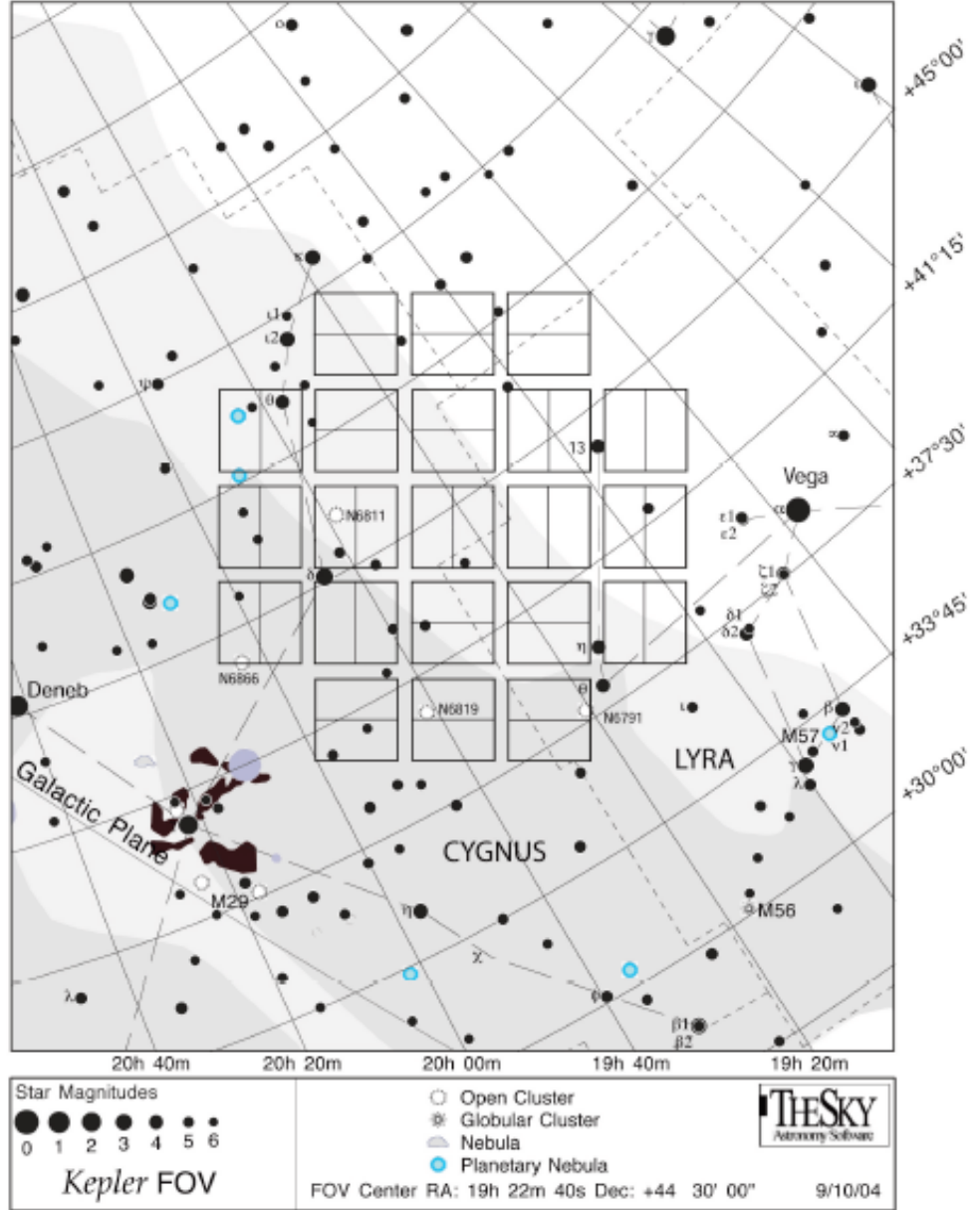


Figure 1. Kepler field of view, from [3]

The relation of this star field to the ecliptic plane means these stars will not be blocked by the Sun. In order to ensure that the spacecraft is not blocked by the Earth or the Moon the orbit had to be carefully chosen. Originally, the orbit was planned to be around a special point in the Sun, Earth, Moon system called the Lagrange 2, (L2), point as shown in Figure 2. .

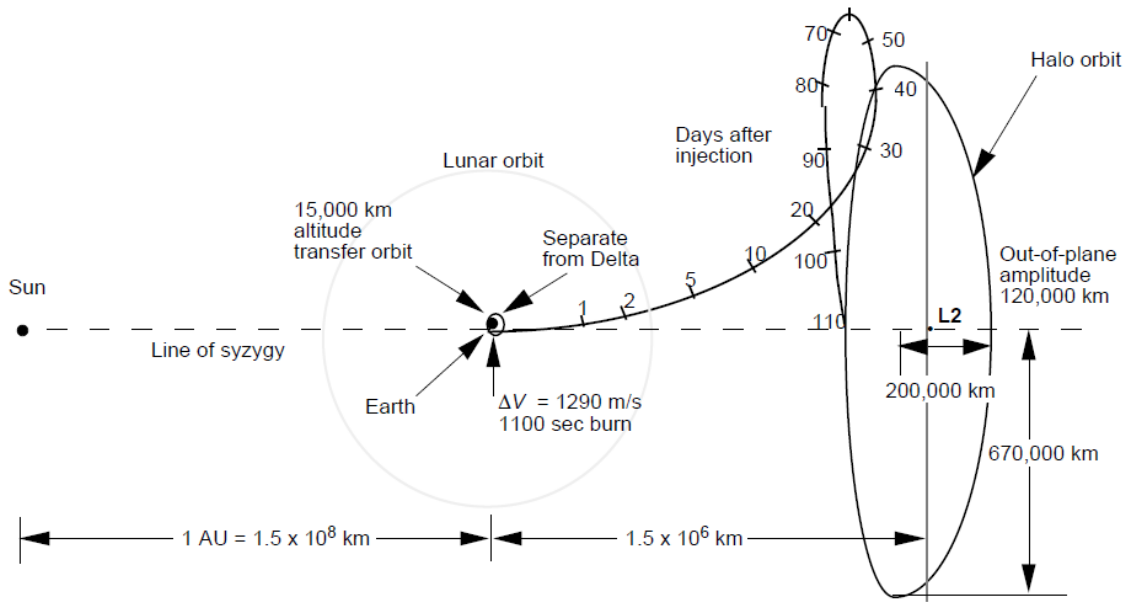


Figure 2. Depiction of original Kepler L2 orbit, from [2]

Insertion into this special orbit would have required the spacecraft to have a propulsion system and a large Delta launch vehicle, so in the interest of cost reduction the propulsion system was removed, the launch vehicle was changed and the orbit was altered to the Earth trailing heliocentric orbit [2], seen in Figure 3..

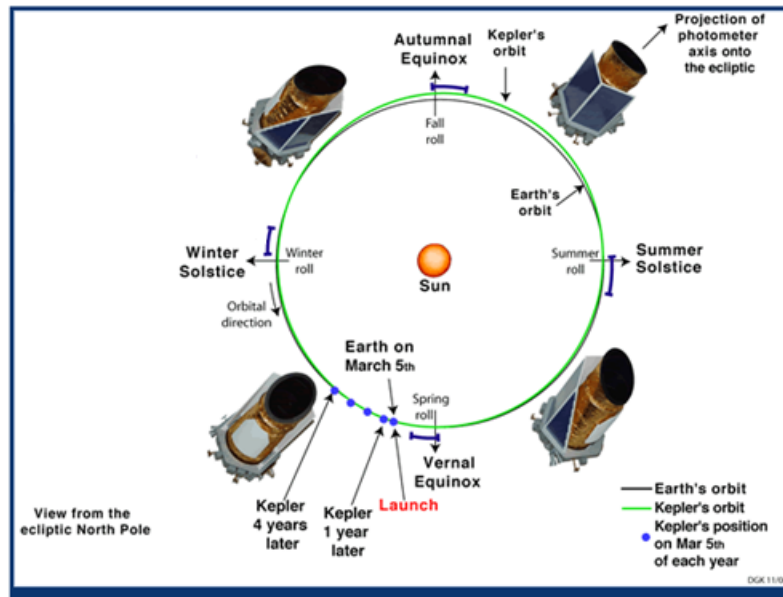


Figure 3. Kepler's heliocentric orbit, after [6]

The heliocentric orbit provides several benefits. It allows near continuous viewing of the Cygnus field. The only planned time where viewing will be limited is during the main data transmittal to the ground which occurs approximately every 31 days and then during the quarterly 90 degree turn of the spacecraft to re-orient the solar panels towards the Sun [3]. Another benefit of the heliocentric orbit is that the number of disturbances experienced by Earth orbiting satellites is reduced. The main disturbance acting on Kepler is due to solar radiation pressure.

In addition to selecting the correct orbit and group of stars the satellite itself has some very important components to allow it to detect planets. The main components are highlighted in Figure 4. and each one will briefly be described to highlight its importance.

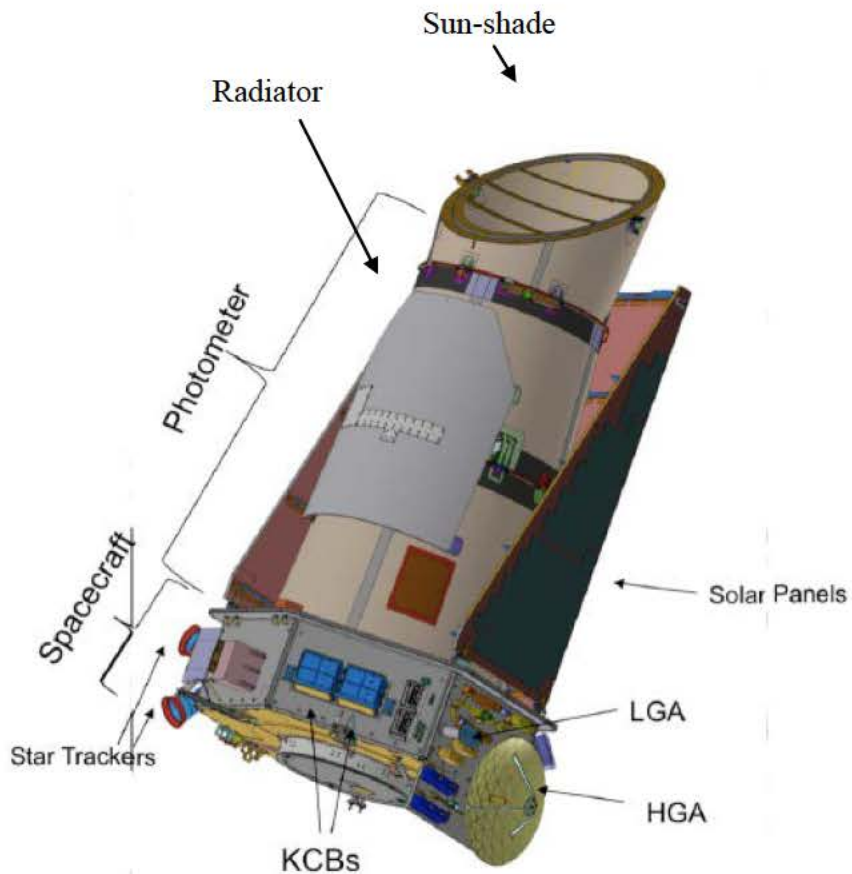


Figure 4. Kepler flight system, showing integrated photometer and spacecraft, after [3]

Kepler consists of two main components, the spacecraft bus and the photometer. The spacecraft bus is the bottom part of Kepler; it is a hexagonal shape and contains most of the components of the spacecraft. The star trackers provide coarse-guidance information and the Kepler control boxes (KCBs), command the photometer, and receive and co-add data from the pixels [3]. The LGA, low gain antenna, allows the spacecraft to receive telemetry and downlink data at a low rate, but from most orientations. The HGA, the high gain antenna, on the other hand, is for the main data transmittal and provides a high data rate. This is the main antenna used during the approximate 31-day data transmissions. In order to use the HGA, Kepler must be rotated so the HGA is pointed towards Earth. The solar panels consist of three main pieces, two triangular-like and one rectangular that provide the power requirements of the Kepler spacecraft. Since the panels do not go around the whole spacecraft, it is necessary to roll the spacecraft about every 90 days to keep the solar panels facing the Sun. The sun-shade protects the photometer and the instrumentation from being saturated by light from the Sun. The radiator on the back of the spacecraft helps ensure the desired operating temperatures can be maintained. In addition to the equipment shown in Figure 4., there are four reaction wheels, which provide “ <0.009 arcsec 3σ single axis pointing stability” [3].

A cutaway of the photometer, arguably the most important part of the spacecraft, is shown in Figure 5. .

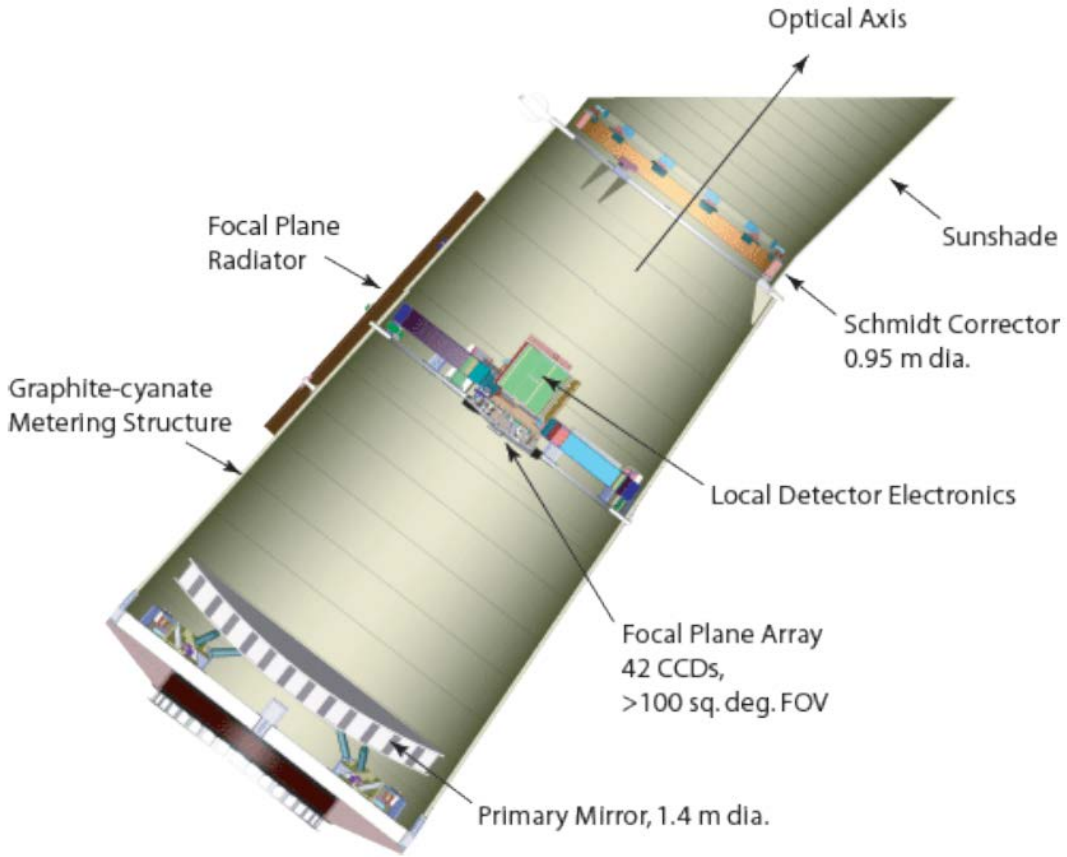


Figure 5. Kepler photometer architecture, from [3]

There are several key components to highlight in reference to the photometer. It is a wide-field Schmidt telescope; this means that the light from the star field enters Kepler through the top of the photometer, refracts through the Schmidt corrector, which is a flat lens that removes certain aberrations, and then is reflected by the primary mirror onto the focal plane array. It has an entrance aperture diameter of 950mm, a $f/ \# = 1.473$, an effective focal length of 1399.20mm, a 16.1° field of view and a 1.4m primary mirror. The focal plane array consists of 21 science and 4 fine guidance sensor, FGS, CCD modules. In total, the science CCD modules have a combined 94.6 million $27 \times 27\mu\text{m}$ pixels, each with a well depth $>1.0 \times 10^6$ electrons. The FGS use $13 \times 13\mu\text{m}$ pixels to provide more precise pointing accuracy than can be obtained using the star trackers [3].

Kepler must stare at the same star group for at least 3.5 years to capture at least three transits of an Earth-like planet to provide the statistical confidence necessary for

planet detection [3]. Kepler accomplishes this by using two specific collection modes, short cadence, SC, and long cadence, LC. One set of data is collected during a 6.54-second frame, which consists of the integration time (the time between pixel reads), the pixel read time and the exposure time (the time the pixel collects photons before being read) [3]. The SC is a mode that coadds, or combines, the data from a number of frames. Typically, 9 frames are used in an SC totaling around 59s. A typical LC is a co-adding of 30 SCs, for about 30 minutes of data. The SC is used for asteroseismology and transit timing of exoplanets, whereas the LC is used for the normal transit method. The majority of science data is obtained using LC [7].

Kepler has been extremely successful at planet detection; the most recent numbers are 989 confirmed planets, and 4234 planet candidates [8]. Kepler is a photometer, so it identifies planets by measuring photons, but does not provide a visual image; therefore, one way a planet is confirmed is through observation by other instruments like ground telescopes [9]. Besides the average planet that orbits around a star similar to the planets in the Earth's solar system, Kepler has also made unique discoveries like multiple planets orbiting double star systems and planets around a four-star system [10]. Possibly the most exciting day in Kepler science was February 26, 2014, referred to as the Kepler Planet Bonanza, when on one day NASA confirmed the discovery of 715 planets orbiting 305 stars [11].

Figure 6. shows that until the Kepler Planet Bonanza only about 1000 exoplanets had been discovered, which includes discoveries by Kepler and other telescopes; after the announcement there were about 1700 planets discovered. The Kepler Planet Bonanza was clearly an historic day and proved the success of the Kepler mission.

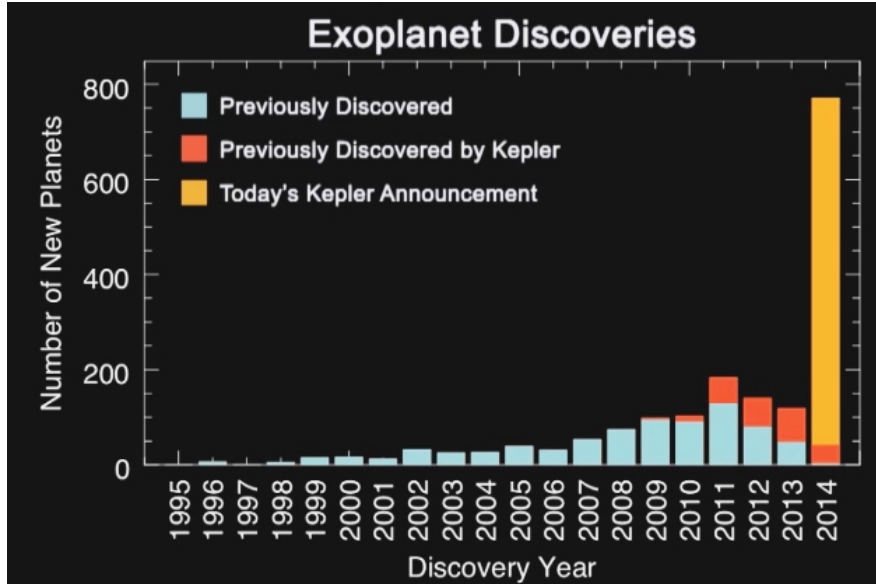


Figure 6. Exoplanet discoveries 1995–2014, from [12]

Figure 7. is a second view of the data announced on February 26, 2014; it details the number of new planets and the size of the planets announced compared to all discoveries before the Kepler Planet Bonanza. One of the key points from Figure 7. is that Kepler was designed to find Earth-like planets, and before Kepler most planet discoveries had been large Jupiter-size planets.

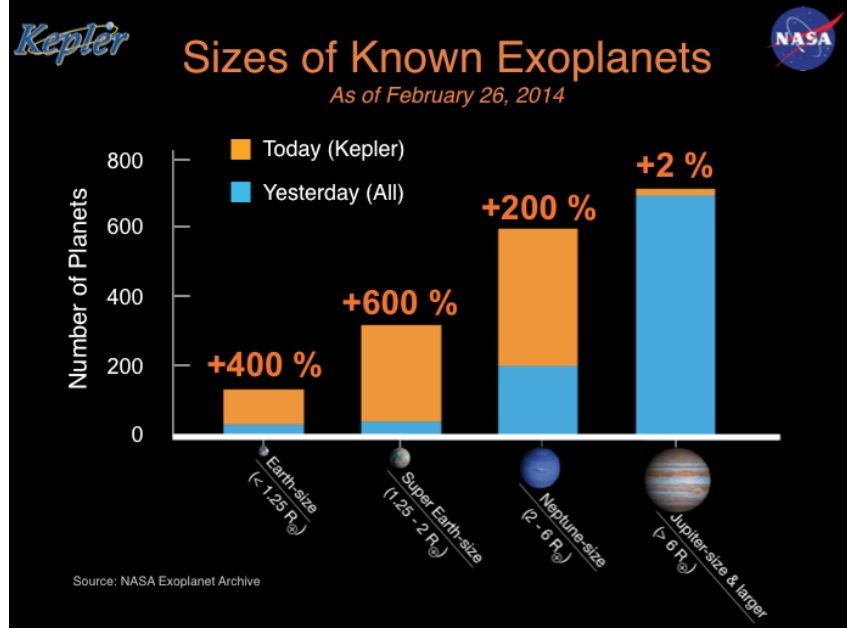


Figure 7. Comparison of size of exoplanet discoveries, from [12]

Unfortunately, after almost four years Kepler could no longer collect data that produced results like the Kepler Planet Bonanza. Kepler lost one of its four reaction wheels in July 2012 and a second in May of 2013 preventing 3-axis attitude control resulting in the end of the original Kepler mission [13]. Initial analysis determined that instead of the <9 milliarcsec pointing stability, over the 30 minute LC, the degraded pointing stability would amount to between 0.5–1.0 arcsec of jitter and a drift of about 1.4 degrees over 4 days, as shown in Figure 8. . Instead of the target star remaining centered on the same location on the CCD, for most of the observation period it would move across the CCD. This creates a risk for target stars to fall off the CCD and, if this happens, they can no longer be observed. In addition, extra noise due to unaccounted for multiple pixel interactions, is expected.

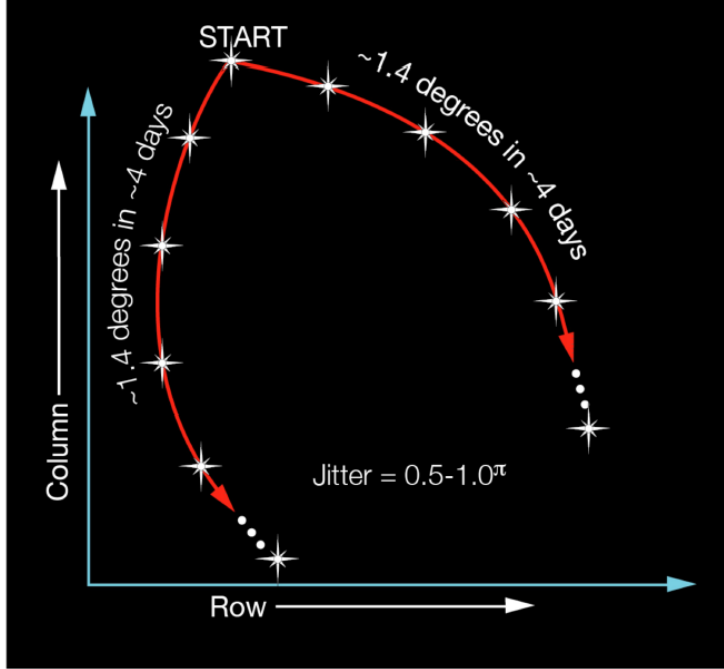


Figure 8. Schematic view of two possible point-drift mode observations on a CCD, from [14]

Although the remaining reaction wheels were not able to provide Kepler with the required pointing stability to detect planets in Cygnus and Lyra, the science equipment on Kepler was still functional. Therefore, in August 2013, when NASA decided to officially suspend the original Kepler mission [14], NASA also requested ideas from the science community at large on possible new uses for Kepler, ultimately resulting in what is now referred to as the K2 mission.

B. THE K2 MISSION

The K2 mission is a new mission utilizing the failed Kepler spacecraft. The main driver behind this new mission is the reduction in pointing stability of Kepler due to solar torque. If uncontrolled, solar torque induces a rotation around all three axes of the spacecraft. Moreover, all three axes cannot be controlled with only two reaction wheels and conventional linear control techniques [15]. To address this issue, engineers at Ball Aerospace developed hybrid control architecture for Kepler: a combination of the two remaining wheels controlling the spacecraft along two of the three axes, momentum biasing of the wheels for stiffening the third axis and thruster control to control error

accumulation around the third axis [13]. Specifically for Kepler, this is best implemented by minimizing the solar torque effects around the uncontrolled axis. The minimum solar torque occurs when the spacecraft bore-sight is pointed in the ecliptic plane [13], meaning that Cygnus and Lyra can no longer be viewed. The combination of the hybrid control scheme and the requirement to minimize the solar torque resulted in the K2 mission oriented in plane with the ecliptic in such a way that the solar torque along the photometer axis is near zero as shown in Figure 9. . This new pointing mechanism results in an estimated 10 arcsec drift in an 8-hour period. This gives a new pointing stability of about 0.63arcsec of drift in a 30 minute, LC period [13]. This stability is much less than that of the original mission.

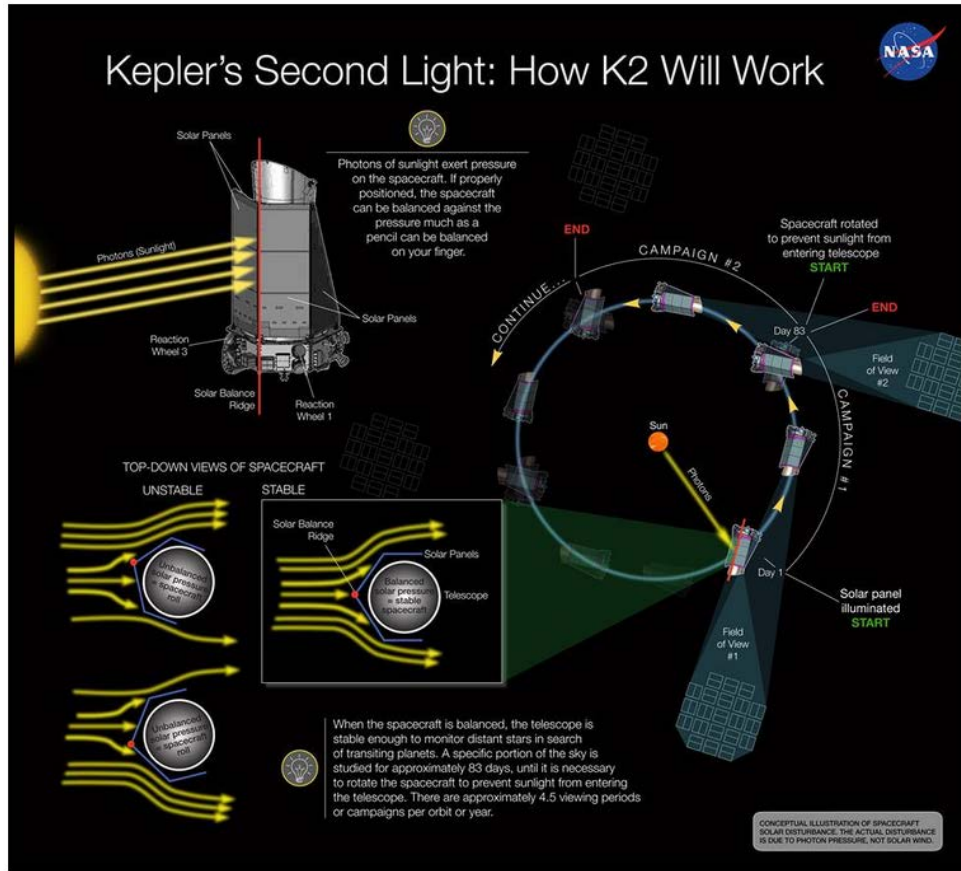


Figure 9. Conceptual illustration of K2, from [16]

Currently, there are 12 campaign periods planned through 2016, each lasting about 90 days [16]. The campaigns correspond to different areas in the celestial sky that can be seen from the ecliptic. Although the pointing stability of the K2 mission is reduced and does not allow for the same type of planet detection of the original Kepler mission, new science targets are possible, including [17]:

- Possible transiting planet hosts
- Pulsational variable stars
- Rotationally variable stars
- Flaring stars
- Accreting stars and interacting binaries
- Galaxies and supernovae
- Microlenses

C. THESIS OBJECTIVE AND SCOPE

This thesis focuses on two objectives. The first objective is to describe how Kepler detects planets. This elucidates an understanding of the original pointing requirements and helps explain why the original mission could not be continued. The analysis on pointing stability attempts to bridge the gap between science requirements and engineering requirements.

The second objective was to develop a solar torque model of Kepler in order to assess the capabilities of the spacecraft in other “off ecliptic” attitudes. The goal is to explore the types of science possible in attitudes not considered as part of the K2 mission.

This thesis consists of eight chapters, including this one. Chapter II provides a definition for planets, explains how stars are classified and gives a brief overview of different methods used to detect planets. Chapter III specifically explores the transit detection method, the method mainly used by Kepler. Chapter IV explains the scientific requirements that must be met to detect planets using the transit method. A simple solar torque model is developed to facilitate the analysis. Chapter V provides the background necessary to understand the effects of solar torque on a spacecraft. Chapter VI details the development of the Kepler solar torque model and compares the model to other available

results. Finally, Chapter VII explores the achievable pointing stability considering the inability to control the spacecraft around all three axes with only two wheels. This thesis is brought to a close with some concluding remarks and suggestions for future work in Chapter VIII.

THIS PAGE INTENTIONALLY LEFT BLANK

II. PLANET HUNTING

For over 2000 years, mankind has explored the skies, and wondered whether the Earth was the only planet; philosophers contemplated ideas such as: “*There are infinite worlds both like and unlike this world of ours*” (Epicurus, 341–270 BCE) and “*There cannot be more worlds than one*” (Aristotle, 384–322 BCE) [18]. Although six of the eight planets in our solar system are visible to the naked eye and were known by Greek astronomers, including Aristotle, they were not necessarily identified as similar objects to Earth. After the invention of the telescope around the seventeenth century, the other two solar system planets, Uranus and Neptune, were discovered in the eighteenth and nineteenth centuries [19]. Then, in 1994, the first extrasolar planet was discovered by an astronomer at Pennsylvania State University, Dr. Aleksander Wolszczan. This was followed by the discovery of the first extrasolar planet orbiting a sun-like star in 1995. Two more planets were discovered only months later. Most recently, the French launched CoRoT, has contributed several dozen confirmed exoplanets outside of our solar system [20], and Kepler has led to the discovery of 978 confirmed planets outside the solar system [21].

This chapter covers three main topics necessary to understand planet hunting. This first section provides the accepted description for a planet, and how that relates to the planet that Kepler is searching for. The second section discusses the current star classification system and its relevance to Kepler. The final section provides a brief overview of different planet detection techniques, including an overview of the transit method.

A. DEFINING A PLANET

1. International Astronomical Union

The International Astronomical Union (IAU) was founded in 1919 “to promote and safeguard the science of astronomy in all its aspects through international cooperation” [22]. The union consists of professional astronomers from over 95 countries and national science societies representing 73 nations. Some issues that the IAU deals

with include defining “fundamental astronomical and physical constants [and] unambiguous astronomical nomenclature” [22].

2. IAU Planet Definition

In 2006, the IAU convened in Prague and, as part of its agenda, describes planets in the solar system using three categories, of which two are cited below:

(1) A Planet is a celestial body that (a) is in orbit around the Sun, (b) has sufficient mass for its self-gravity to overcome rigid body forces so that it assumes a hydrostatic equilibrium (nearly round) shape, and (c) has cleared the neighbourhood around its orbit. (2) A “dwarf planet” is a celestial body that (a) is in orbit around the Sun, (b) has sufficient mass for its self-gravity to overcome rigid body forces so that it assumes a hydrostatic equilibrium (nearly round) shape (c) has not cleared the neighbourhood around its orbit, and (d) is not a satellite. [23]

Although these definition were specifically written with regards to the Earth’s solar system, it would be a fair assumption that this definition would also be fitting for extra-solar/exo planets, planets in orbit around other stars, which is what the Kepler mission is interested in.

3. Planet Definition Relevant to Kepler Mission

The IAU resolution, which defined the characteristics of planets in 2006, has not been without its opponents and critics [24]. In fact, when the Kepler mission was formulated the definition of the IAU did not even exist. Kepler’s main focus is habitable or Earth-size planets, which are defined by Koch et al. as “a solid body with a mass between $\sim .5$ and ~ 10 Earth masses at a distance from its parent star such that the planet’s surface temperature and atmospheric pressure are consistent with the presence of liquid water” [2]. This ignores most of the key points in the definition of a planet as determined by the IAU. In contrast to the IAU definition, the Kepler mission was designed to find planets, which are described as any extra-solar object with the potential of supporting life like Earth. This does not mean that other objects were ignored, but the specific search for Earth like planets was used as part of the design requirements for the mission.

B. STAR CLASSIFICATION

Astronomers as far back as Hipparchus have tried to create a system to classify stars; in the case of Hipparchus stars were organized by how bright they appeared to him [25]. This simple classification scheme continues to be modified until today. Two components of the current methods of star classification that are relevant to the Kepler mission are the apparent magnitude and the spectral class.

1. Apparent Magnitude

Astronomers developed a system to categorize stars by quantifying the relative magnitude, m , of a star; how the flux of one star relates to another or to some reference flux:

$$m_2 - m_1 = -2.5 \log_{10} \left(\frac{F_2}{F_1} \right) \quad (1)$$

The radiant flux, F , is a value that can be measured, and is the amount of energy emitted per second per unit of surface area. In one formulation the datum for the radiated flux was determined to set the star Vega with an apparent magnitude of zero, and the Sun was measured to have a flux at the Earth about 51 billion times greater than from Vega [26]. Therefore, the visual apparent magnitude of the Sun is:

$$m_{Sun} - m_{Vega} = -2.5 \log_{10} \left(\frac{F_{Sun}}{F_{Vega}} \right)$$
$$m_{Sun} - 0 = -2.5 \log_{10} (51 \times 10^9) \approx -26.77 \quad (2)$$

There are two major drawbacks when using the relative magnitude to classify a star: (1) A star that is farther from the Earth, although brighter at its surface, could be classified as dimmer because of its distance. (2) The value of apparent magnitude is dependent on the measurement of flux, which depends on the type of filter used on the measuring instrument. To address the first concern astronomers defined the absolute magnitude, discussed in the next section.

The issue about filters is that the flux and its measurement are wavelength dependent. The most common filters are U (ultraviolet), B (blue) and photo visual (V), which pass different wavelengths as shown in Figure 10. .

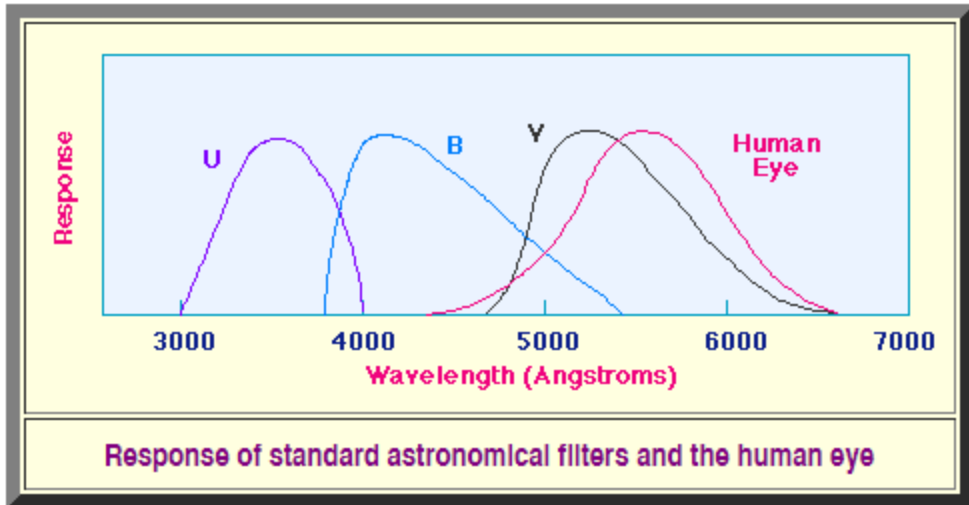


Figure 10. Comparison of different filters, from [27]

Because of the compositions of stars, it is fully expected that a star will have a higher apparent magnitude in one wavelength than another. One way to mitigate this ambiguity is to specify the type of filter was used. A second way, used by the Kepler team, is to develop equations that can encapsulate different values based on different filters in one apparent magnitude calculation.

2. Absolute Magnitude

As mentioned in the previous section the apparent magnitude is a measure of a star's brightness measured from Earth, but this can be misleading because a star that is brighter but farther away may appear to be dimmer at the Earth then a dimmer but closer star. Therefore, the absolute magnitude system was devised to create a more objective standard for ranking stars. This system quantifies stars based on how they appear at a distance of 10 parsecs [25]. A parsec (abbreviated as pc) is “the distance to an object at which the orbit of the Earth subtends an angle of one arcsecond” [25]. Given that the orbit of the Earth is one astronomical unit, (AU), which is equal to $1.496 \times 10^{11} \text{ m}$, a parsec is defined as:

$$1\text{pc} = \frac{1\text{AU}}{1\text{arc-sec}} = \frac{1.496 \times 10^{11} \text{ m}}{4.848 \times 10^{-6} \text{ rad}} = 3.086 \times 10^{16} \text{ m} \quad (3)$$

Unlike, the apparent magnitude, which uses flux measurements, the absolute magnitude, M , is:

$$M \equiv -2.5 \log_{10} \left(\frac{L}{L_{ref}} \right) \quad (4)$$

where luminosity, L , is the total energy emitted at the surface of a star and L_{ref} is the reference luminosity [25].

Flux and luminosity are directly related. Flux is the luminosity measured at a given distance from the source spread through the surface of a sphere, therefore L_{ref} is related to a well-defined reference bolometric, all wavelength, flux measured at a distance of 10 pc [25] by :

$$L_{ref} = 4\pi F_{ref} d^2 \quad (5)$$

with

$$F_{ref} = 2.53 \times 10^{-8} W / m^2; d = 10 pc \quad (6)$$

giving:

$$L_{ref} = 3.0 \times 10^{28} W / m^2 \quad (7)$$

As an example, it has been determined that the Sun has $L = 384.6 \times 10^{24} W$ [28]. Therefore, its absolute magnitude is:

$$M = -2.5 \log_{10} \left(\frac{384.6 \times 10^{24}}{3.0 \times 10^{28}} \right) = 4.7 \quad (8)$$

3. Spectral Classification

Besides the magnitude of a star, an alternative way to compare stars is to use spectral classification. The beginnings of stellar classification by spectral type began in the 19th century with work done by Joseph von Fraunhofer with a comparison of the Sun to other stars [29]. This was followed with a more thorough approach by Father A. Secchi, who categorized around 4,000 stars into four categories defined by similar properties [29].

Towards the end of the 19th century Harvard conducted a survey of even more stars and named this work and its results the Henry Draper Catalogue [29]. After several

iterations of examining these original results the now famous spectral categories of O, B, A, F, G, K and M were developed. The letter categories group the stars based on a temperature range and chemical make-up [29]. One such listing of ranges is summarized in Table 1. .

Table 1. Temperature ranges of Harvard sequence, after [29]

Star Class	Temperature (°K)
O	>25,000
B	11,000–25,000
A	7,600–11,000
F	6,000–7,600
G	5,100–6,000
K	3,600–5,100
M	<3,600

In addition to the letter category, a number is added to represent where in the range of temperatures the star is. These numbers are between zero and nine [29], where zero refers to the highest temperature in the category and nine refers to the lowest.

A second level of classification that adds to the Harvard classification system was developed around 1930 by an astronomer named W. W. Morgan [29]. The work done by Morgan classifies stars not only by their temperature and make-up as dictated by the letter and number but also by their luminosity or the absolute magnitude as described in the previous section. By categorizing stars in this manner, Morgan discovered that there were five additional groupings that could be made based on clusters of data. These groups are:

- I: Supergiants
- II: Bright Giants

- III: Normal Giants
- IV: Subgiants
- V: Main Sequence Stars/Dwarfs [29]

The different classification schemes are easily visualized through the use of a Hertzsprung-Russel (H-R) diagram, which shows many stars on a plot based on temperature versus magnitude, temperature versus luminosity and Harvard classification letters. An example of an H-R diagram is shown in Figure 11. .

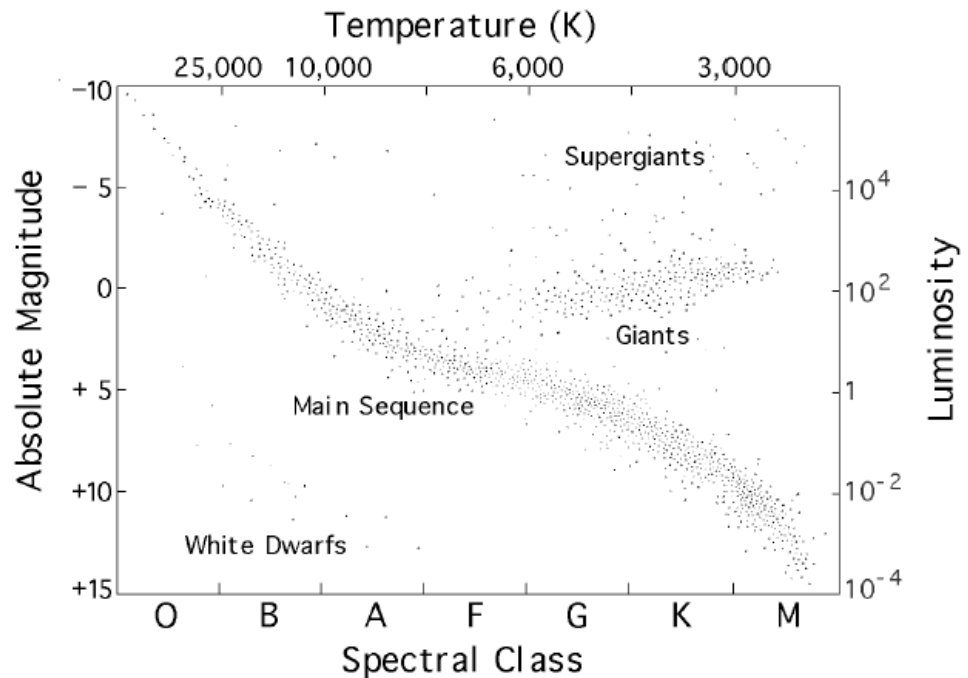


Figure 11. Hertzsprung-Russell diagram of temperature vs. luminosity of stars, from [25]

An example of a classification of a star using the categories described above is of the Sun. The Sun is classified as a G2V star; this means the Sun has a temperature around 5800°K , which has been confirmed by measurement [28], hence G2 and it is a main sequence star, which explains the V.

This classification scheme is significant because if one knows the star spectral classification one can calculate the approximate radius of a star using the physics of

blackbody radiation. Blackbody radiation relates the luminosity, L , and temperature, T , via the Stefan-Boltzmann constant, σ as in:

$$L = \sigma AT^4 \quad (9)$$

Assuming the stars are spherical, the area, A in (9), is simply the surface area of sphere ($A = 4\pi R^2$). Therefore, given the luminosity and temperature, the radius of the star can be computed as:

$$R = \sqrt{\frac{L}{4\pi\sigma T^4}} \quad (10)$$

Continuing with the example for the Sun:

$$R = \sqrt{\frac{384.6 \times 10^{24} W}{4\pi \left(5.67 \times 10^{-8} \frac{W}{m^2 \circ K^4} \right) (5778^\circ K)^4}} = 6.96 \times 10^8 m \quad (11)$$

As seen in Figure 11., the absolute magnitude is similar for main sequence stars with similar temperatures, therefore, when a star other than the Sun is referred to as G2V it can be assumed to have a similar radius to the Sun, regardless of the apparent magnitude. This is an important point to remember because several times throughout this thesis a 12th magnitude G2V star is mentioned, which does not have the same apparent magnitude as the Sun, but it is assumed to have the same radius as the Sun.

4. Apparent Magnitude and its Relevance to Kepler

In Kepler's field of view there are about 160,000 stars, however there is not enough telemetry bandwidth to transmit information for all the monitored stars [30]. This created a need to provide a mechanism to quickly and accurately identify and classify the potential target stars that provide the greatest odds for finding planets [30]. The absolute magnitude is not sufficient for this classification because it is based on the energy at the star's surface, while Kepler is collecting light energy from star near the Earth. Therefore, use of the absolute magnitude would require additional data processing. Similarly, the apparent magnitude as explained is also not completely sufficient for this task. The reference flux or brightness needed to calculate the apparent magnitude is usually referenced to Earth and is filter dependent. Therefore, a modified version of the apparent magnitude was used to create a new Kepler magnitude; this is the apparent magnitude as

seen by the Kepler photometer and accounts for different values through different filters [30]. In order, to define the apparent Kepler magnitude data was collected and processed and a catalog of stars was developed to specifically use with the Kepler mission.

For the purposes of this thesis the actual equations used to calculate the Kepler magnitude are not important. However, what is important is how many electrons are estimated to be read by the photometer for a given Kepler magnitude. This estimate is made by first modifying (2) to utilize values of photoelectron current instead of the flux. The photoelectron current is the number of electrons on a charge-coupled device (CCD) that are excited by the photons from the star, as in:

$$m_2 - m_1 = -2.5 \log_{10} \left(\frac{f_2}{f_1} \right) \quad (12)$$

where f_i is the photoelectron current.

In the design process, a 12th Kepler magnitude star was used as the reference star, which gives the reference photoelectron current, $f_{ref} = 2.1 \times 10^5 \frac{e^-}{s}$ [3]. Using this reference photoelectron current for f_1 in (12), taking $m_1 = 12$ and given the Kepler magnitude of any star, m_2 , its photoelectron current can be calculated by:

$$f_2 = 10^{-0.4(m_2 - 12)} f_{ref} \quad (13)$$

Throughout the rest of this thesis the classification of a star will be identified by its Kepler apparent magnitude and its spectral class.

C. PLANET DETECTION METHODS

A third important part of background information to understand how Kepler performs its mission is to understand planet detection techniques.

There are three main challenges for exoplanet discovery [31]:

- Planets don't produce any light of their own, except when young.
- They are an enormous distance from us.
- They are lost in the blinding glare of their parent stars.

While being cognizant of these constraints, scientists have developed several creative ways to detect exoplanets. These methods exploit advances in both physics and technology. Figure 12. summarizes the available techniques.

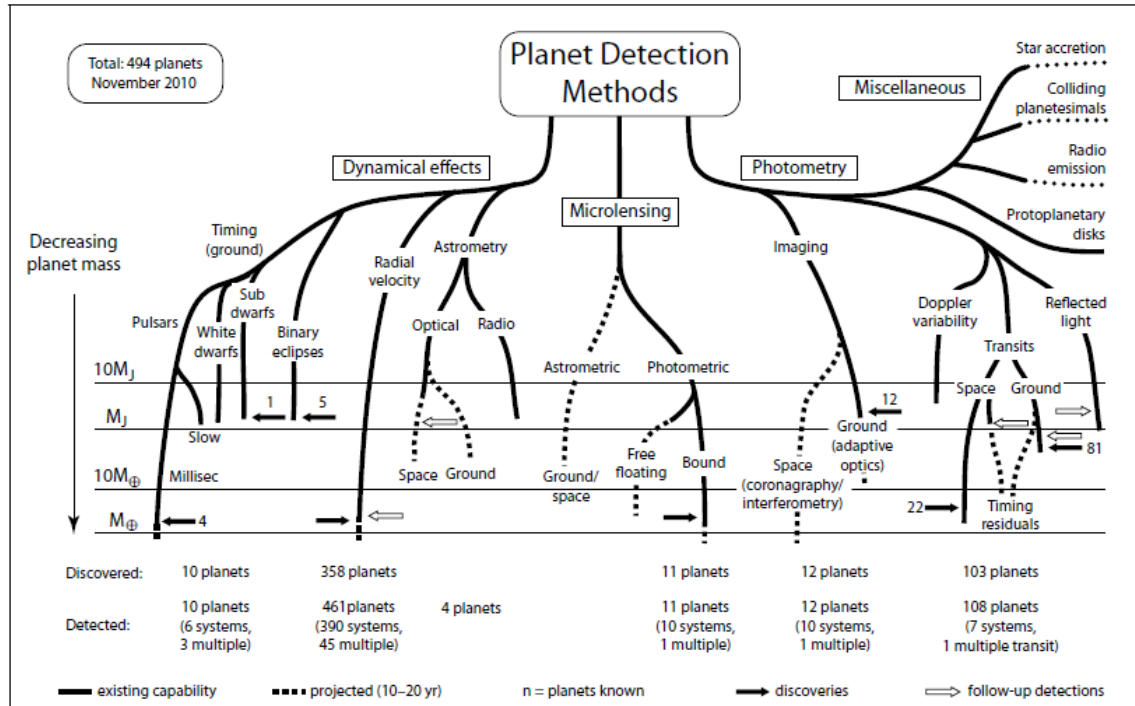


Figure 12. Methods for detecting exoplanets, from [18]

There are three particular points to note about Figure 12. . The symbol M_J , refers to the mass of Jupiter, and M_{\oplus} , refers to the mass of Earth. The numbers of discovered planets were updated as of 2010, so they do not reflect the discoveries of planets since then, specifically the numerous planets discovered by Kepler. According to NASA there are 5022 exoplanet discoveries, 1746 confirmed with over half coming from Kepler data [32].

As shown in Figure 12. there are at least 10 methods that have been successfully used to discover exoplanets. These methods include radial velocity, astrometry, direct imaging, gravitational microlensing and transit.

1. Radial Velocity

Radial velocity, sometimes referred to as the Doppler Shift method, exploits the notion that a star and its orbiting planet actually revolve around a center of mass; the planet thus has a gravitational tug on the star so there is a measurable change in the star's position and velocity with time. The instruments measure the Doppler Shift resulting from the perturbation of the star. The larger and closer the planet is to the star the more noticeable this effect is, which is why some of the first planets discovered are Jupiter-class [31]. However, as shown in Figure 12., exoplanets with a mass close to the Earth's can be detected using this method [18].

2. Astrometry

Astrometric techniques exploit the same physics as the radial velocity technique, however instead of measuring the Doppler Shift astronomers measure the actual change in motion of the star [31]. The major limitation of this method is that largest expected displacements for the most massive nearby stars are not large enough for current state of the art technology [18]. Only one confirmed exoplanet has been discovered by the Astrometric method [32].

3. Direct Imaging

Direct imaging, as its name implies, discovers planets by taking actual pictures. This is extremely difficult because of the problems listed above: planets normally do not produce light, they are very far away and glare from parent stars blocks them [31]. Two methods of direct imaging are coronography and interferometry: coronography uses a masking device to block out the light from a nearby star, while interferometry “uses specialized optics to combine light from multiple telescopes in such a way that the light waves from the star cancel each other out” [31].

4. Gravitational Microlensing

As NASA explains gravitational microlensing exploits a result from “Einstein’s theory of general relativity: gravity bends space” [31].

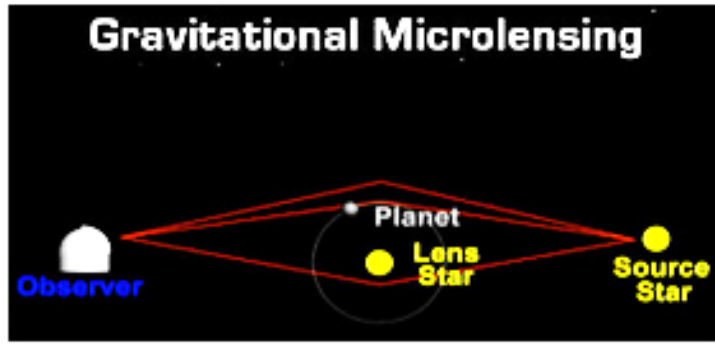


Figure 13. Gravitational microlensing example, from [31]

As shown in Figure 13., light starts from the source star and then instead of traversing an expected straight line is bent around the “lens” star, which corresponds to the lower red line. If a planet is orbiting the “lens” star it will contribute an extra bending of space-time, which “causes a temporary sharp increase in brightness and change of the apparent position of the star” [31]. The planet can be detected and its mass can be estimated by the amount of extra bending of the light.

5. Transit Method

Every star has a particular measurable brightness, however if a planet, or another object passes in front of the star its brightness is reduced. This reduction in brightness is what systems that employ the transit method attempt to measure [31]. In addition, to implying the existence of a planet, the reduction of brightness provides an estimate of the size of the planet and after several measurements it is possible to calculate the orbital period.

D. SUMMARY

This chapter defined a planet, explained star classification methods and provided a brief overview of a few different planet detection techniques. NASA and other space agencies have developed satellites and ground based systems to detect exoplanets using some of the techniques described above. In 1990, NASA launched the Hubble Space Telescope, and although not the primary mission has utilized the direct imaging method

to discover planets like Fomalhaut b [33]. The Spitzer Space Telescope, launched in 2003 by NASA, uses IR sensors for direct image detection of exoplanets [33]. The Large Binocular Telescope Interferometer and Keck Interferometer also use the direct imaging technique [33]. CoRoT, launched in 2006 by CNES and ESA, and Kepler use the transit method to detect planets [33]. The next chapter will provide a more detailed explanation of the transit method, which is used by Kepler.

THIS PAGE INTENTIONALLY LEFT BLANK

III. THE TRANSIT METHOD FOR PLANET DETECTION

The Kepler spacecraft's main method for detecting planets is the transit method, therefore a more thorough understanding of this concept is important. The data provided by Kepler can also be exploited using other methods, like transit timing variation as explained in [34], and a special algorithm that utilizes a phenomenon called beaming effect or Doppler boosting as explained in [35].

According to Michael Perryman, 1999 marked the year of the first successful detection of an exoplanet using the transit method [18]. The basic premise as explained above is to measure the flux from the star and detect a drop in flux as a planet or other object transits in front of the star [18]. The decrease in flux is observed through the analysis of light curves, which plot the flux versus time. The light curve from the first planet detected utilizing the transit method is shown in Figure 14. .

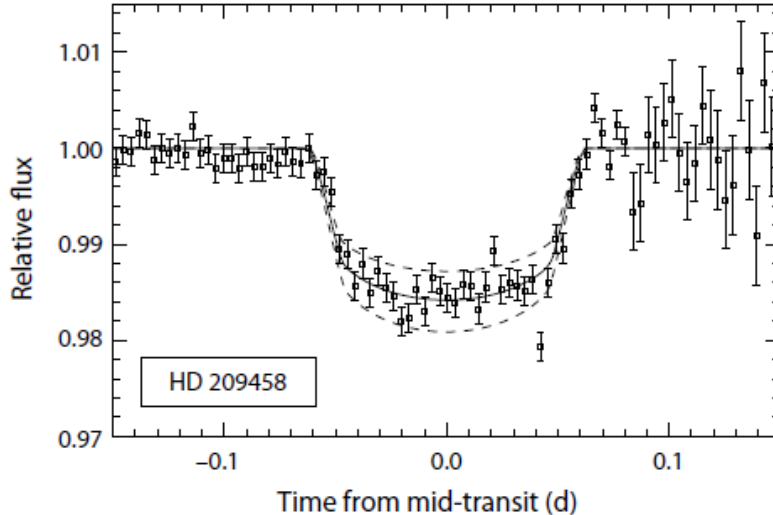


Figure 14. Light curve from star with orbiting planet HD 209458, from [18]

The transit method can be employed by both space and ground assets. Some examples of ground systems are Wide-Angle Search for Planets, MEarth project and Siding Spring Observatory Wide Field Imager [18]. Some space based assets include

Kepler, Hubble Space Telescope and CoRoT, (Convection, Rotation & Planetary Transits) [33]. Space based systems have an advantage over ground-based systems in that there are no atmospheric aberrations to deal with on orbit. As of 2011, the smallest drop in flux that a ground system could detect was about 0.1 [18] whereas Kepler, for example, was designed to detect planets that cause a reduction as little as 20 parts per million, ppm, i.e. 20×10^{-6} .

The basic governing equation for flux reduction is defined as approximately the ratio between the radius of the transiting planet and the radius of star it orbits [18]:

$$\Delta F \approx \left(\frac{R_p}{R_*} \right)^2 \quad (14)$$

where ΔF , is the transit depth also referred to as the loss in flux (a dimensionless quantity), R_p , is the radius of the transiting planet and R_* is the radius of the orbited star. Equation (14) assumes that both the star and the planet can be modeled with a circular cross-section. Usually, the radius of the planet is unknown so the transit depth is measured and then the radius of the planet is approximated using (14).

For a real planet orbiting a star, there are actually several changes that can occur with the measured flux from the star as shown in Figure 15..

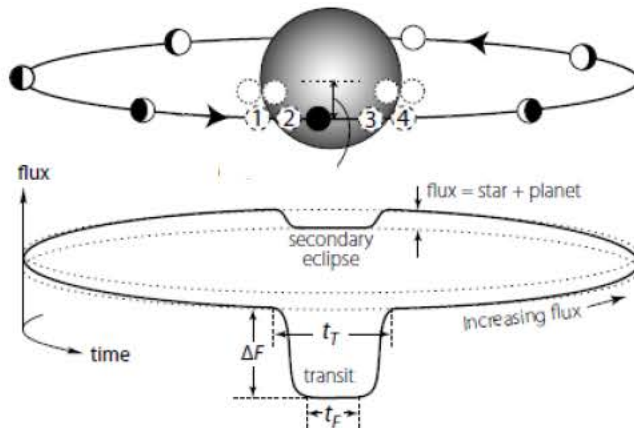


Figure 15. Schematic of a transit, after [18]

In Figure 15., the bottom circular dashed line is the baseline flux expected from the star, whereas the uppermost dashed circular line represents the flux of the star and planet combined, this includes the light produced from the star reflected off the planet's surface. The main transit, the one that provides the greatest transit depth occurs when the planet crosses directly in front of the star, calculated using (14). The secondary dip shown in Figure 15. is actually because the starlight that is being reflected off the planet is being blocked by the star. The largest decrease is the former and that is the transit of interest. Also shown in Figure 15. are times, t_T the total transit time, and t_f , the transit time measured by when the planet is completely eclipsing part of the star.

Another property of the planet that can be calculated is an estimate of the orbital radius. If there are multiple passes observed the interval between the transits can be equated to the period of the orbit. Then using Kepler's third law, which relates the period of an orbit to the orbital radius, the orbital radius is:

$$r = \left(\frac{P^2 GM_*}{4\pi^2} \right)^{1/3} \quad (15)$$

Where P is the period between transit depth measurements, G is Newton's universal gravitational constant, M_* , is the mass of the star and r is the orbital radius. Using (15) assumes a knowledge of the mass of the star. One approach for a quick approximation of the mass of a star is to relate it to the luminosity of the star, which is assumed known. The mass of a planet and luminosity are related by [36]:

$$L \propto M_*^3 \quad (16)$$

This relationship relies on several simplifications so for real stars the exponent is not 3, as an example stars that range between about half and two times the mass of the sun the exponent is 2.6 [36].

This chapter provided a more detailed explanation of the transit method used by Kepler and other instruments, but still only discussed the simplest aspects of the transit method. As mentioned in the introduction it has proven to be highly successful especially with regards to detecting relatively small planets that are about the size of the Earth. The past two chapters covered nomenclature and explained planet detection in a general

sense. The next chapter therefore will deal with planet detection and how it specifically relates to Kepler.

IV. KEPLER SCIENCE REQUIREMENTS

As the previous chapter explained, the transit method is useful in detecting planets by measuring a change in the flux from the parent star. The advantage of space based systems like Kepler is the capability to detect planets even with very low decreases in flux. This is possible with precise instrumentation in the form of a CCD. This chapter will discuss photometric precision requirements, which are the specifics of the measurements being made that limit the measurement process. This chapter concludes with a discussion utilizing the theory developed in the first sections of this chapter to explain the engineering requirements of the original Kepler mission, expected science capability of Kepler after the failure of two reaction wheels and the current science capability after the engineering solutions described in the introduction.

A. PHOTOMETRIC PRECISION REQUIREMENTS

The photometric precision defines the minimum detectable transit depth and was the guiding principle in the design of the spacecraft. The first step was identifying the science goal, which as Borucki et. al. explained was to “detect a 13,000 km diameter (i.e., an Earth-sized) planet around an $m_v = 12$, G2 spectral class, main sequence star” [5]. The Sun, in the Earth’s solar system is a G2V main sequence star [28] so the transit depth caused by the Earth relative to the Sun is:

$$\Delta F \approx \left(\frac{R_{\oplus}}{R_s} \right)^2 = \left(\frac{6400 \text{ km}}{696000 \text{ km}} \right)^2 \approx 8.4 \times 10^{-5} \quad (17)$$

Based on the fact that all stars classified as G2V are similar, the transit depth of the Earth to the Sun will be similar to any Earth like planet around any Sun like star.

Another key design factor in determining the photometric precision was the signal-to-noise ratio (SNR). Based on work done by Borucki et. al., “a total SNR of approximately eight (or more) from a series of transits is needed to unambiguously recognize a planetary transit when many stars are monitored” [5]. Furthermore, the SNR for a single transit is:

$$SNR_{\text{single transit}} = \frac{SNR_{\text{total}}}{\sqrt{\#\text{of transits}}} \quad (18)$$

A four year mission searching for an Earth-like planet, not just of similar size, but also of a similar orbit to Earth, would yield four transits providing a single transit SNR of:

$$SNR_{\text{single transit}} = \frac{8}{\sqrt{4}} = 4 \quad (19)$$

If the signal that must be detected is the transit depth of the Earth then the total allowed design noise floor is:

$$\text{allowed noise floor} = \frac{\Delta F}{SNR_{\text{single transit}}} = \frac{8.4 \times 10^{-5}}{4} \approx 2 \times 10^{-5} \quad (20)$$

Therefore, the photometric system for Kepler was designed such that for an Earth-like planet orbiting a G2V star with $m=12$, the total allowed noise is 20ppm. If the noise is below 20ppm then the transit depth, the signal, is not only detectable but also statistically recognizable as a planet.

B. CCD SIGNAL

The desired detection signal is the transit depth; however there is a second signal of interest, which is the signal strength of the star's original flux. The signal strength detected by a given pixel identified by n and m is representing its row and column is:

$$s(n, m; \lambda) = \int_{-\infty}^{+\infty} \int_{-\infty}^{+\infty} f(x, y; \lambda) r(x - np, y - mq; \lambda) dx dy \quad (21)$$

where $f(x, y; \lambda)$ for a very distant source is the Point Spread Function (PSF), $r(x, y)$ is the Pixel Response Function (PRF) and p and q are the pixel pitch [37].

1. PSF

The PSF, or impulse response function of the optics system, describes the diffraction of light as it passes through an aperture and interacts with the optical equipment like lenses. In other words, the PSF describes how the intensity of the source is distributed over a given area.

The phenomena of light diffraction was first discovered in the 17th century; if light passes through an aperture, that has a dimension on the order of the wavelength of light then the light will be spread out, diffract, as seen in Figure 16. . This is referred to as the Huygens-Fresnel principle [38].

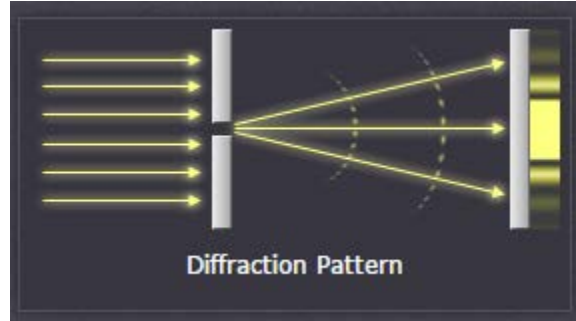


Figure 16. Light diffracting by small aperture, from [39]

Different shaped apertures can cause different refraction patterns. One such pattern explained by Fraunhofer [38], is that for a circular aperture; light will be diffracted as the Airy disk shown in Figure 17. .

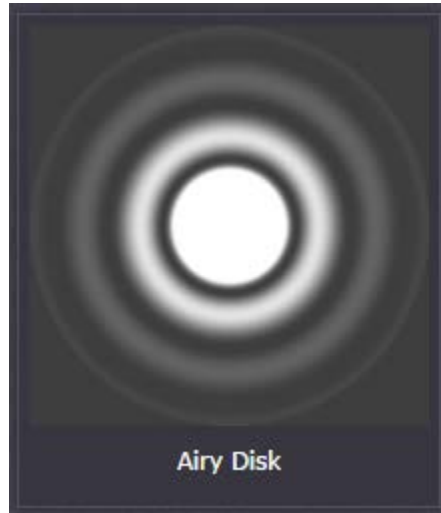


Figure 17. Airy disk diffraction from circular aperture, from [39]

In addition to diffraction caused by apertures, light can be diffracted by changing the focus of mirrors and lenses. Kepler was designed with the ability to change the focus

of light incident on the CCD's in order to ensure the PSF covered several pixels to prevent pixel saturation [3]. Each pixel has a well depth, which is the maximum amount of excitable electrons available. If more photons interact with any individual pixel than available electrons information would be lost. The PSF for Kepler was chosen to be a “best focus,” as shown in Figure 18., and was tested via simulation software [40] and later calibrated in flight [3].

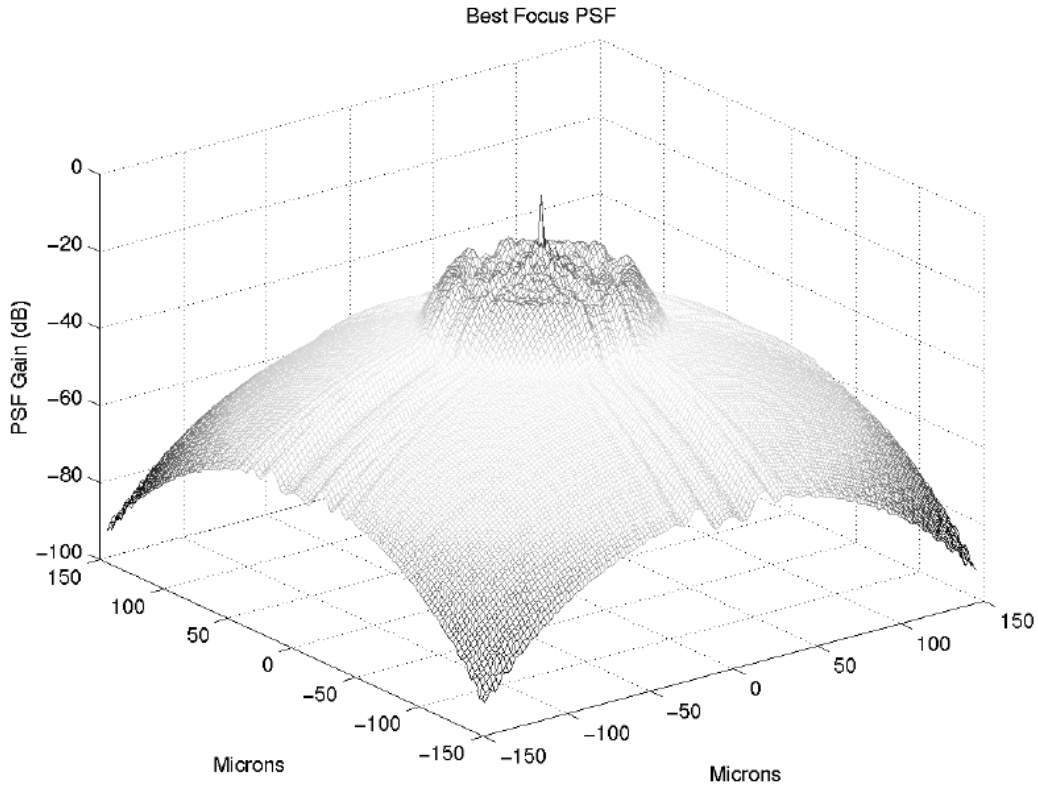


Figure 18. Sample best focus axial point spread function (PSF) of the *Kepler* optics, from [40]

The Kepler instrument was calibrated based on the requirement that 95% of the energy from the target star would be captured by an array of no more than 7x7 pixels, with 50% of the energy focused on the center pixel. Each pixel is a $27 \mu\text{m} \times 27 \mu\text{m}$ square, so 7 pixels is 189 microns [3].

2. PRF

The PSF describes what happens to the incident energy through the optical system while the PRF describes what happens to the light when it interacts with the CCD. Some information that can be described by the PRF is intra-pixel variations, differences in response based on the location of incidence on individual pixels, and inter-pixel variations, interactions that occur between disparate pixels [37]. If a pixel is uniform, then regardless of where on the pixel the point source impacts the spread of the energy will be the same.

In Kepler's case the PRF includes the optical PSF, described above, the jitter Power Spectral Density (PSD), module defocus, the CCD response function, the electronic impulse response and any aberrations due to stellar spectra type [3]. Kepler's pixels are non-uniform and the image will overlap several pixels, therefore five PRF's were determined for each pixel array [41]. The five PRF's consisted of one at each corner and one in the center of each pixel. This allowed for an interpolated PRF for any position on the pixel [41]. The PRF's were developed through design, simulation, testing and finally in flight calibration where stars were selected, measured and PRF's were updated to provide the best fit [3].

3. Total Signal

One method for using a CCD photometer is as follows: the source impacts the pixels, the energy is spread out, the electrons are read, and then through processing the signal is fit to the PRF and PSF to determine to the original source. PRF/PSF fitting is completed by using expected PRF/PSF of a target star and then comparing those results to the actual measurements [41]. This is useful in removing unwanted, but measured stars. As part of the processing it is necessary to know the total signal from a source; this signal is usually spread out over several pixels so it is the sum of the signals from the desired pixels [37]:

$$S = \sum_{n,m} s(n,m; \lambda) \quad (22)$$

Since solving (22) in terms of the PRF and PSF is quite complicated instead of using (21) to calculate the total signal this thesis assumes that the photoelectron current, calculated from (13), over a specific time period is the total signal:

$$S = f_2 t \quad (23)$$

C. NOISE

Both space-based and ground based telescopes can be used to detect planets using the transit method. Ground-based telescopes do not have the limitations of cost and difficulty of launching large telescopes into space. Therefore, there is an advantage with regard to the possible aperture size. However, ground based telescopes have a great limitation due to the Earth's atmosphere, the noise levels produced from atmospheric effects like atmospheric scintillation prevent current ground based telescopes from detecting planets smaller than ones that produce a transit depth no lower than about 1% [18]. This threshold limits ground based systems to detection of Jupiter size planets and larger. Thus, space-based telescopes are the preferred system of employment for transit detection of Earth like planets.

For a space-based telescope the total measurement noise can be defined as a combination of signal noise and instrument noise [5]:

$$\sigma_{noise} = \sqrt{\sigma_{signal,noise}^2 + \sigma_{instrument,noise}^2} \quad (24)$$

1. Signal Noise

The signal noise includes shot noise and noise due to stellar variability [5].

a. Shot Noise

The shot noise is an inherent statistical noise that must be accounted for when using a CCD. The statistics of shot noise follow Poisson statistics [5]. Poisson statistics are governed by the Poisson distribution, which is the “number of counts... in a fixed interval of time” for a random process with a steady rate of change [42]. Given the number of electrons calculated from (23), and based on Poisson statistics the shot noise error is:

$$\sigma_{\text{shot,noise}} = \frac{\text{error}}{\text{signal}} = \frac{\sqrt{S}}{S} = \frac{1}{\sqrt{S}} \quad (25)$$

Therefore, as the magnitude of the signal decreases the shot noise increases.

b. Stellar Variability

Stellar variability defines the change in flux of a star due to different physical phenomena like sun spots. Ideally, the stellar variability of every target star would be known, however the only star at the time when the Kepler mission was designed that had data on its variability was the Sun in the Earth's solar system. Therefore, the measured noise due to stellar variability of the Sun was used as the design figure of merit, with the assumption that most target stars will have similar stellar variability properties to the Sun [5].

c. Summary

Combining the shot noise and stellar variability noise the total signal noise is:

$$\sigma_{\text{signal,noise}}^2 = \sigma_{\text{shot,noise}}^2 + \sigma_{\text{stellar var,noise}}^2 = \frac{1}{S} + \sigma_{\text{stellar var,noise}}^2 \quad (26)$$

2. Instrument Noise

The instrument noise combines dark current noise, read noise and pointing noise [5].

a. Read Noise and Dark Current Noise

Read noise is the introduction of extra electrons due to reading the pixels, the two parts that contribute to read noise are: the conversion from an analog to digital signal and the characteristics of the electronics themselves [43]. Read noise can vary across the CCD so it is difficult to quantify it without measuring [3].

As temperature increases in the CCD material there is an increasing probability that valence electrons are freed causing electrons in addition to the source to be read from the pixels, this is called dark current [44]. One technique to limit the dark current noise is

to cool the CCD [43], the lower the temperature the lower probability electrons will separate. Another method to limit the effects of dark current is to operate the pixels close to full well capacity; this method will also limit the effects of read noise [2]. Each pixel only has a certain amount of electrons that can be excited by photons at any given moment, the well capacity, so if the pixel is operated near its well capacity there are a limited number of electrons that remain to be freed by high temperatures and from read errors. Each method is used by Kepler [3]. Dark current and read noise can be formulated in a similar manner to shot noise in the sense the noise represents the collection of unwanted electrons over the total signal:

$$\begin{aligned}\sigma_{\text{read noise}} &= \frac{e_{\text{read}}^-}{S} \\ \sigma_{\text{dark noise}} &= \frac{e_{\text{dark current}}^-}{S}\end{aligned}\quad (27)$$

b. Pointing Noise

The third aspect of instrument noise is pointing noise, which is a combination of spacecraft jitter and drift. Both can be described as “the movement of the telescope line of sight, (LOS), over time” [3] and both effects are functions of the spacecraft attitude determination and control system (ADCS). Jitter refers to the relatively high frequency LOS movement whereas drift is low-frequency movement. A simple analogy to explain the difference is if a person has a laser pointer pointing at the center of an apple, jitter would be the tiny movements of the laser due to the unsteadiness of the person’s hand around the center of the apple, whereas drift would be if the laser pointer starts moving away from the center of the apple and keeps moving. Jitter noise can be accounted for in the PRF, which as explained above, is true in the case of Kepler [3].

To obtain an accurate calculation of pointing noise, numerical simulations are required, which take into account how the incident energy is distributed across the pixels, for example the Airy disk described above. However, for this thesis a first-order approximation is sufficient. Therefore, similar to the other noise sources described above the pointing noise due to drift can be formulated as some error over the total. Unlike the other noises, which occur due to unwanted electrons, the noise due to drift results in the

loss of the ability to collect electrons. The pointing noise is the ratio of the lost signal S_{lost} to the original signal S_0 [37]:

$$\sigma_{\text{pointing, noise}} = \frac{S_{lost}}{S_0} \quad (28)$$

As an example, in Figure 19., the pixel (outlined in blue) has a uniform distribution of electrons (shaded in gray). Although it was explained above that the actual distribution of electrons is not uniform, if one examines Figure 18. closely, it is apparent that most of the energy is concentrated in a small region, with a sharp drop-off outside of the pixel size of about 27 μm . This justifies the uniform distribution assumption.

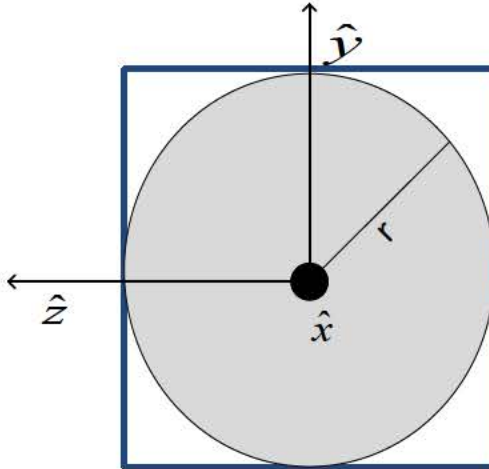


Figure 19. Image centered on pixel

There are three directions that the system can drift caused by rotation of the spacecraft; it can rotate around the y -axis and z -axis, sometimes referred to as the cross-boresight axes, and the x -axis, or about boresight axis. Based on the coordinate system for the pixel in Figure 19., which is the same as for Kepler, the pointing noise can be analyzed in two parts: one due to rotations about the y -axis and z -axis and the second due to rotations about the x -axis.

(1) Cross-boresight axes rotations. Cross-boresight axes rotations affect every pixel regardless of its location on the CCD and will reduce the amount of electrons that can be read from a specific pixel. Figure 20. is a representation of what happens to an

image if it is rotated by an angle ψ around the z -axis and an angle θ around the y -axis by some arbitrary amount.

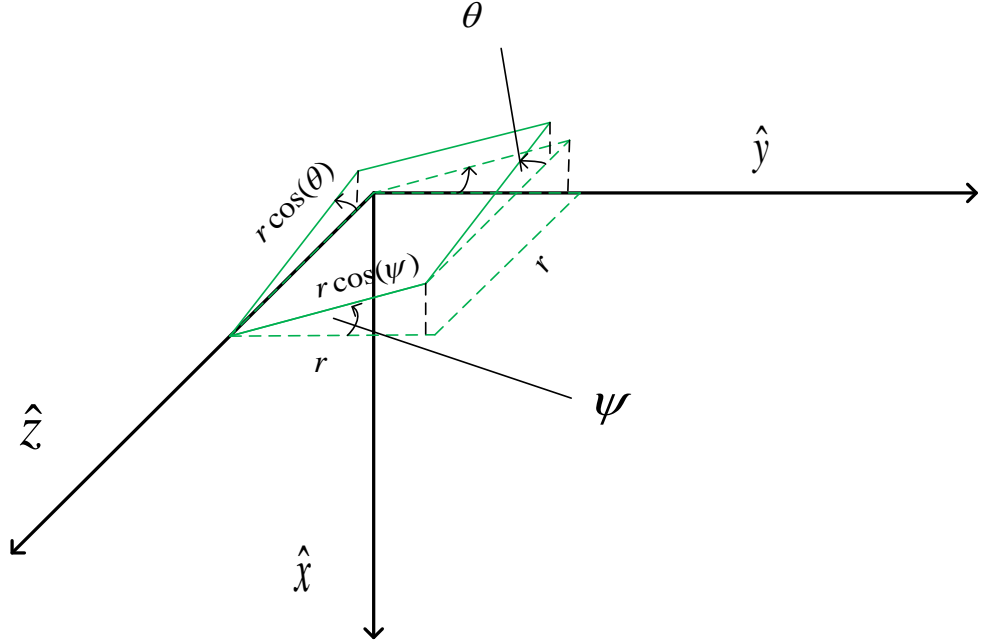


Figure 20. Rotation of pixel around z -axis and y -axis

Defining ρ_{signal} , as the number of electrons per square meter, the total signal can be redefined in terms of the electron density and the area the signal covers on a pixel, A :

$$S = \rho_{signal} A \quad (29)$$

Assuming zero drift around the y -axis and z -axis the signal appears as a circle on a pixel with area:

$$A_0 = \pi r^2 \quad (30)$$

However, under the rotations as shown in Figure 20., the source is distorted in the shape of an ellipse with a new area:

$$A_n = \pi r^2 \cos(\psi) \cos(\theta) \quad (31)$$

Figure 21. is a depiction of the two shapes, the original circle and the ellipse caused by the cross-boresight rotations.

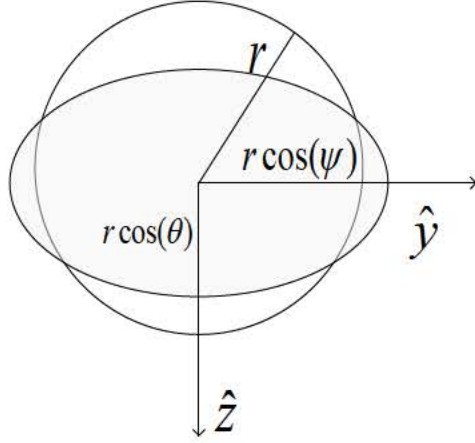


Figure 21. Overlay of original circle with distorted ellipse

One can then define the lost collection area, A_{lost} in terms of (30) and (31):

$$A_{lost} = A_0 - A_n \quad (32)$$

Finally, using (28), (29) and (32), one can estimate the pointing noise for the rotations depicted in Figure 20. [45]:

$$\sigma_{\text{pointing, noise}} = \frac{S_{lost}}{S_0} = \frac{\rho_{signal} A_{lost}}{\rho_{signal} A_0} = \frac{A_0 - A_n}{A_0} \quad (33)$$

Incorporating (30) and (31) the pointing noise is:

$$\sigma_{\text{pointing, noise}} = \frac{\pi r^2 - \pi r^2 \cos(\psi) \cos(\theta)}{\pi r^2} \quad (34)$$

Furthermore, if one assumes that the drift caused by the rotations around the y -axis and the z -axis are small due to small angles of rotation and $\gamma \approx \psi \approx \theta$ one could use a Taylor expansion on (34) and ignore higher order terms, $O(x^2)$ and above to get:

$$\begin{aligned} \sigma_{\text{pointing, noise}} &= 1 - \cos(\psi) \cos(\theta) = 1 - \cos^2(\gamma) \\ \gamma &\ll 1 \\ \therefore \sigma_{\text{pointing, noise}} &\approx 1 - 1 + \gamma^2 + \frac{\gamma^4}{3} + O(\gamma^6) \approx 0 \end{aligned} \quad (35)$$

Two important conclusions come from the analysis of pointing noise due to the rotations around the y -axis and z -axis: (1) the original signal strength does not matter, it is the area that the electrons are distributed over that matters (2) if the rotations are small then there is no significant pointing noise introduced due to these rotations. Two possible

sources of error in this analysis are: large rotations and pixel spreading. If the rotations are large then it is possible that pointing noise around the y -axis and z -axis becomes significant because small angle approximations are invalid. Furthermore, this analysis examined the image spread out over one pixel, while it would not make a difference in the analysis if the electrons were spread out over many pixels, it would make the simplification of assuming the distribution is circular less plausible, once again requiring numerical analysis for a more accurate solution.

The first examination treated the cross-boresight maneuvers as a titling effect, which is a valid approximation if the CCD is near the mirror. However, in the case of Kepler, as shown in Figure 22., the CCD is separated from the primary mirror by the effective focal length, f .

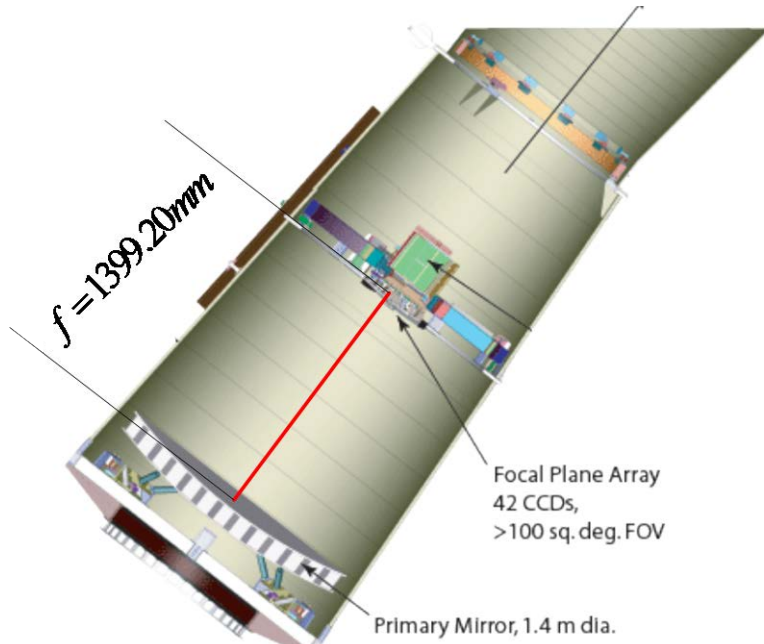


Figure 22. Kepler photometer, after [3]

The distance between the CCD and the primary mirror cause a moment arm effect that leads to a pixel motion that is more drastic than the tilting loss described above. Because of the moment arm it is more correct to assume that if the spacecraft rotates by

$\Delta\psi$ around the z -axis and $\Delta\theta$ around the y -axis then the image will be shifted by some amount Δy and Δz as depicted in Figure 23. .

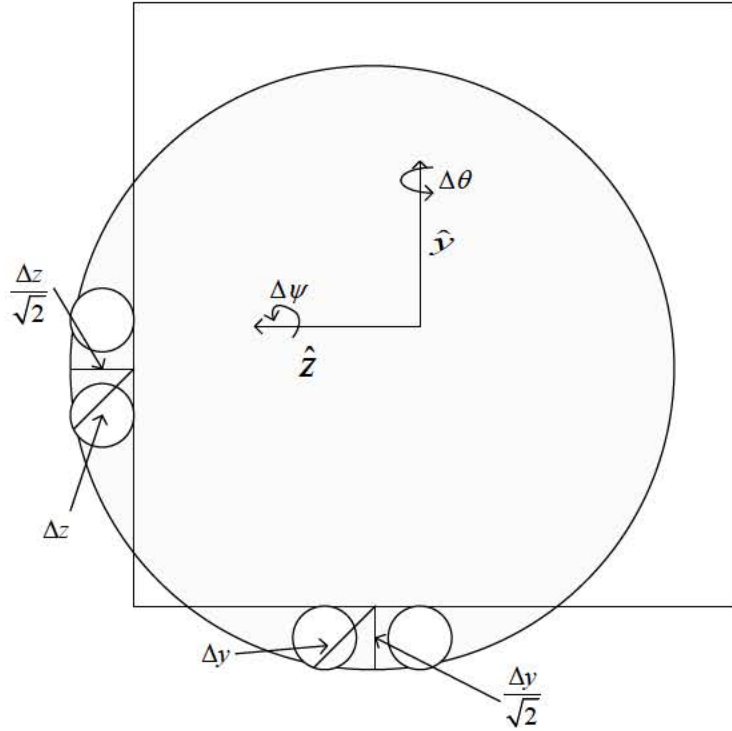


Figure 23. Estimating A_{lost} due to cross-boresight axis rotations

Similar to before, the desire is to determine the ratio of A_{lost} to A_0 . It is simple to solve for A_0 , however accurately calculating A_{lost} is more complicated and requires calculus or numerical simulations, which is not desirable for this first-order approximation. Therefore, a simpler approximation for estimating the loss is to inscribe circles in the sectors of the image that exit the pixel, as shown in Figure 23. . It is assumed that $\Delta\phi \ll 1$ and $\Delta\psi \ll 1$, so the effects of the rotations can be treated as a linear shift of the pixel. It is expected that the first order approximation will be conservative because of the uniform distribution assumption and software tools that reduce the effects of pointing noise are being ignored [46]. Therefore, the smaller area of the two circles compared to the entire shifted segment should reduce the expected over estimation.

Using Figure 23. the lost area is:

$$A_{lost} = 2\pi \left(\frac{\Delta y}{2\sqrt{2}} \right)^2 + 2\pi \left(\frac{\Delta z}{2\sqrt{2}} \right)^2 = \frac{\pi\Delta y^2 + \pi\Delta z^2}{4} \quad (36)$$

In this thesis it is desired to work with rotation angles instead of distances therefore, it is necessary to relate Δy and Δz to their respective rotations $\Delta\theta$ and $\Delta\psi$. Before doing that it is useful to calculate the size of a science pixel in terms of rotation angles, specifically arcsec. The geometry of Figure 24. is used to calculate this value; Figure 24. is a simple representation of a telescope, but not to scale, where f , is the focal length, l , is the length of a pixel and β is the angle that will define the dimension of the pixel in arcsec.

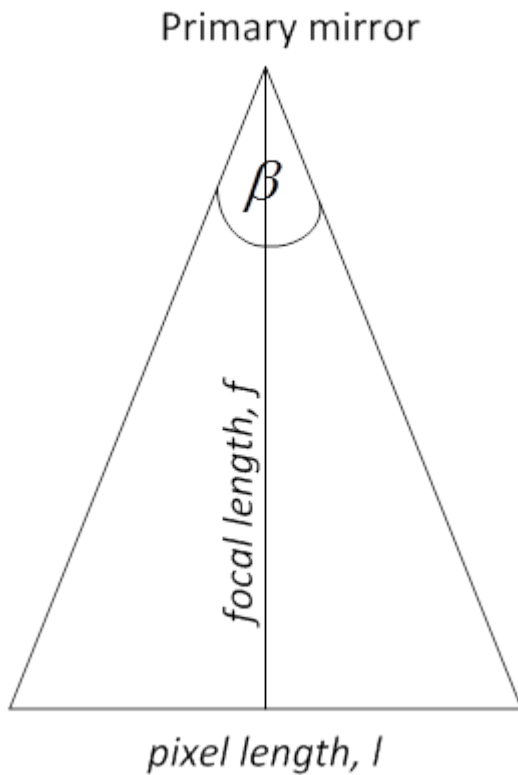


Figure 24. Simple representation of a telescope, (not to scale)

Using simple trigonometry β can be solved for by:

$$\tan\left(\frac{\beta}{2}\right) = \frac{l}{2f} \quad (37)$$

Since pixels are typically on the micrometer scale it is assumed that the $\beta / 2 \ll 1$ so β in radians is:

$$\tan\left(\frac{\beta}{2}\right) \approx \frac{\beta}{2} \therefore \beta = \frac{l}{f} \quad (38)$$

Based on convention, β is in arcsec, l is in μm and f , is in mm as in:

$$\beta(\text{arc-sec}) = 206.26 \frac{l(\mu\text{m})}{f(\text{mm})} \quad (39)$$

A similar technique and similar figure can be used to relate Δy and Δz to $\Delta\theta$ and $\Delta\psi$. To simplify the explanation it will be assumed that $\Delta\theta = \Delta\psi$, which also implies that $\Delta y = \Delta z$, so the equation for the lost area becomes:

$$A_{lost} = \frac{\pi\Delta y^2 + \pi\Delta z^2}{4} = \frac{\pi\Delta y^2}{2} \quad (40)$$

Figure 25. is a depiction of the shifted image on a pixel that can be used to solve for Δy in terms of the rotation $\Delta\theta$.

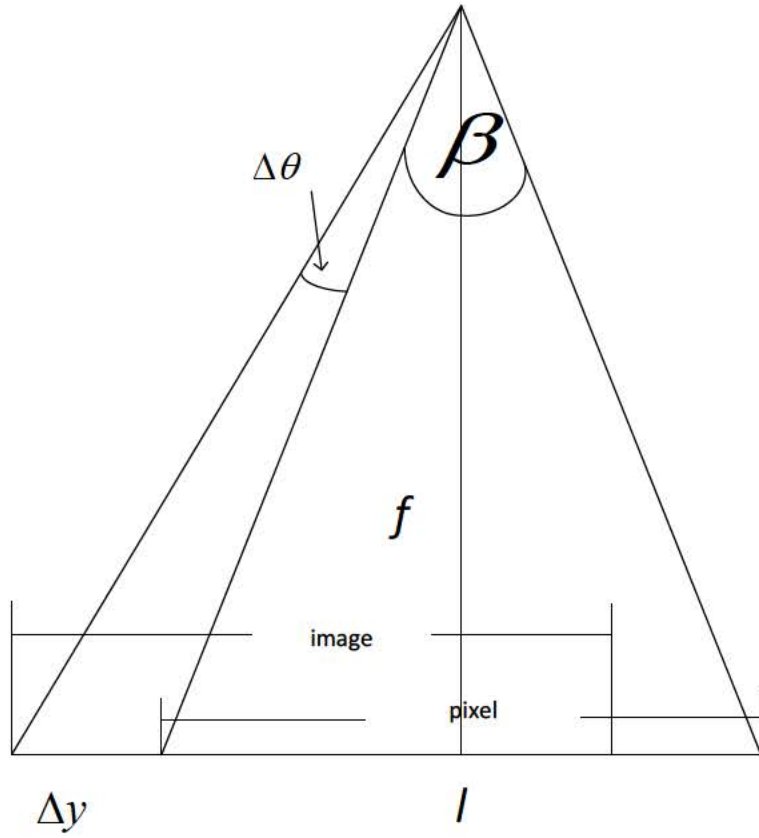


Figure 25. Solving for Δy , (not to scale)

Using a similar process as before when solving for l , one can solve for Δy :

$$\begin{aligned}
 \tan\left(\frac{\beta}{2} + \Delta\theta\right) &= \left(\frac{l/2 + \Delta y}{f}\right) = \frac{l}{2f} + \frac{\Delta y}{f} \\
 \frac{\beta}{2} + \Delta\theta \ll 1 \therefore \tan\left(\frac{\beta}{2} + \Delta\theta\right) &\approx \frac{\beta}{2} + \Delta\theta \\
 \frac{\beta}{2} + \Delta\theta &= \frac{l}{2f} + \frac{\Delta y}{f} \\
 \beta = \frac{l}{f} \therefore \Delta\theta(\text{arc sec}) &= 206.26 \frac{\Delta y(\mu\text{m})}{f(\text{mm})}
 \end{aligned} \tag{41}$$

It is important to note that although rotation is defined from the center of mass of the spacecraft, different components of the spacecraft, for example the primary mirror will be rotated by the same angle. Using the relationship derived in (41), (40) thus becomes:

$$A_{lost} = \frac{\pi \Delta y^2}{2} = \frac{\pi}{2} \left(\frac{f \Delta \theta}{206.26} \right)^2 \quad (42)$$

The original area can be defined in terms of the angular pixel length. If the radius of the original circle is defined as half the length of a pixel, l , used in Figure 24., the original area is:

$$A_0 = \frac{\pi(l)^2}{4} = \frac{\pi}{4} \left(\frac{f \beta}{206.26} \right)^2 \quad (43)$$

Finally, the first-order approximation pointing noise due to cross-boresight axes rotation defined in (33) is:

$$\sigma_{\text{pointing, noise}} = \frac{\rho_{\text{signal}} A_{lost}}{\rho_{\text{signal}} A_0} = \frac{\frac{\pi}{2} \left(\frac{f \Delta \theta}{206.26} \right)^2}{\frac{\pi}{4} \left(\frac{f \beta}{206.26} \right)^2} = \frac{2 \Delta \theta^2}{\beta^2} \quad (44)$$

(2) Effects of about boresight axis rotations. There is one more type of rotation to consider and that is about boresight axis, rotations around the x -axis. In order to understand this, Figure 26. shows a different perspective of a signal on a given pixel. This diagram shows the line, d , the distance from the center of the focal plane array to the center of the pixel of interest. The gray circle is the signal to be read.

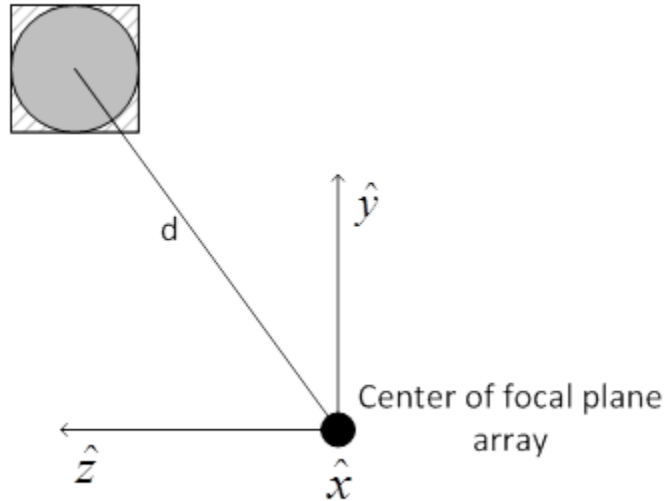


Figure 26. Image centered on a pixel away from the center of the focal plane array

If the CCD is rotated by some $\Delta\phi$, as shown in Figure 27., around the x -axis, then the center of the source will change. For actual systems, even if $d=0$, meaning the pixel center is at the center of the focal plane array, the rotation would create some noise due to the intra-pixel interactions, but for this first-order approximation those interactions are ignored, and $d>0$.

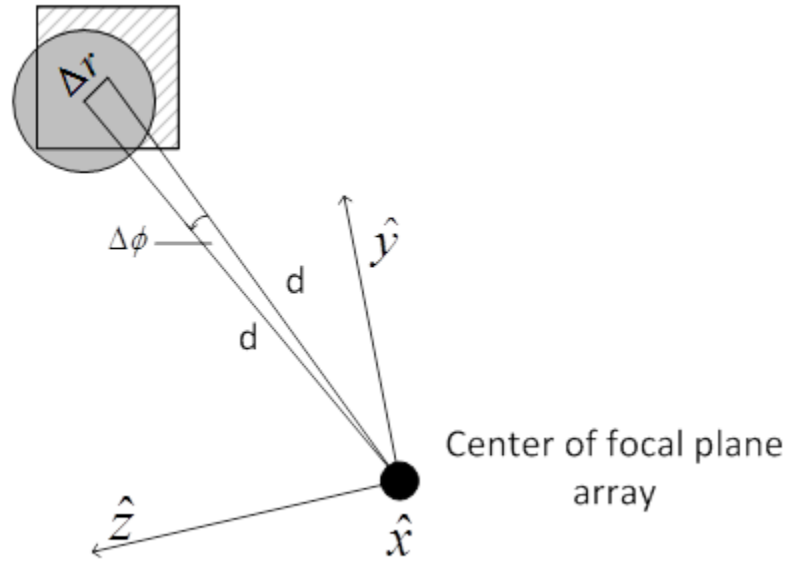


Figure 27. Image shifted after rotation of $\Delta\phi$

As shown in Figure 28., the lost area is very similar to that due to the cross-boresight rotations, therefore the same approximation technique of inscribing two circles is used.

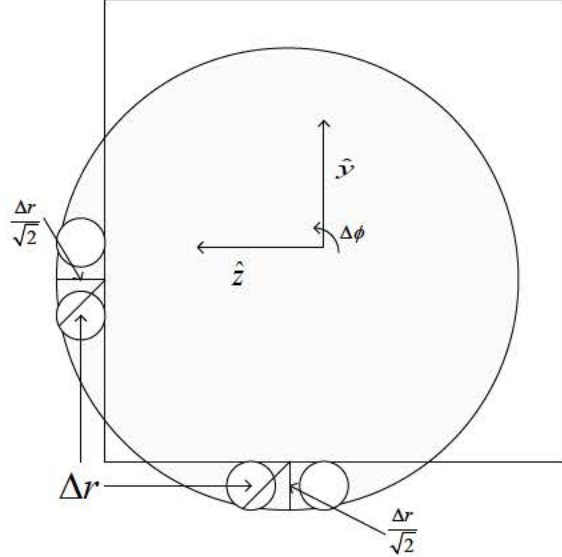


Figure 28. Visualization of A_{lost}

Using Figure 27., the lost area is:

$$A_{lost} = 4\pi \left(\frac{\Delta r}{2\sqrt{2}} \right)^2 = \frac{\pi \Delta r^2}{2} \quad (45)$$

Similarly to the approximation developed for cross-boresight it is useful to determine the relationship between Δr and $\Delta\phi$, which can be accomplished by using Figure 27..

$$\Delta r(\mu m) = d(mm) \frac{\Delta\phi(arc\ sec)}{206.26} \quad (46)$$

where the factor of 206.26 converts mm-arcsec into μm -rad. Therefore, the area lost due to about boresight axis rotations is:

$$A_{lost} = \frac{\pi \Delta r^2}{2} = \frac{\pi}{2} \left(\frac{d \Delta\phi}{206.26} \right)^2 \quad (47)$$

Using the original collection area, derived in (43), the first-order approximation pointing noise due to the about boresight axis rotation defined in (33) becomes:

$$\sigma_{\text{pointing, noise}} = \frac{\rho_{signal} A_{lost}}{\rho_{signal} A_0} = \frac{\frac{\pi}{2} \left(\frac{d \Delta\phi}{206.26} \right)^2}{\frac{\pi}{4} \left(\frac{f \beta}{206.26} \right)^2} = \frac{2(d \Delta\phi)^2}{(f \beta)^2} \quad (48)$$

(3) Comparing cross-boresight and about boresight losses. Two equations for pointing loss have been derived, one due to cross-boresight axes rotations and the other due to about boresight axis rotations. For small rotations, the cross-boresight axes and about boresight axis pointing noises can be superposed so the first order approximation of the total pointing noise is:

$$\sigma_{\text{pointing noise}} = \frac{2\Delta\theta^2}{\beta^2} + 2\left(\frac{d\Delta\phi}{f\beta}\right)^2 \quad (49)$$

It is beneficial to compare, how the two forms of pointing noise are related. The pointing noise contribution from the cross-boresight axes rotations and about boresight axis rotations can be compared by:

$$\eta = \frac{\sigma_{\text{pointing noise, cross}}}{\sigma_{\text{pointing noise, around}}} = \frac{2\left(\frac{\Delta\theta}{\beta}\right)^2}{2\left(\frac{d\Delta\phi}{f\beta}\right)^2} = \left(\frac{f\Delta\theta}{d\Delta\phi}\right)^2 \quad (50)$$

Using $f = 1399.20\text{mm}$, and $d = 150\text{mm}$ [47], which is approximately the farthest distance that a pixel could be from the center of the focal plane and assuming that $\Delta\theta = \Delta\phi$, the ratio, η , between the two pointing noises is:

$$\eta = \left(\frac{1399.20}{150}\right)^2 = 87 \quad (51)$$

Assuming the pointing errors are the same around all three axes, the pointing noise due to cross-boresight axes rotations is almost two orders of magnitude greater than the pointing noise from the about bore-sight axis rotations.

As shown in (51) if the rotations around all three axes are of the same order of magnitude the cross-boresight axes pointing noise is much greater, so with a fully functioning control system only the first term of (49) would provide a significant contribution.

It is important to emphasize the limitations of this approximation. It ignores intra-pixel and inter-pixel issues captured by the PRF, it simplifies the calculation of the loss in area, it assumes that the source spreads evenly and like a circle and it ignores the size of the pixel mask (the amount of pixels that the signal is spread over). The first limitation

may underestimate the error; extra losses may exist due to the interactions. The other limitations may overestimate the error. The assumption that the source spreads evenly ignores the fact that the outer concentration of electrons is actually lower than in the center of the real distribution of electrons. Furthermore, only examining the noise over one pixel implies that if the rotations are large enough the signal would be completely lost and this simplification also ignores the fact that the PSF can be spread out over many pixels. In fact for Kepler the PSF was designed to have ~95% of the signal strength spread over at most a pixel mask of 7x7 pixels [3]. The size of the pixel mask was ignored because it adds another level of complication, which cannot be accounted for without a simulation. Small drifts may actually have a much lower loss of electrons than predicted. This first-order approximation can provide an idea of the system's performance, but to truly understand the effects of motion, numerical analysis with the PSF and PRF is ultimately required.

c. Summary

Combining the read, dark current and pointing noise together provides:

$$\sigma_{\text{instrument, noise}}^2 = \sigma_{\text{read, noise}}^2 + \sigma_{\text{dark, noise}}^2 + \sigma_{\text{pointing, noise}}^2 = \left(\frac{e_{\text{read}}^-}{S} \right)^2 + \left(\frac{e_{\text{dark current}}^-}{S} \right)^2 + \left[\frac{2\Delta\theta^2}{\beta^2} + 2 \left(\frac{d\Delta\phi}{f\beta} \right)^2 \right]^2 \quad (52)$$

D. ANALYSIS OF KEPLER'S NOISE FLOOR

The first section of this chapter outlined the required design SNR and transit depth signal. The next sections discuss the signal and noise from the target star and the spacecraft pointing system. The following sections will utilize the developed equations to examine three different cases of Kepler: (1) Kepler's original mission, (2) original estimates of Kepler's ADCS degradation (3) K2 mission. This chapter will conclude with an exploration of the science capabilities for the first and third cases.

1. Case 1: Original Kepler Mission

The original Kepler mission can be examined based on the design requirements of Kepler. This ensures that the above equations, especially the approximation for pointing noise provide the expected results of around 20ppm for noise and a total SNR of at least 4

for an Earth-size planet in an Earth-like orbit around a Sun-like, G2V star, with a magnitude of 12.

a. Signal

Using the knowledge of a twelfth magnitude G2V star as the design standard (23) and the average transit of a planet of 6.5 hours [3] the number of electrons expected to be read by a pixel mask is:

$$\begin{aligned} S &= f_2 t \\ f_2 &= 10^{(-0.4(m_2 - 12))} f_{12} \\ m_2 &= 12, f_{12} = 2.1 \times 10^5 \frac{e^-}{s}, t = 6.5 \text{ hrs} \\ S &= 4.9 \times 10^9 e^- \end{aligned} \tag{53}$$

b. Shot Noise

The shot noise for this star can be calculated using (25):

$$\sigma_{\text{shot noise}} = \frac{1}{\sqrt{S}} = \frac{1}{\sqrt{4.9 \times 10^9}} = 1.4 \times 10^{-5} \tag{54}$$

c. Stellar Variability

As stated previously, stellar variability for every target star is unknown. Therefore, in the planning stages a constant value of 10 ppm for stellar variability is used [3]:

$$\sigma_{\text{stellar variability}} = 1 \times 10^{-5} \tag{55}$$

d. Read Noise

Read noise described above is a function of the operation of the CCD and as recently as 1996 there was no concern that read noise would be large enough to have an impact on the overall SNR [5]. Invariably, CCD technology has improved since that time, but for a conservative estimate this thesis will use the original design value of 1626 e⁻/hr [5] making read noise:

$$\sigma_{\text{read noise}} = \frac{1626 \frac{e^-}{hr} (6.5hr)}{4.9 \times 10^9 e^-} = 2.2 \times 10^{-6} \quad (56)$$

e. Dark Noise

Similar to read noise this thesis will use the estimate of dark current provided during the design of the Kepler mission of about $1880 \text{ e}^-/\text{hr}$ making [5] dark current noise:

$$\sigma_{\text{dark noise}} = \frac{1880 \frac{e^-}{hr} (6.5hr)}{4.9 \times 10^9 e^-} = 2.5 \times 10^{-6} \quad (57)$$

f. Pointing Noise and Pointing Requirements

The final component, before solving for the expected photometric precision for the original Kepler mission, is the pointing noise. So far it has been explained that the read noise and dark current contribute negligently to the noise floor due to careful CCD design. Similarly the pointing noise is within the control of the designers so the goal was to make the pointing noise negligible as well. A good way to do this would plan on the pointing noise being around one order of magnitude lower than the final desired photometric precision. Therefore, the design value of $\sigma_{\text{pointing noise}} < 5.0 \times 10^{-6}$ [5] was used.

Since the pointing noise has a direct impact on the pointing requirements one could use (49) to obtain an idea of the allowed maximum pointing error. Using (49) the first order approximation maximum allowed pointing error is:

$$5 \times 10^{-6} = \frac{2\Delta\theta_{\max}^2}{\beta^2} = \frac{2\Delta\theta_{\max}^2}{(3.98 \text{ arc sec})^2} \therefore \Delta\theta_{\max} \approx .006 \text{ arc sec} \quad (58)$$

In addition to obtaining this estimate it is possible to confirm the validity of this estimate and (49) by comparing it to the actual pointing accuracy design requirements of Kepler. The pointing accuracy requirement is to maintain pointing to be better than 0.009 arcsec , 3σ on the order of 30 minutes corresponding to the LC time [48]. The time scale for the pointing accuracy is 30 minutes instead of the 6.5 hours used throughout the rest

of this example. The explanation is that the 6.5 hours consists of 13 LCs, at the end of each LC the satellite can be slightly adjusted to ensure the target stars are on the original pixels, which reduces some of the expected noise effects due to pointing error. Alternatively the signal could be read from another set of pixels. Also as explained in the introduction after 30min an LC is read, so for pointing purposes the measurements are over until the next LC. In addition, using the first-order approximation level the signal strength does not have an effect, so the only concern is the total expected drift per integration, which is the time of the LC. Therefore, it is sufficient to quantify the pointing accuracy per LC. When one compares the calculated pointing accuracy from (58) to the actual pointing requirement the results are:

$$\frac{\Delta\theta_{\text{max calculated}}}{\Delta\theta_{\text{actual}}} = \frac{.006 \text{arc sec}}{.009 \text{arc sec}} = \frac{2}{3} \quad (59)$$

First the comparison show that the first-order approximation is the same order of magnitude, milliarcsec, and second it is within 33% of the actual requirement. This means that even by simplifying the pointing noise to a geometrical calculation and ignoring the PRF and PSF one can have a good idea of what pointing stability is required to achieve a certain pointing noise.

g. Total Noise and SNR

The noise values calculated above provide a total noise of:

$$\sigma_{\text{total noise}} = \sqrt{(1.4 \times 10^{-5})^2 + (1.0 \times 10^{-5})^2 + (2.5 \times 10^{-6})^2 + (2.2 \times 10^{-6})^2 + (5.0 \times 10^{-6})^2} = 18 \text{ppm} \quad (60)$$

This is reasonable; as it is about the 20ppm design value. Assuming a signal equal to the transit depth of Earth the SNR is:

$$SNR = \frac{84 \text{ppm}}{18 \text{ppm}} = 4.7 \quad (61)$$

This value is close to the expected SNR of 4 discussed previously. However, it is a bit higher.

h. Summary

This example provided several useful takeaways. It demonstrated how the noise calculations were used and identified baseline values for stellar variability, read and dark current noise that will be used for the next two cases. It also validated the first-order approximation for the pointing noise and provided an improvement on that approximation. It also proved that it is possible to achieve the necessary SNR=4 to detect an Earth-like planet in an Earth-like orbit around a Sun-size star. Using the method above it is possible to calculate the ability to detect other size planets around other size stars with different pointing accuracies.

2. Case 2: Original Estimates of ADCS Degradation

As stated previously, the original Kepler mission was deemed to be no longer possible due to the failure of two out of the original four reaction wheels. This failure reduced the pointing accuracy that was achievable with the Kepler spacecraft, increasing the pointing noise and removing the ability to conduct the original Kepler mission. This case will demonstrate a reason why the original Kepler mission was deemed no longer viable based on the original estimates of ADCS degradation.

For this explanation the same target star, one with a magnitude of 12 was used, as in the original Kepler mission. The signal from the star and the noise values except for pointing noise are in Table 2. . Although not an exact comparison to Case 1 this case will be examined using a time scale of one minute. The original predicted values of the reduced drift were about one arcsec/min [14] and as will be shown, one arcsec over a minute will provide a pointing noise high enough to ruin the mission.

Table 2. Case 2: signal and noise values for 12th magnitude star

Star Signal (e^-)	1.3×10^7
Shot Noise	2.8×10^{-4}
Stellar Variability	1.0×10^{-5}
Read Noise	2.2×10^{-6}
Dark Noise	2.5×10^{-6}

In Table 2. , as expected, the star signal decreased because the time was less than the original mission and subsequently the shot noise increased. The read noise and dark noise remain the same since both the signal and the amount of extra electrons were scaled by the same factor, canceling the change. As mentioned previously the stellar variability is assumed constant at 10 ppm.

The only component left to evaluate before calculating the total noise is the pointing noise. In the original Kepler mission the ADCS was able to control all three axes to an accuracy of <0.009 arcsec, however now with the two failed wheels it is only possible to control rotations around two axes to that type of accuracy [13]. As will be explained in a later chapter, the wheels will control rotations around the z -axis and one other axis. The contribution to pointing noise due to cross-boresight rotations is so much worse than the contribution due to about boresight axis pointing noise, so it was decided to also control rotations about the y -axis [13]. The new pointing estimates of 1 arcsec will be assumed to be the pointing stability about the x -axis and 0.009 arcsec will be used for the y -axis and z -axis. Using (49) the first order approximation pointing noise is

$$\sigma_{\text{pointing noise}} = \frac{2((150\text{mm})1\text{arc sec})^2}{((1399.20)3.98\text{arc sec})^2} + \frac{2(.009\text{arc sec})^2}{(3.98\text{arc sec})^2} = 1.5 \times 10^{-3} \quad (62)$$

This approximation provides a result close to the original predicted estimate of NASA of a pointing noise of about 1000ppm for the degraded pointing system [14]. This calculated value is within 50% of the estimate from NASA, which is satisfactory and not surprisingly worse than the 30% difference between actual and estimated from Case 1. As

the drift gets worse the limitations of the simplifications that went into developing (48), that were accounted for in [14], will become more exaggerated. Similar to the original Kepler estimate, the approximation is not exact but it provides an ability to understand the impact of degraded pointing noise on the original mission.

The new pointing noise value is much larger than the noise from the other components so one can ignore the other components of noise and assume the total noise is roughly equivalent to the pointing noise. The total noise for a twelfth magnitude G2V star then is about 1500ppm, which would provide an SNR of 0.056. It is clear that continuing the original mission is not feasible since the noise is greater than the desired detection signal. This value is only for a one minute time frame, which means it would expectedly be significantly worse for the 30min LC co-added to the 6.5hr transit used in Case 1.

3. Case 3: The K2 Mission

After different unique engineering solutions were implemented, the pointing accuracy could be improved to approximately 10arcsec over a period of 8 hours [13]. This is about 0.63arcsec of drift per each 30min LC. Similar to the previous two cases this case will be examined using a twelfth magnitude star. However, this case, like Case 1, will return to the original 6.5hr timeline, while using the 30min drift value. Table 3. lists the signal and noise values, including the effects of the 0.63arcsec pointing error.

Table 3. Case 3: signal and noise values for 12th magnitude star

Star Signal (e^-)	4.9×10^9
Shot Noise	1.4×10^{-5}
Stellar Variability	1.0×10^{-5}
Read Noise	2.2×10^{-6}
Dark Noise	2.5×10^{-6}
Pointing Noise	5.8×10^{-4}
Total Noise	5.8×10^{-4}

As expected, the values for all sources except the pointing noise and total noise match the results from Case 1. Similar to Case 2, the pointing noise dominates the other noise values so the total noise is essentially pointing noise. The pointing noise, although better than Case 2, is still much worse than Case 1, and is greater than the 84 ppm transit depth of an Earth-like planet giving SNR of 0.15. It is once again clear from this simple approximation that the original science is not feasible.

E. SMALLEST DETECTABLE PLANET

The analysis above focused on the original design target star of twelfth magnitude. In addition, it used the first-order approximation to analyze the ability to conduct the desired mission, which at least in Case 1 and Case 2 had actual values to compare the results to, providing confidence in the approximation. In addition to examining the state of Kepler for the design star there are at least two more interesting aspects to explore using the method described above: (1) a comparison of the ability to detect planets and (2) a comparison of photometric precision to actual data.

The comparison of the ability to detect planets will still assume the star is about the same size as the Sun but could have a magnitude ranging from 12 to 16.5. The goal is to determine what the planet size in Earth radii needs to be to ensure the SNR is 4.0 or greater. The pointing noise will be based on the information outlined in Case 1 and 3, corresponding to an accuracy of 0.009 arcsec for Case 1, and 0.63 arcsec for Case 3. Case 2 will not be in this comparison because the accuracy over 30 minutes is so poor it would provide significantly different results than the other 2 cases and not provide any useful information. The results are shown in Figure 29. .

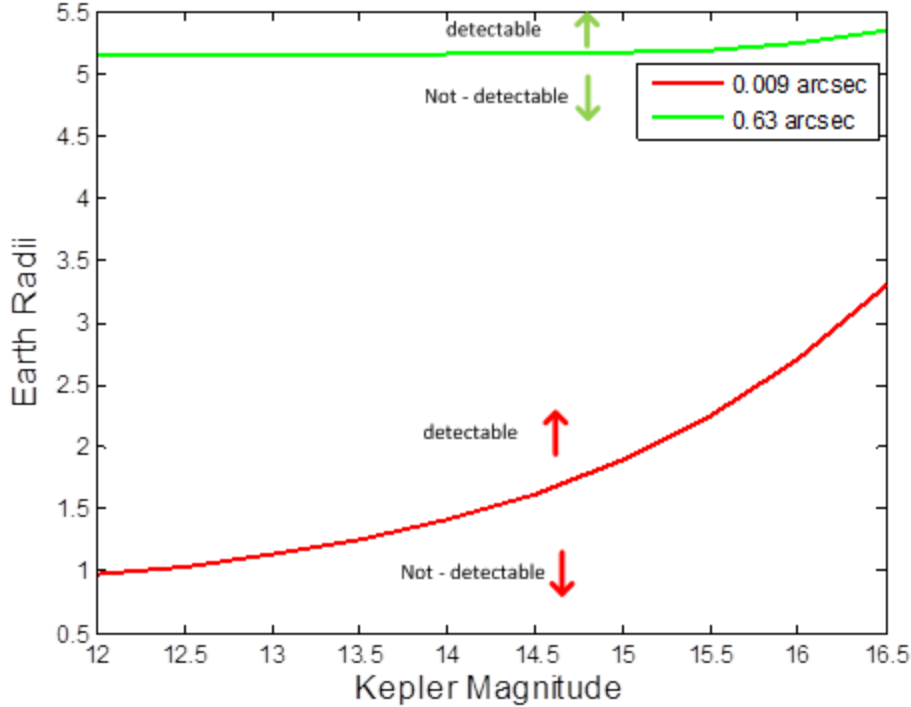


Figure 29. Planet detection ability for different drift rates per LC

As designed, Case 1 for a twelfth magnitude star allows for the detection of a planet equivalent to about $1R_{\oplus}$ with an SNR of 4. Also, as the magnitude increases, the star appears dimmer, so fewer electrons are read for that star and the minimum size of a detectable planet steadily increases to about $3.5R_{\oplus}$ when the magnitude is >16 . Case 3, using the first-order approximation, predicts that at best a planet with a radius around $5.1R_{\oplus}$ can be detected with an SNR of 4. However, unlike the steady increase in Case 1, the size of the detectable planet is about the same until the Kepler magnitude increases beyond 15.5; this is because the estimated pointing noise is so great that all other noise is negligible in comparison until the star dims significantly.

As shown above, it is possible to predict expected science capability using the pointing noise approximation, but the question remains how well the analysis compares to actual data. Figure 30. is a plot of the predicted photometric precision values using the equations provided in this thesis for Case 1 and Case 3 overlaid with actual Kepler and K2 data obtained from [46]. The red circles represent data from when Kepler had three

functioning wheels and were carefully selected G type stars [46]. The green circles are from the K2 mission using two-wheels and coarse pointing, but for stars of unknown variability and class. The blue data points are also from K2, but are based on fine pointing results, which use optimized apertures [46]. The difference between coarse pointing and fine pointing precision has to do with the use of the FGS.

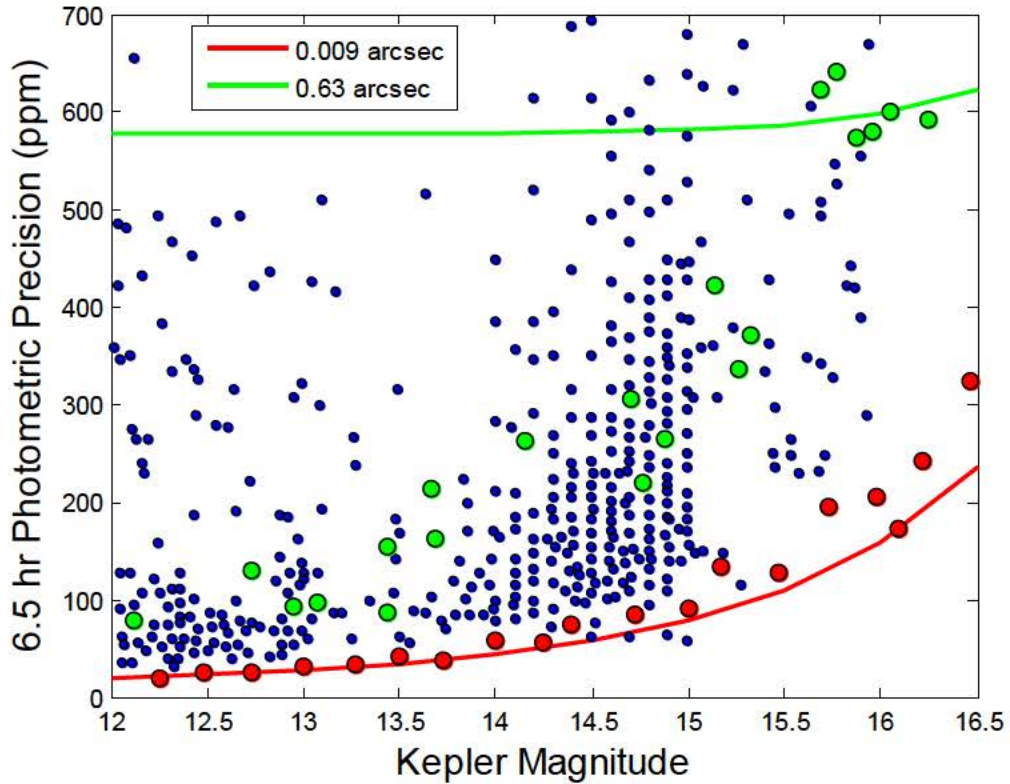


Figure 30. Predicted photometric precision vs. actual data, after [46]

Case 1, as expected, closely follows the empirical data for the G type stars from the original Kepler mission. There is a slight deviation that occurs as the magnitude increases, which could be due to several factors including a difference in stellar variability or differences between the approximation and actual noise values increase as the star dims. Case 3 on the other hand does not closely correlate to the K2 empirical data. This is not too surprising; the data from the K2 mission were carefully selected and included software improvements that reduced the effects of pointing noise [46].

Furthermore, the fine pointing targets were read using different optimized apertures [46], which put into question the simplification made here that removed the need for the pixel mask. There are improvements to the data processing, mainly functions of software that cannot be accounted for in the geometrical approximation for pointing noise provided above. This emphasizes the limited scope of this approximation. However, the results are satisfactory in the sense that they provide an estimate of an upper bound of possible science that can be performed by the K2 mission.

F. SUMMARY

This chapter outlined the requirements driving the design of Kepler. It also explored the effects of the degradation in pointing accuracy due to reaction wheel failure. It demonstrated the loss of ability of possible science that occurred from Kepler to K2. The reaction wheels were installed to provide accurate pointing capabilities and pointing precision. The next chapter will discuss the physics of solar torque, which is the main factor that limits pointing accuracy and precision achievable with the two remaining reaction wheels.

THIS PAGE INTENTIONALLY LEFT BLANK

V. SOLAR TORQUE ON SPACECRAFT

This chapter begins with a brief outline of torque and space environment disturbances. These two topics are just an introduction to the main purpose of this chapter, which is to describe the physics behind solar torque disturbances on spacecraft.

A. TORQUE

Torque is a phenomenon caused by the application of a force on an object offset from a fixed point of rotation, in an environment like space, offset from an object center of gravity. The application of a force will induce a rotation dependent upon the direction of the force and the perpendicular “moment arm.” Mathematically, torque is defined as:

$$\vec{T} = \vec{r} \times \vec{F} \quad (63)$$

By convention, a counter-clockwise torque is defined as a positive torque, while a clockwise torque is negative as depicted in Figure 31. .

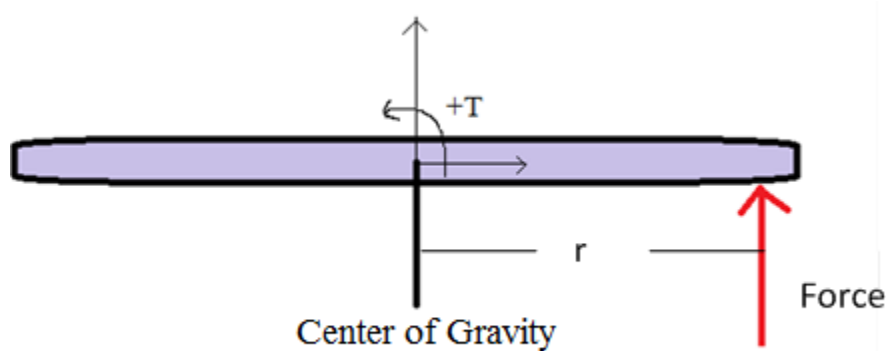


Figure 31. Example of force inducing a counter-clockwise torque

B. SPACE ENVIRONMENTAL DISTURBANCE TORQUE

Every spacecraft is subject to any combination of several environmental disturbances that can induce a torque about the spacecraft body. As shown in Figure 32. , the environmental disturbances are: (1) solar radiation pressure, (2) atmospheric drag, (3) magnetic field torque, (4) gravity gradient.

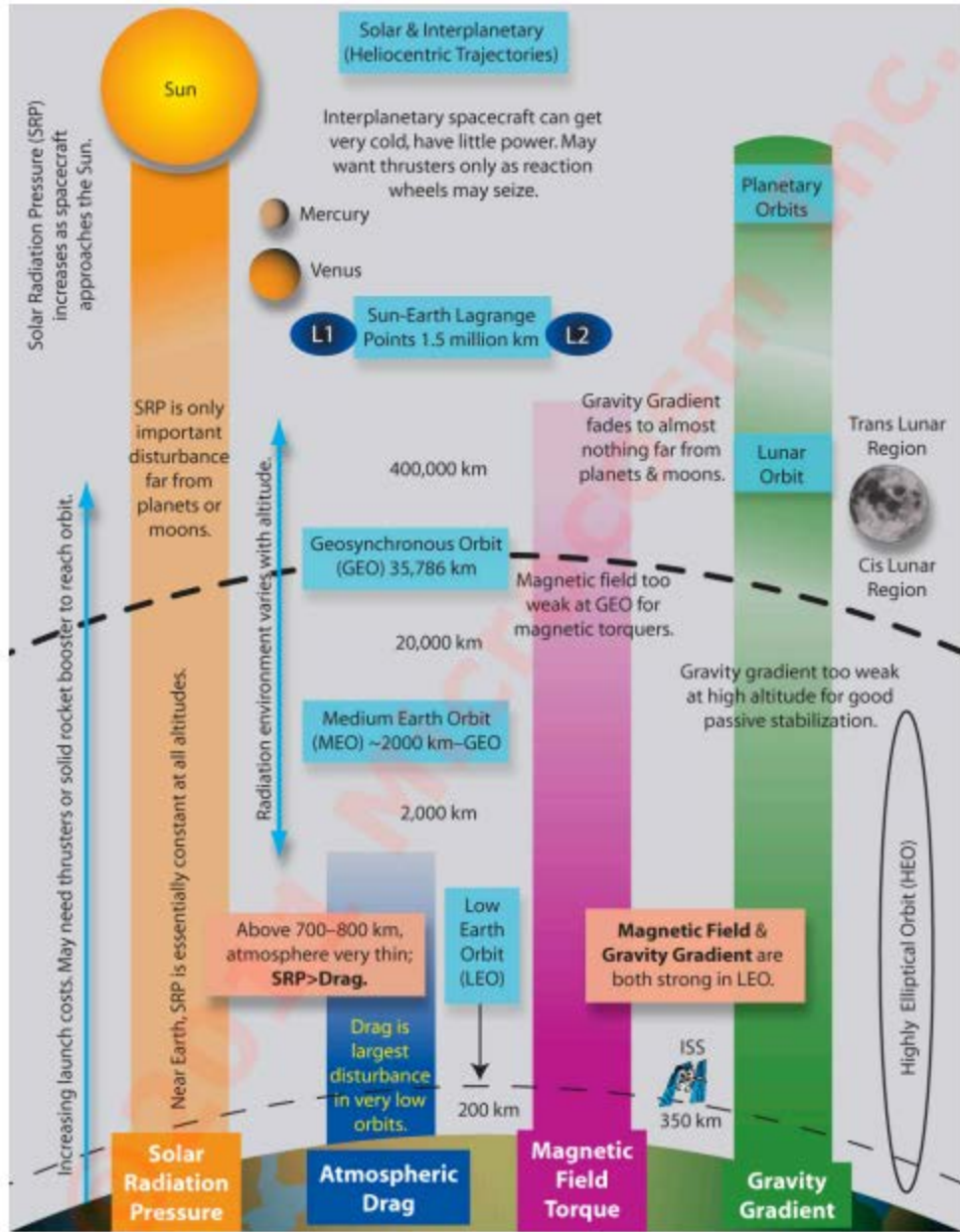


Figure 32. Effects of major environmental disturbance torques on spacecraft, from [49]

As Figure 32. shows, the dominant environmental disturbance torque important to spacecraft not in the vicinity of any large celestial body is the torque due to solar radiation pressure. Due to its orbit this is the only environmental disturbance torque relevant to the Kepler spacecraft [13].

C. RADIATION DISTURBANCE TORQUE

As Spence explains, “radiation incident on a spacecraft’s surface produces a force which results in a torque about the spacecraft’s center of mass” [50]. For Kepler, this incident radiation can come from direct solar photon radiation, referred to as solar radiation pressure above, and radiation from the spacecraft itself. In general, the torque due to the solar radiation pressure is at least an order of magnitude larger [51], so solar torque effects will be the main focus of this thesis.

1. Force Due to Electromagnetic Radiation

According to classical electricity and magnetism theory, when electromagnetic radiation impinges on an object the radiation is scattered “due to the combined effects of all the electrons” [52]. There are three predictions based on this explanation of scattering that did not coincide with experiment:

[one] that the energy scattered by an electron traversed by an X-ray beam of unit intensity is the same whatever may be the wave-length of the incident rays... [two] when the X-rays traverse a thin layer of matter, the intensity of the scattered radiation on the two sides of the layer should be the same... [three] only a small part, if any, of the secondary X-radiation is of the same wave-length as the primary. [52]

Because experiments failed to confirm these predictions Arthur H. Compton realized that the classical explanation was insufficient and offered a quantum mechanics view on radiation scattering [52]. Compton proposed treating the electromagnetic quanta, commonly referred to as photons, as completely interacting with one electron, vice examining their effect based on interactions with all the electrons. This interaction is shown in Figure 33. .

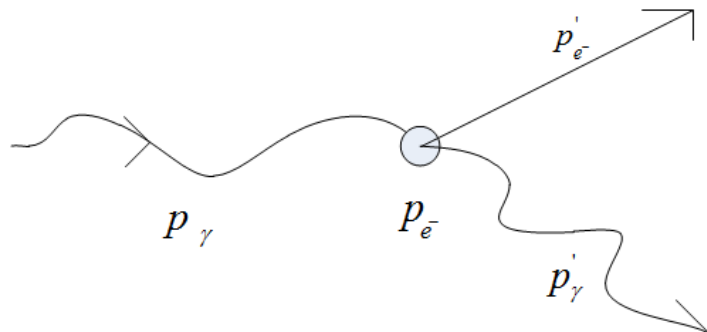


Figure 33. Schematic of Compton scattering.

Figure 33. shows the photon, γ , representing the electromagnetic energy, interacting with a single electron, e^- . This interaction can be examined based on the conservation of energy, E , and the conservation of momentum, p :

$$\begin{aligned} p_\gamma + p_{e^-} &= p'_\gamma + p'_{e^-} \\ p_{e^-} &= 0 \therefore p_\gamma = p'_\gamma + p'_{e^-} \\ E_\gamma + E_{e^-} &= E'_\gamma + E'_{e^-} \end{aligned} \tag{64}$$

The photon, has a momentum and energy dependent on wavelength, λ :

$$\begin{aligned} E &= \frac{hc}{\lambda} \\ p &= \frac{h}{\lambda} \end{aligned} \tag{65}$$

where h , is Planck's constant, and c , is the speed of light.

When the photon interacts with the electron it transfers some momentum and energy to the electron. Since the photon loses momentum and energy to the electron based on (65) the wavelength of the photon must also change so Compton's theory explains why the secondary radiation is of a different wavelength than the primary.

Compton's theory also explains the other two problems mentioned above [52], however, for the purposes of this thesis that part of the analysis by Compton is not relevant so it will not be discussed here.

Compton's theory showed that a change in momentum occurs due to the interaction between a photon and electron. In addition, it is known that a change in momentum means a force is exerted on an object:

$$F = \frac{dp}{dt} \tag{66}$$

where F is the force exerted on an object and $\frac{dp}{dt}$ is the change in momentum per unit time.

Combining these two ideas, it can be deduced that a force is induced on an electron due to the change in momentum, however here it is of interest to determine the force produced by many photons incident on a surface, which has many electrons. This requires the ability to calculate the force due to the combination of many photons from a single source, for example the Sun.

2. Irradiance of Sun

The first step to calculate the force is to determine the irradiance of the Sun. The irradiance captures information based on all the photons emitted by a source so it will allow the force due to many photons to be calculated.

It is a good approximation to model the Sun as a blackbody [53]. Based on this assumption if one knows the temperature of the Sun, it is possible to determine the Sun's irradiance based on blackbody radiation theory.

The spectral irradiance is defined as:

$$I(\lambda, T) = \frac{8\pi hc^2}{\lambda^5} \frac{1}{e^{\frac{hc}{\lambda kT}} - 1} \quad (67)$$

where I is the power per area per wavelength, with SI units of W/m^3 , h is Planck's constant, λ is the wavelength, c is the speed of light, k is Boltzmann's constant and T is the temperature.

For a blackbody (67) can be integrated over all wavelengths to derive an equation for irradiance, L , solely dependent on temperature [53]:

$$L(T) = \int_{-\infty}^{\infty} \frac{8\pi hc^2}{\lambda^5} \frac{1}{e^{\frac{hc}{\lambda kT}} - 1} d\lambda = \frac{2\pi^5 k^4}{15 h^3 c^2} T^4 \quad (68)$$

The constants in (68) are commonly combined and referred to as Stefan-Boltzmann's constant:

$$\sigma = \frac{2\pi^5 k^4}{15 h^3 c^2} \approx 5.67 \times 10^{-8} \frac{\text{W}}{\text{m}^2 \text{K}^4} \quad (69)$$

Using (69), (68) can be written in the more compact form of:

$$L(T) = \sigma T^4 \quad (70)$$

Throughout many years of observation and measurement the Sun's surface temperature has been measured to be about 5778K [28].

Using the knowledge that electromagnetic radiation is an inverse square law it is possible to determine the irradiance of the Sun at the orbit of the Earth, which roughly corresponds to the same orbit as Kepler as shown in (71).

$$L(T)_{\text{Earth}} = \frac{L(T)_{\text{Sun}} r_{\text{Sun}}^2}{d_{\text{Sun-Earth}}^2} \approx 1367 \frac{W}{m^2} \quad (71)$$

If the irradiance of the Sun at the Earth can be converted into a pressure then one can calculate the resultant force acting on an object such as a solar panel. The advantage of solving for pressure is it maintains the ability to examine any arbitrary surface. The two important relationships necessary for this analysis are the relationships between work, W , force, F and velocity, v , and force and pressure, P , as shown in (72) and (73).

$$W = F \cdot v \quad (72)$$

$$F = PA \quad (73)$$

If (71) is redefined, in terms of work, the solar radiation pressure at the Earth's orbit can be solved. This is approximately the same as the radiation pressure at Kepler's orbit as shown in (74). The computation requires dividing the irradiance by the speed of light.

$$\begin{aligned} L(T)_{\text{Earth}} &\approx L(T)_{\text{Kepler}} = \frac{W}{A} \approx 1367 \frac{W}{m^2} \\ \frac{W}{Ac} = \frac{F}{A} = P &= \frac{1367 \frac{W}{m^2}}{c} = \frac{1367 \frac{W}{m^2}}{3 \times 10^8 \frac{m}{s^2}} \approx 4.557 \times 10^{-6} \frac{N}{m^2} \end{aligned} \quad (74)$$

Utilizing the results of (74), it is possible to find the force on any arbitrary surface area in an orbit at the distance of the Earth from the Sun. This is possible by using the pressure and treating it as if it acts at an average point called the center of pressure. The center of pressure corresponds to the centroid of the surface area.

3. Force from Direct Solar Photon Radiation

The relationship between solar radiation pressure and force as defined in (73), is a simplification. In reality the angle between the surface and incident photons is important

as well as the surface's material properties. Due to the material properties "the [solar photon radiation] forces may be modeled adequately by assuming that incident radiation is either absorbed, reflected specularly, reflected diffusely or some combination" [51] as depicted in Figure 34. .

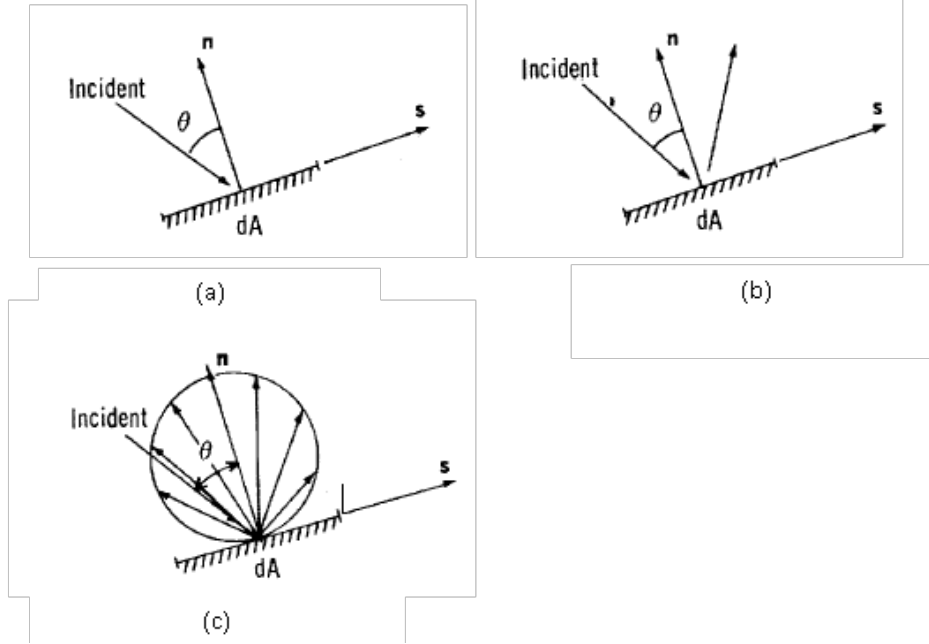


Figure 34. Depiction of the three main types of incident solar radiation effects:
 (a) absorbed radiation; (b) specularly reflected radiation; (c) diffusely reflected radiation, after [51]

The forces from incident solar radiation on a small surface are due to absorption, specular reflection, and diffuse reflection as defined in (75) below. Important parameters to understand (75) are: the photon pressure, P , defined in (74), the absorption coefficient, ρ_α , the specular reflection coefficient, ρ_s , the diffuse reflection coefficient, ρ_d , the Sun vector, \hat{S} , the vector normal to the incident surface, \hat{n} and an element of the area of the incident surface, dA .

$$\begin{aligned}
 df_\alpha &= -P\rho_\alpha \cos(\theta)\hat{S}dA \\
 df_s &= -2P\rho_s \cos^2(\theta)\hat{n}dA \\
 df_d &= -P\rho_d \left(\frac{2}{3}\cos(\theta)\hat{n} + \cos(\theta)\hat{S} \right) dA
 \end{aligned} \tag{75}$$

The three coefficients used in (75) must satisfy (76), which is based on the conservation of energy. In this description, the incident photons must be absorbed, specularly reflected or diffusely reflected. The three coefficients correspond to the percentage of photons that are either absorbed or reflected

$$\rho_a + \rho_s + \rho_d = 1 \quad (76)$$

The angle θ used in (75) is illustrated in Figure 35. .

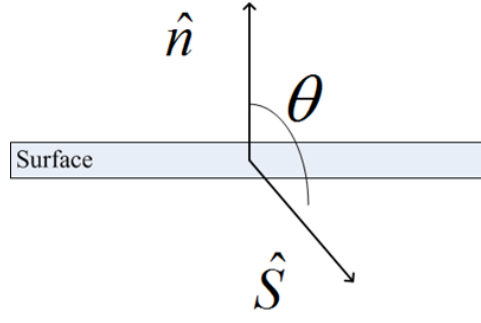


Figure 35. Angle between Sun vector, \hat{S} , and the normal, \hat{n} , to the surface

The total force can be calculated by combining the three equations of (75) and integrating over the surface:

$$F = -P(\hat{S} \cdot \hat{n}) \int \left[\rho_a \hat{S} + 2\rho_s (\hat{S} \cdot \hat{n}) \hat{n} + \rho_d \left(\frac{2}{3} \hat{n} + \hat{S} \right) \right] dA \quad (77)$$

If the surface is a flat plate, which as will be seen later is the main component that is being analyzed then (77) simplifies to (78), where A is the surface area of a flat plate. If the surface is more complicated, further derivation is required.

$$F = -PA(\hat{S} \cdot \hat{n}) \left[\rho_a \hat{S} + 2\rho_s (\hat{S} \cdot \hat{n}) \hat{n} + \rho_d \left(\frac{2}{3} \hat{n} + \hat{S} \right) \right] \quad (78)$$

If the Sun vector is defined as being from the spacecraft body to the Sun then (78) is valid when (79) is satisfied. This is because the force only acts on one side of the plate corresponding to the direction of \hat{n} .

$$0 \leq \hat{S} \cdot \hat{n} \leq 1 \quad (79)$$

4. Defining the Sun-Vector

a. Definition Based on Direction Cosine Matrix

In addition to defining the force incident on the spacecraft, it is necessary to define the Sun vector. As shown in Figure 36, a reference coordinate system is chosen such that the y -axis always points towards the Sun, regardless of the position of the satellite in the orbit. This choice is due to the heliocentric orbit of Kepler, and that the normal of the main solar panel of the spacecraft lies roughly along the y -axis.

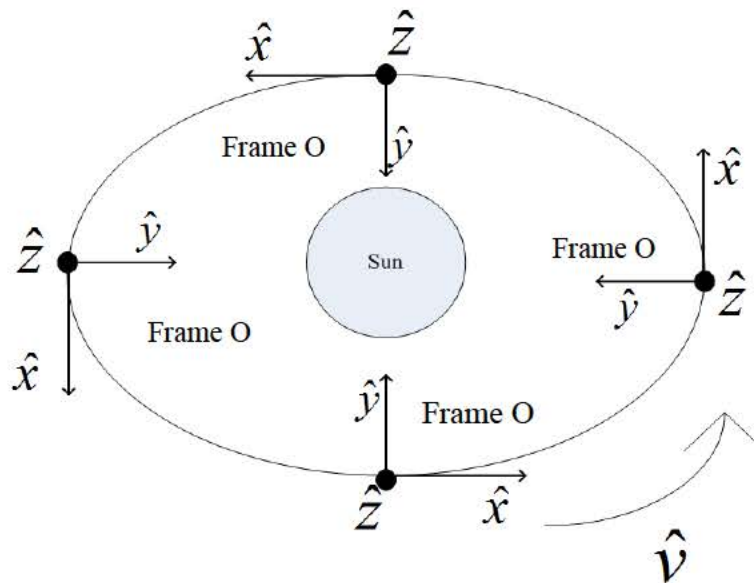


Figure 36. Depiction of Frame O in different orientations in Kepler's heliocentric orbit

Using Frame O , as the frame of reference, one can define the Sun vector, throughout the orbit as:

$${}^O\hat{S} = [0; 1; 0] \quad (80)$$

In addition to defining an orbit reference frame, a body frame, referred to as Frame B , needs to be defined that will account for rotations of the spacecraft, this is depicted in Figure 37. .

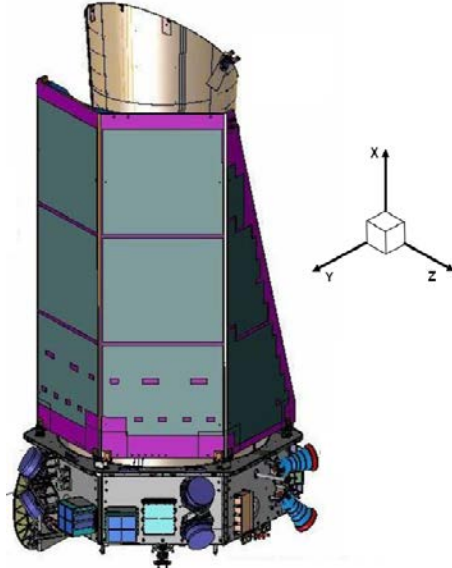


Figure 37. Definition of Frame B , centered on the spacecraft body,
from [3]

Next, it is necessary to define the relationship between Frame O and Frame B in order to convert the Sun vector defined in (80), from Frame O into Frame B . The relationship is based on the difference in orientation between Frame O and Frame B . The difference in orientation can be identified by three rotation angles: ϕ , the rotation angle around the x -axis, also referred to as elevation, θ , the rotation angle around the y -axis, and ψ , the rotation angle around the z -axis, also referred to as azimuth. Figure 38. through Figure 40. illustrate a 1–3–2 rotation, one of several rotation schemes. A 1–3–2 rotation consists of a rotation around the x -axis followed by a rotation around the new z -axis and finally a rotation around the new y -axis. This rotation sequence is the rotation sequence used throughout the remainder of this thesis.

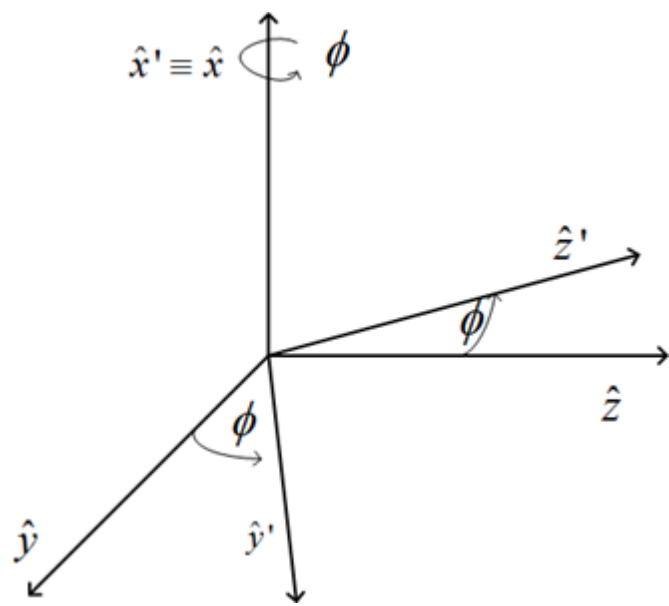


Figure 38. First rotation - rotation by ϕ around the x -axis

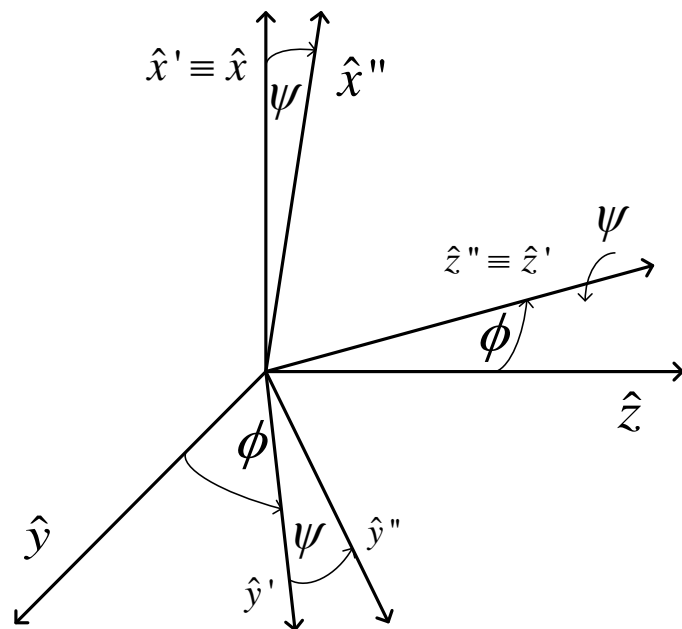


Figure 39. Second rotation - rotation by ψ around the z' -axis

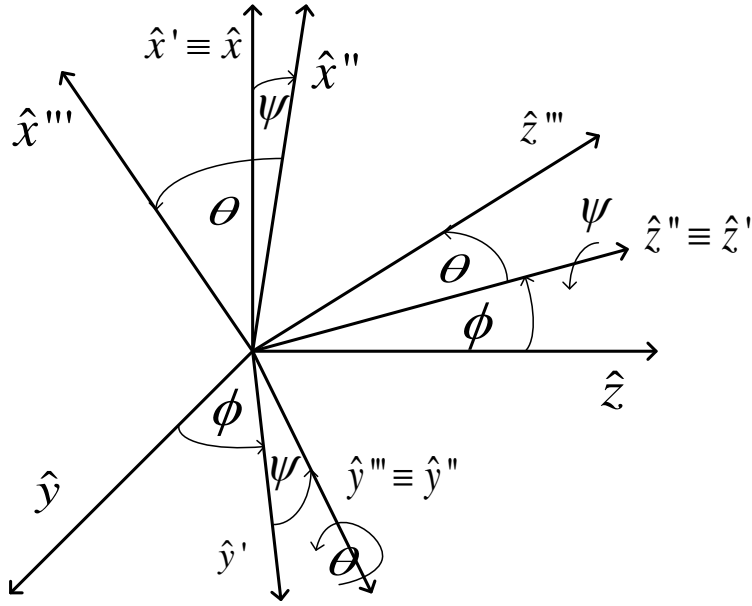


Figure 40. Third rotation—rotation by θ around the y'' -axis

Using the rotation sequence described above it is possible to derive an equation that will transfer the Sun vector from Frame O to Frame B :

$${}^B\hat{S} = C_{BO}(\theta, \psi, \phi) {}^O\hat{S} = C_2(\theta)C_3(\psi)C_1(\phi) {}^O\hat{S} \quad (81)$$

The operators that describe the rotations are commonly referred to as Direction Cosine Matrices and are:

$$\begin{aligned} C_x = C_1 &= \begin{bmatrix} 1 & 0 & 0 \\ 0 & \cos(\phi) & \sin(\phi) \\ 0 & -\sin(\phi) & \cos(\phi) \end{bmatrix} \\ C_y = C_2 &= \begin{bmatrix} \cos(\theta) & 0 & -\sin(\theta) \\ 0 & 1 & 0 \\ \sin(\theta) & 0 & \cos(\theta) \end{bmatrix} \\ C_z = C_3 &= \begin{bmatrix} \cos(\psi) & \sin(\psi) & 0 \\ -\sin(\psi) & \cos(\psi) & 0 \\ 0 & 0 & 1 \end{bmatrix} \end{aligned} \quad (82)$$

Evaluating (81) using the transformations in (82) gives:

$${}^B\hat{S}(\theta, \psi, \phi) = C_{BO}(\theta, \psi, \phi) {}^O\hat{S} = \begin{bmatrix} \sin(\phi)\sin(\theta) + \cos(\phi)\cos(\theta)\sin(\psi) \\ \cos(\phi)\cos(\psi) \\ \cos(\phi)\sin(\psi)\sin(\theta) - \cos(\theta)\sin(\phi) \end{bmatrix} \quad (83)$$

Due to operational requirements of the Kepler spacecraft, its nominal orientation is with the x -axis in the anti-velocity direction; this can be accounted for with a rotation of $\theta = \pi$. At this point, it will be assumed that Kepler will always point in the anti-velocity direction, therefore, (83) can be simplified into:

$${}^B\hat{S}(\psi, \phi) = \begin{bmatrix} -\cos(\phi)\sin(\psi) \\ \cos(\phi)\cos(\psi) \\ \sin(\phi) \end{bmatrix} \quad (84)$$

It is useful to check (84) through several simple orientations to ensure that the results from the equation are correct; these orientations are shown in Figure 41. and described in Table 4. . As Table 4. shows, the results from (84) matches the predicted values.

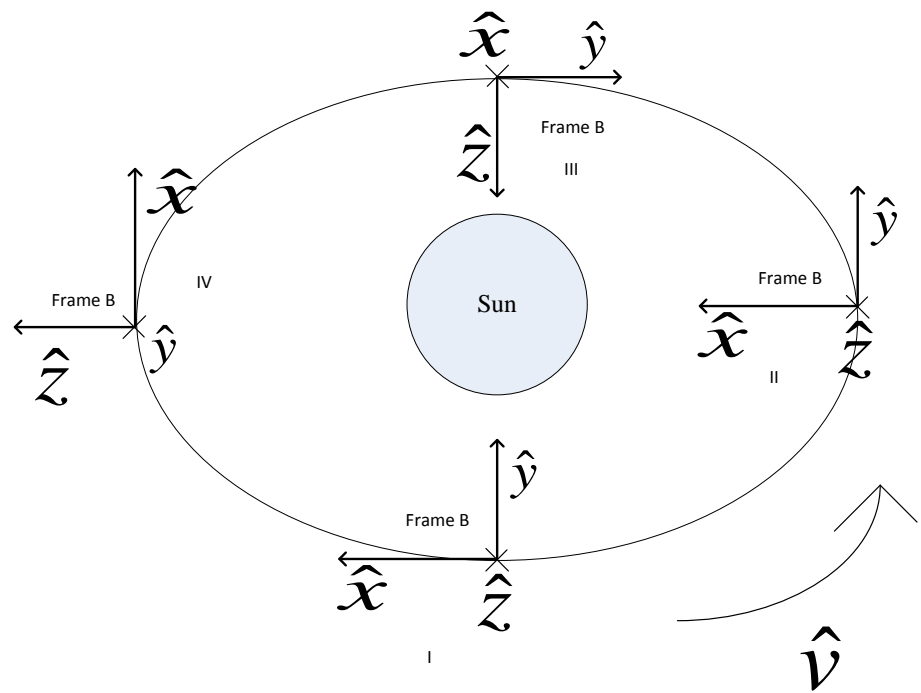
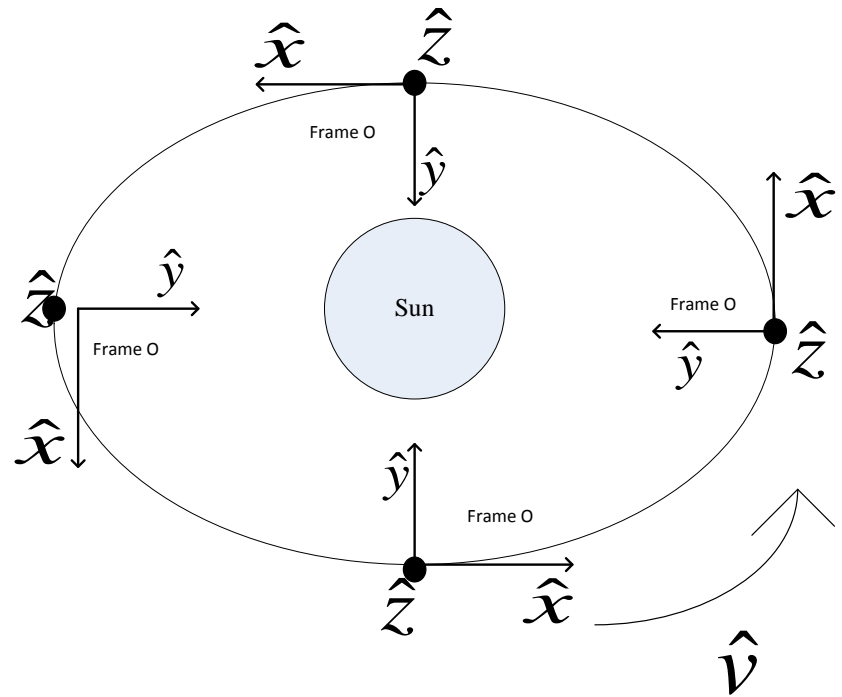


Figure 41. Validation rotations

Table 4. Analysis of the different orientations in Figure 3.4

Position	(θ, ψ, ϕ)	Predicted Sun vector in body frame based on Figure 41.	${}^o\hat{S}$	${}^B\hat{S}$ based on (84)
I	$(\pi, 0, 0)$	[0;1;0]	[0;1;0]	[0;1;0]
II	$(\pi, -\pi/2, 0)$	[1;0;0]	[0;1;0]	[1;0;0]
III	$(\pi, \pi/2, \pi/2)$	[0;0;1]	[0;1;0]	[0;0;1]
IV	$(\pi, 0, -\pi/2)$	[0;0;-1]	[0;1;0]	[0;0;-1]

b. Definition Based on Trigonometry

An alternative method of deriving an equation for the Sun vector removes the need for an orbit frame; all that is required is the Sun vector, the angle between the y - z plane and the Sun-Vector, ψ , and the angle from the x - y plane to the Sun-Vector, ϕ , with both angles being positive in the counter-clockwise direction. The equation for the Sun-Vector can be derived through trigonometry based on Figure 42.. .

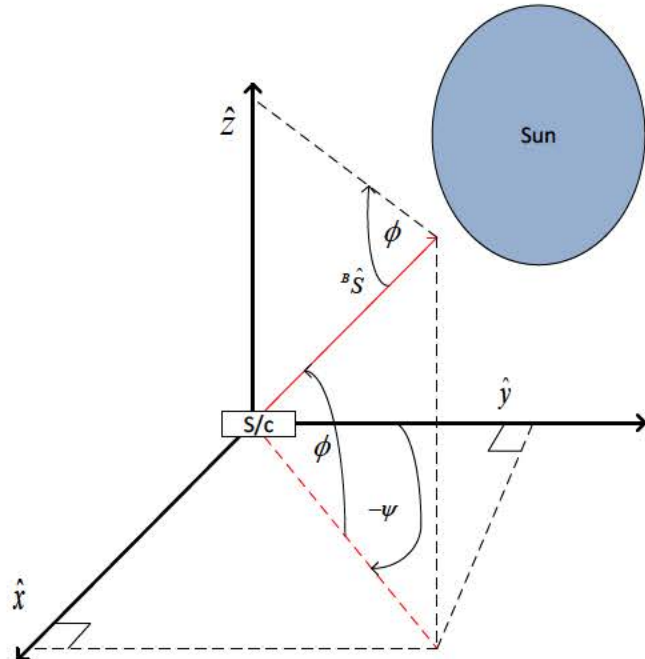


Figure 42. Trigonometric derivation of the Sun vector

The Sun vector in the body fixed frame:

$$\hat{S}(\psi, \phi) = \begin{bmatrix} \cos(\phi) \sin(-\psi) \\ \cos(\phi) \cos(-\psi) \\ \sin(\phi) \end{bmatrix} = \begin{bmatrix} -\cos(\phi) \sin(\psi) \\ \cos(\phi) \cos(\psi) \\ \sin(\phi) \end{bmatrix} \quad (85)$$

Equation (85) can be checked in two ways: first under the condition that $(\psi, \phi) = (0, 0)$ the expectation is that $\hat{S} = [0; 1; 0]$, shown in (86) and under the same test rotations as before shown in Figure 43., with the results in Table 5.

$$\hat{S}(0, 0) = \begin{bmatrix} -\cos(0) \sin(0) \\ \cos(0) \cos(0) \\ \sin(0) \end{bmatrix} = \begin{bmatrix} 0 \\ 1 \\ 0 \end{bmatrix} \quad (86)$$

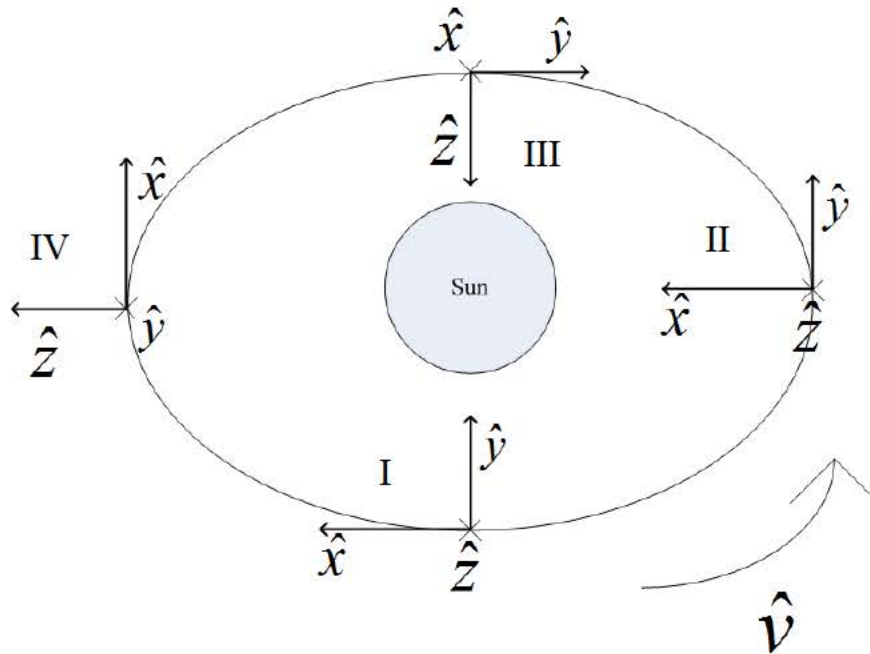


Figure 43. Different test orientations

Table 5. Analysis of the different orientations in Figure 3.4

Position	(ψ, ϕ)	Expected Sun vector in body frame based on Fig. IV.8	$\hat{\mathbf{S}}$ based on (85)
I	$(0, 0)$	$[0;1;0]$	$[0;1;0]$
II	$(-\pi/2, 0)$	$[1;0;0]$	$[1;0;0]$
III	$(\pi/2, \pi/2)$	$[0;0;1]$	$[0;0;1]$
IV	$(0, -\pi/2)$	$[0;0;-1]$	$[0;0;-1]$

Equation (86) and Table 5. confirm that this derivation will also produce correct results for defining the Sun-Vector with regards to the spacecraft body fixed frame.

c. Comparison between Sun-Vector Based on DCM and Trigonometry

It is clear that both (84) and (85) are the same equation and will produce the same results, however the Direction Cosine Matrix derivation provides for more flexibility; if desired it is possible to include the third rotation about the y -axis and use (83). However, due to the need to illuminate the solar panels the spacecraft should be limited in its rotation angles around the y -axis. Therefore, unless stated otherwise the Sun-Vector will be defined using (84), will be represented only by ψ and ϕ , and in the text will be displayed with this notation, (ψ, ϕ) .

5. Moment Arm

One more piece of information needed to calculate the radiation disturbance torque is the moment arm. This is defined as the difference between the vector that defines the center of pressure, c_p and the center of mass, c_m :

$$\vec{r} = \vec{c}_p - \vec{c}_m \quad (87)$$

6. Solar Torque

Evaluating (63) using (78) and (87) allows the solar torque disturbance to be computed for a flat plate as:

$$\vec{T} = (\bar{c}_p - \bar{c}_g) \times -PA(\hat{S} \cdot \hat{n}) \left[\rho_a \hat{S} + 2\rho_s (\hat{S} \cdot \hat{n}) \hat{n} + \rho_d \left(\frac{2}{3} \hat{n} + \hat{S} \right) \right] \quad (88)$$

D. SUMMARY

This chapter explained torque and space environmental disturbances experienced by a spacecraft. It provided a derivation of the solar torque equations including a definition of the Sun vector. The next chapter will develop a solar torque model for Kepler.

VI. KEPLER SOLAR RADIATION PRESSURE MODEL

The last chapter provided the background necessary to understand solar torque. This chapter explains the details of a model for Kepler based on a flat plate. To do this, Kepler's dimensions are first determined, followed by the development of a solar radiation pressure, SRP model. This chapter concludes with an analysis of the developed model through many different possible orientations of Kepler and compares it to other available solar torque data.

A. SIZING OF KEPLER

Before any model of Kepler can be developed, the dimensions of the spacecraft must be known. However, due to proprietary restrictions it was not possible to obtain a dimensional model of Kepler. Therefore, the relevant dimensions needed to be determined based on available information and drawings, such as Figure 44. .

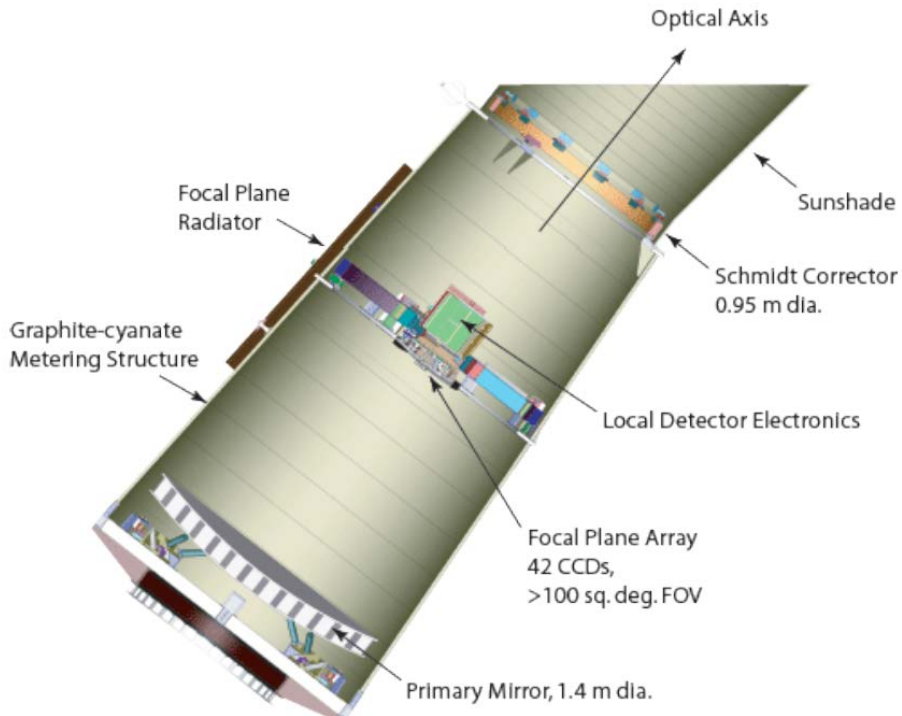


Figure 44. Cut-away of Kepler spacecraft, from [3]

From Figure 44., the primary mirror diameter is given as 1.4 m, and the flat Schmidt corrector has a diameter of 0.95 m. Figure 44. is assumed to be to scale so those given dimensions can be used to determine several other important dimensions. The basic method used was to take information, like Figure 44., import it into Microsoft Visio and obtain dimensions of other components that are not listed. Specifically, the Schmidt corrector was used as a reference because it is flat compared to the primary mirror. This image was imported to Microsoft Visio and a blue line was drawn from one end of the Schmidt corrector to the other. It measured 83.445 mm as shown in Figure 45..

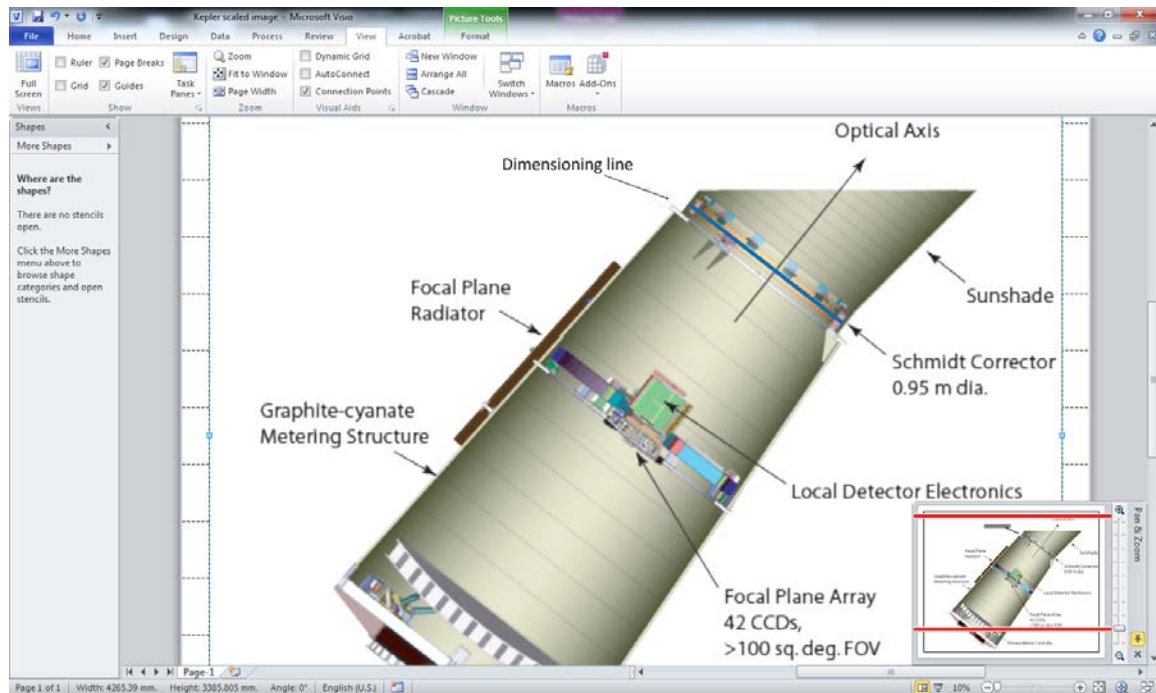


Figure 45. Image of Kepler figure in Microsoft Visio with dimensioning line, after [3]

The dimension of 83.45mm is obviously not the correct size of the Schmidt corrector. The image needs to be scaled, so that the line drawn across the Schmidt corrector is equal to 0.95m. This is accomplished by the simple calculation:

$$\text{scale factor} = \frac{\text{Actual length}}{\text{Microsoft Visio Length}} = \frac{950\text{mm}}{83.445\text{mm}} \approx 11.39 \quad (89)$$

Using the scale factor of 11.39, Figure 45. was altered so the dimensions of the image in Microsoft Visio are correct; this was accomplished by multiplying the height and the width of the image by the scale factor.

After scaling the image, a line was drawn along the Schmidt Corrector to confirm that the scaling was performed correctly and that the dimension of the Schmidt corrector in Microsoft Visio measures 0.950m. The scaled image allowed other dimensions not labeled in the original diagram to be determined. Figure 46. , displays the relevant dimensions obtained from the scaled view of Kepler.

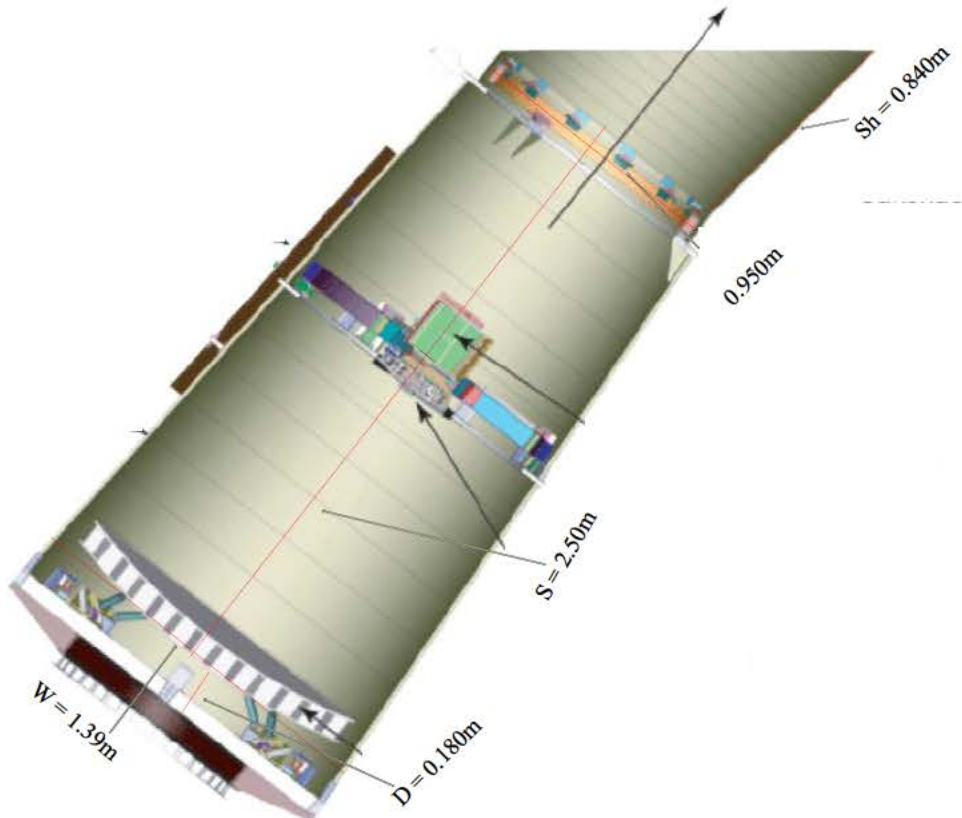


Figure 46. Dimensioned Kepler schematic, after [3]

There are other dimensions not obtainable from Figure 46. that are necessary for building a solar torque model, such as the height and length of the spacecraft portion and

the dimensions of the solar panels. These other measurements can be found by using the same technique as described but applied to other available drawings such as the one shown in Figure 47. .

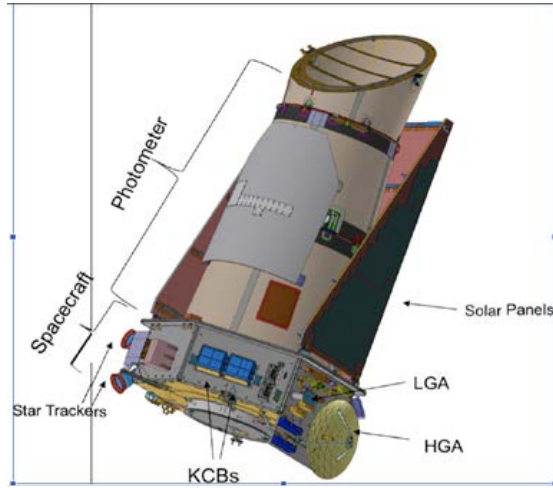


Figure 47. Kepler flight system, showing integrated photometer and spacecraft, from [3]

The reference feature for Figure 47. , instead of being the Schmidt corrector, is the sum of the lines labeled as *S* and *D*, in Figure 46. , which measure 2.68 m. This is because this dimension appears to be the feature that is most similar between the two images. Using the Microsoft Visio Length of 134.08 mm, which corresponds to the reference line drawn on Figure 47. , the known dimension of 2.68 m, and (89) the scaling factor for Figure 47. was calculated as 19.99.

Figure 48. is the final dimensioned model of the Kepler spacecraft using the view in Figure 47. and Table 6. lists the important dimensions and their descriptions from both Figure 46. and Figure 48.. The dimensions given in Table 6. are not exact dimensions; but are close approximations. This data is necessary for the next step of developing the SRP model of the spacecraft. In the next section a flat plate is considered to model the SRP.

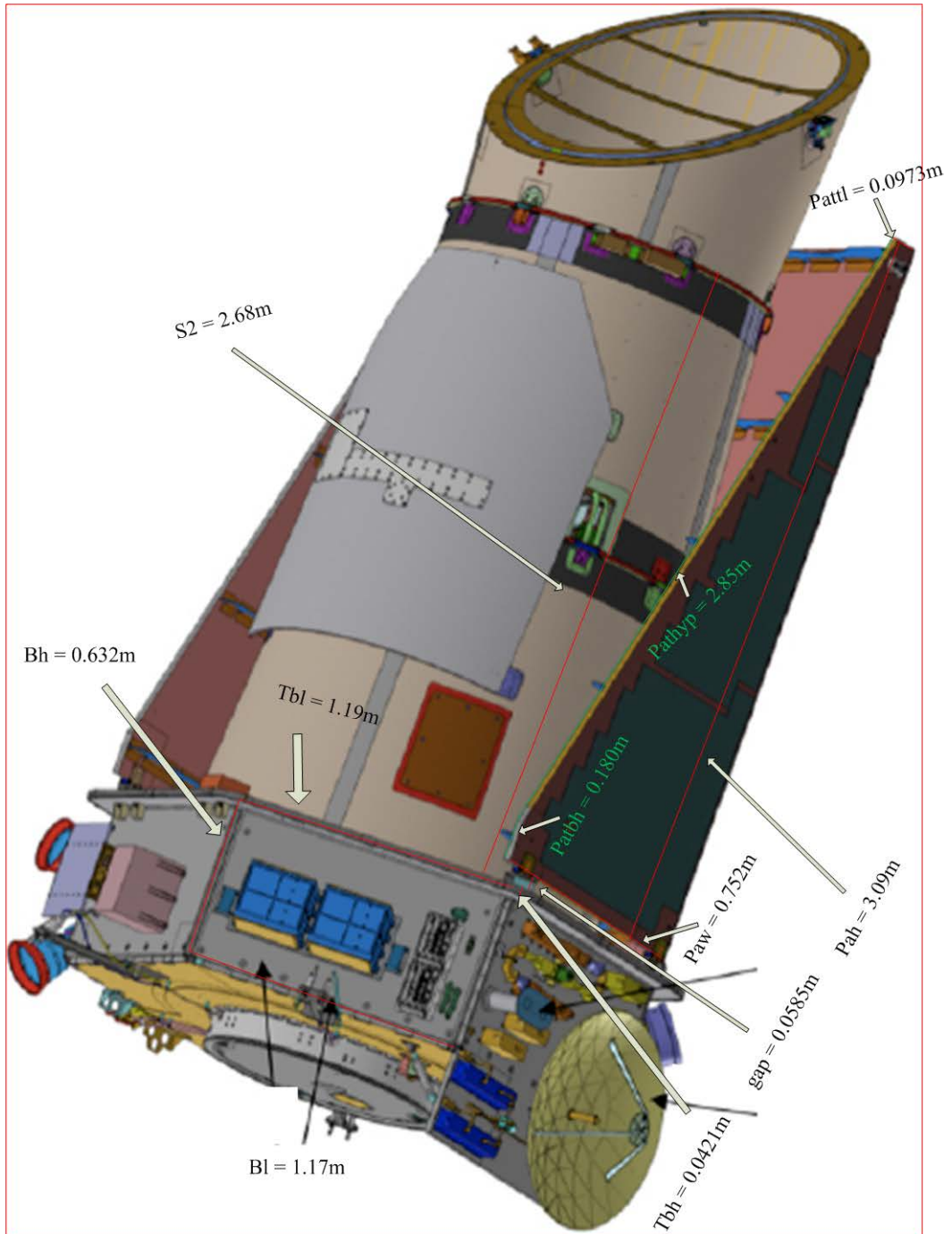


Figure 48. Second dimensioned Kepler schematic, after [3]

Table 6. Estimated Kepler dimensions

Name	Description	Dimension (m)	Source
S	Distance from one mirror to the other	2.50	Figure 46.
W	Width of the base of the photometer, diameter	1.39	Figure 46.
Sh	Height of Sun-shade	0.840	Figure 46.
D	Depth of photometer below primary mirror	0.180	Figure 46.
-	Schmidt Corrector	0.950	Figure 46.
S2	S+D	2.68	Figure 48.
B1	Bus Length	1.17	Figure 48.
Bh	Bus height	0.632	Figure 48.
Tbh	Top Bus height	0.0421	Figure 48.
Tbl	Top Bus length	1.19	Figure 48.
Gap	Gap between bus and solar panels	0.0585	Figure 48.
Pah	Solar Panel height	3.09	Figure 48.
Paw	Solar Panel Width	0.752	Figure 48.
Pathyp	Triangle Solar Panel hypotenuse	2.85	Figure 48.
Patbh	Triangle Solar Panel bottom height	0.180	Figure 48.
Pattl	Triangle Solar Panel top length	0.0973	Figure 48.

B. FLAT PLATE MODEL

Although, the Kepler spacecraft has many surfaces with different geometries, the desire is to model the spacecraft for solar torque purposes as simply as possible. The simplest model that is a viable possibility is a flat plate; it is simple analytically and computationally and it is viable because the majority of the time the two large solar panels are facing the Sun. This makes the parts of the spacecraft close to the positive y -axis face the major contributor of solar torque.

For a first iteration, it makes sense to make the single plate approximately as tall and wide as the spacecraft. Using the information from Table 6. the height of the flat plate is determined as:

$$h = Tbh + bh + S2 + Sh + Gap = 4.66 \text{ m} \quad (90)$$

Since the main concern is the solar torque on the positive y -axis spacecraft face, the width of the plate was chosen as twice the width of the solar panels, which is 1.50m.

The flat plate superimposed on a scaled drawing of Kepler is shown in Figure 49. ; the flat plate is the hashed rectangle outlined in red.

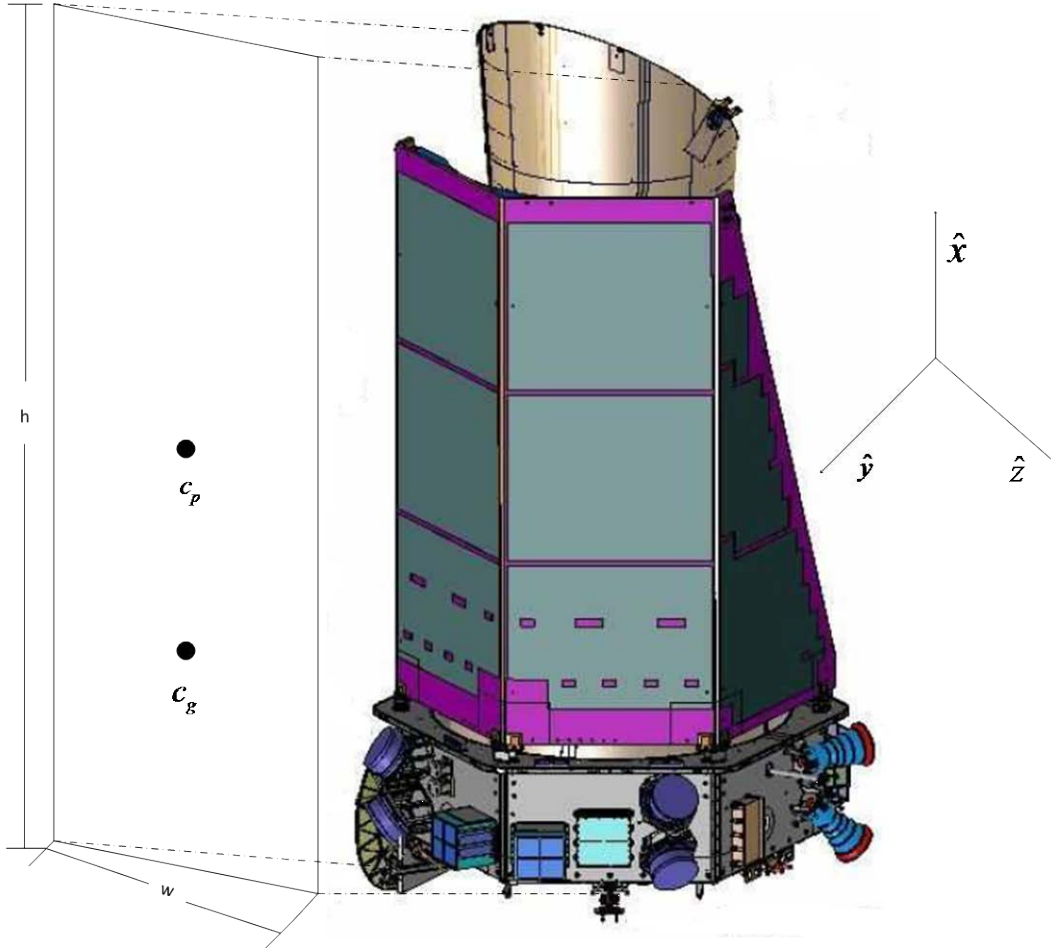


Figure 49. Schematic of flat plate, after [48]

As explained earlier, the distance from the c_p to the c_g is required to calculate the torque. It was assumed that Kepler's origin was fixed at the center of the bottom of the bus structure. The centroid of the flat panel, corresponding to the c_p , is in the middle of the panel. If the bottom of the panel lies on the y - z plane, at the $x=0$ position, the distance in the \hat{x} direction is half of the height, 2.33 m, of the panel. The distance in the \hat{z} direction is zero, since the flat plate rests vertically on the y - z plane, is parallel to the x - z plane and centered along the y -axis. The third coordinate, along the \hat{y} direction was chosen to align with the distance of the solar panels from the center of the spacecraft.

This distance was determined by using the geometry of a hexagon as shown in Figure 50. It was assumed that the solar panels are arranged in a regular hexagonal shape, minus two faces, with the one side as length P_{aw} , from Table 6.

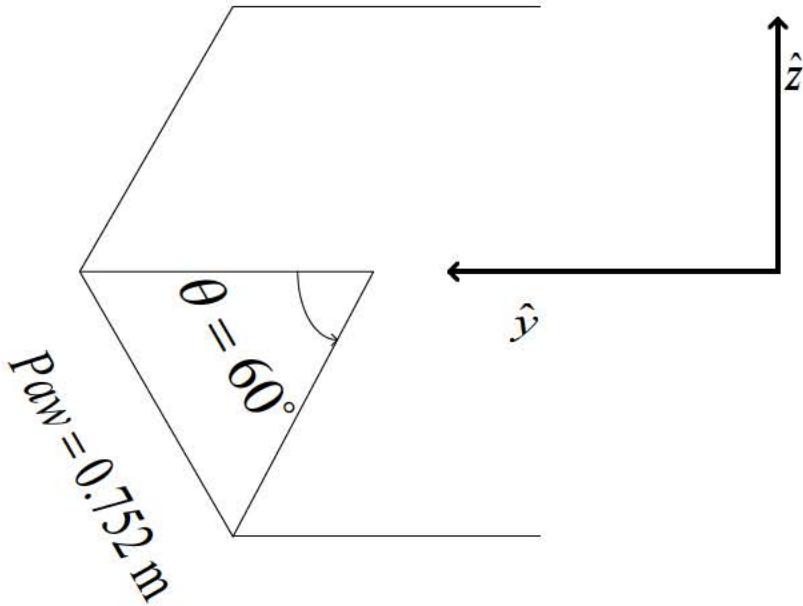


Figure 50. Hexagonal pattern of solar panels

Since the hexagon can be broken up into equilateral triangles the distance from the center to the edge of the solar panel was equal to its width which was 0.752 m. Therefore, the coordinates of the c_p of the flat plate are:

$$c_p = [x, y, z] = [2.33, 0.752, 0.0] \text{ m} \quad (91)$$

Two more important parameters have to be defined before conducting the analysis of the flat plate. These are the area and the coefficients of absorption, specular reflection and diffuse reflection of light for the solar panel.

It was assumed that the solar panel absorbs most of the solar radiation and it ignores diffuse reflection. As such the following values for the coefficients in (78) are used:

$$\begin{aligned} \rho_a &= 0.8 \\ \rho_s &= 0.2 \\ \rho_d &= 0.0 \end{aligned} \quad (92)$$

The normal vector to the surface of the flat panel is another crucial piece of information. As mentioned earlier the panel is parallel to the x - z plane giving it the following normal vector:

$$\hat{n} = [0, 1, 0] \quad (93)$$

The parameters for the flat plate SRP model are summarized in Table 7.

Table 7. Parameters for the flat plate SRP model

h_{panel} (m)	w_{panel} (m)	c_p (m)	\hat{n}	A (m^2)	ρ_α	ρ_s	ρ_d
4.66	1.50	[2.33, 0.752, 0.0]	[0, 1, 0]	6.99	0.8	0.2	0.0

C. RESULTS FROM FLAT PLATE SRP MODEL

The following figures display the results of the solar torque on the flat panel in different orientations defined in terms of azimuth and elevation angles. In addition, contour plots from a model developed by Ball Aerospace [13] are provided for comparison.

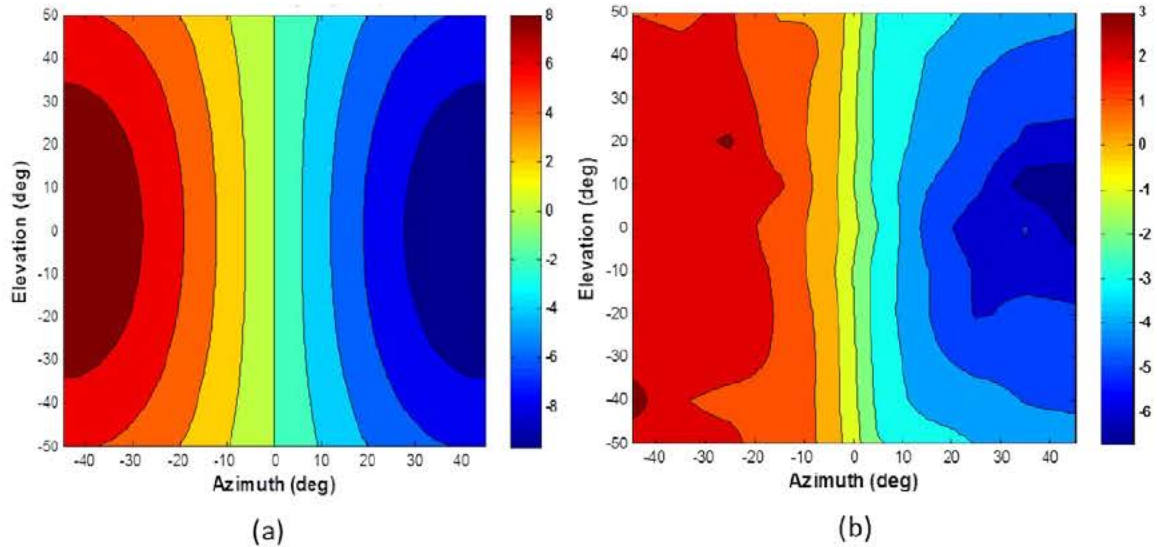


Figure 51. Solar torque ($\mu\text{N}\cdot\text{m}$) around the x -axis (a) flat plate model with $c_p = [2.10, 0.752, 0.0]$ m, (b) Ball model, after [13]

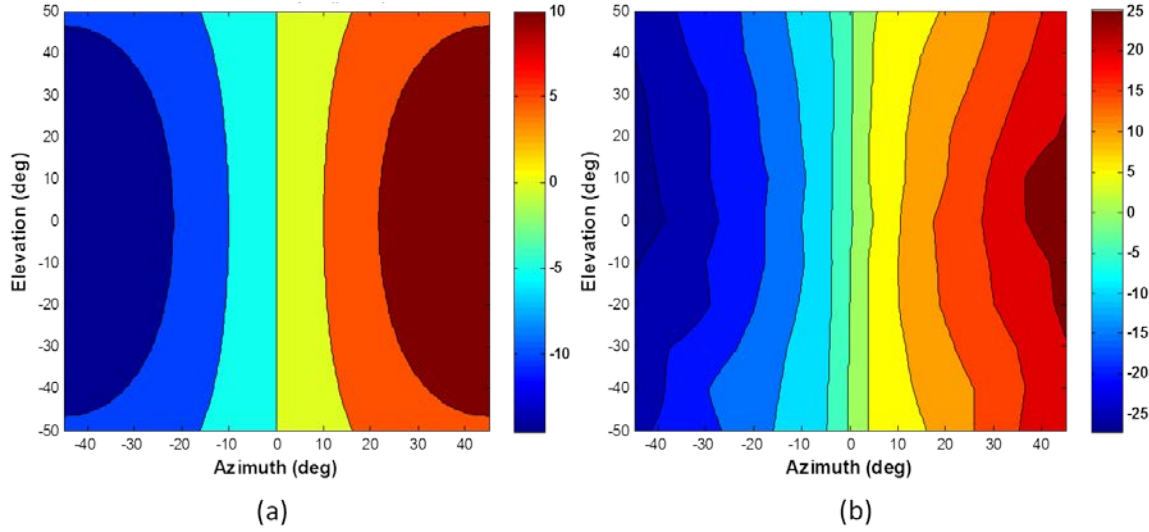


Figure 52. Solar torque ($\mu\text{N}\cdot\text{m}$) around the y -axis (a) flat plate model with $c_p=[2.10, 0.752, 0.0] \text{ m}$, (b) Ball model, after [13]

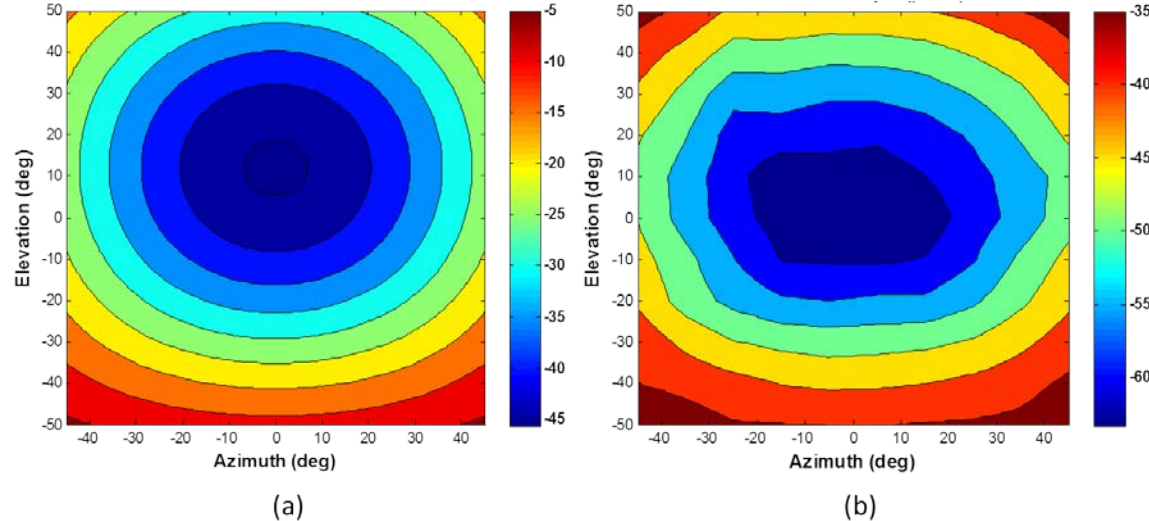


Figure 53. Solar torque ($\mu\text{N}\cdot\text{m}$) around the z -axis (a) flat plate model with $c_p=[2.10, 0.752, 0.0]$ m, (b) Ball model, after [13]

The results shown in Figure 51. and Figure 52. for the flat plate model are similar to the Ball model. There are deviations in the magnitude and the flat plate model has smoother contours, due to the simplicity of the model. However, in Figure 53. , the flat plate model has the maximum solar torque centered approximately on a rotation of (0, 15), whereas the Ball model is centered at (0, 3). If the equations for torque are

examined it can be shown that the deviations observed using the flat plate is expected. Further investigation is necessary to understand why the flat plate model around the z -axis deviates from the model developed by Ball Aerospace.

The cross-product for torque can be expanded to obtain:

$$\vec{T} = (r_y F_z - r_z F_y) \hat{i} - (r_x F_z - r_z F_x) \hat{j} + (r_x F_y - r_y F_x) \hat{k} \quad (94)$$

Utilizing the assumed vector, $\vec{r} = [r_x, r_y, r_z]^T = [r_x, r_y, 0]^T$, (94) simplifies as:

$$\vec{T} = (r_y F_z) \hat{i} - (r_x F_z) \hat{j} + (r_x F_y - r_y F_x) \hat{k} \quad (95)$$

For the flat plate SRP model the r -vector components are all positive. Therefore, by choosing different combinations of F_x and F_y , (the only two components of force relevant to the solar torque component around the z -axis), the deviation of the maximum solar torque can be predicted. For example, if $|F_x| < |F_y|$ but both forces point in opposite directions then the two components will complement each other. Initially, from examining (84) one may conclude that this combination of the forces should not make a difference on the maximum torque and that it should be when both rotations angles are zero. However, as demonstrated in Table 8. that assumption is not true. It turns out that if $elevation > 0$ and $azimuth = 0$, then direction of the two forces are opposite and $|F_x| < |F_y|$, causing the magnitude of the solar torque around the z -axis to be greater than if $elevation = azimuth = 0$. Furthermore, when $elevation < 0$ and $azimuth = 0$, the directions of the forces are the same so even though $|F_x| < |F_y|$ the magnitude of the solar torque around the z -axis is less than when $elevation = azimuth = 0$. The fact that the maximum solar torque is not centered on (0,0) in Figure 53. is therefore consistent with the simplification inherent to the developed model.

Table 8. Test cases to validate results in Figure 53.

Az($^{\circ}$)	El($^{\circ}$)	${}^B\hat{S}$	F_x (μN)	F_y (μN)	F_z (μN)	T_x ($\mu N\cdot m$)	T_y ($\mu N\cdot m$)	T_z ($\mu N\cdot m$)
0	0	[0,1,0]	0	-35	0	0	0	-31
-45	0	[0,0.70,-0.70]	0	-17	12	8.7	-10	-16
45	0	[0,0.70,0.70]	0	-17	-12	-8.7	10	-16
0	-10	[0.17,0.98,0]	-4.0	-34	0	0	0	-27
0	10	[-0.17,0.98,0]	4.0	-34	0	0	0	-33

If this deviation is predicted, then the question remains why the flat plate model produces this deviation that is not present in the Ball model. One possible explanation is that the flat plate model has a greater value in the \hat{y} component of the c_p than the Ball model. If, however the component in the \hat{y} direction is small enough then the deviation is negligible. Alternatively the deviation can be the result of complexity not captured using the flat plate model.

D. MATCHING THE DATA

As seen in Figure 51., Figure 52. and Figure 53., the data produced by the simple flat plate model has similar qualitative characteristics to the model developed by Ball Aerospace. However, the magnitude of the solar torques is different and the center point for the maximum solar torque around the z -axis is not the same. Therefore, it is useful to attempt to better match the Ball model.

Several steps were taken to more closely match the single plate model to the Ball data. First, it was necessary to obtain data points from the Ball Aerospace contour plots (Figure 51. through Figure 53.). A total of 9191 data points were obtained by digitizing the plots. This corresponds to 101 degrees range for elevation, and 91 degrees range for azimuth. The second, but more important step was to carry out a least squares optimization to minimize the difference between the two data sets. This was conducted using the built-in MATLAB function “lsqnonlin.” The function “lsqnonlin” solves is [54]:

$$\min_x \|f(x)\|_2^2 = \min_x (f_1(x)^2 + f_2(x)^2 + \dots + f_n(x)^2) \quad (96)$$

This function is recommended when trying to solve a problem with no constraints, but with the objective of a least squares analysis [55]. The built-in MATLAB function converts the problem into a least squares problem, therefore it is only necessary to input [54]:

$$f(x) = \begin{bmatrix} f_1(x) \\ f_2(x) \\ \vdots \\ f_n(x) \end{bmatrix} \quad (97)$$

Equation (98) is the function provided to lsqnonlin for the least squares fit. In this case it was decided to keep the center of pressure fixed, while making the c_g as the unknown. The goal of this analysis is to minimize the overall error between the three plots. This can be accomplished by minimizing the following equation:

$$\begin{aligned} f(c_g(1), c_g(2), c_g(3)) = & \|T_{x,B} - ((c_p(2) - c_g(2)) * F_z - (c_p(3) - c_g(3)) * F_y\|_2 \dots \\ & + \|T_{y,B} - (-((c_p(3) - c_g(3)) * F_x - (c_p(1) - c_g(1)) * F_z)\|_2 \dots \\ & + \|T_{z,B} - ((c_p(1) - c_g(1)) * F_y - (c_p(2) - c_g(2)) * F_x\|_2 \end{aligned} \quad (98)$$

where $T_{i,B}$ denotes data obtained from Ball contour plots.

The results of this least squares analysis provided a new c_g . However, because the c_g represents the actual physical body of Kepler whereas the flat plate is a simplified model it is more useful to apply the adjustment to the c_p . Although with only one flat plate there is not much difference in solving for a new c_p or a new c_g if it is decided to use more plates in the hopes of gaining greater fidelity in the model it is simpler to solve for a new c_g and applying the adjustment to the c_p of the plates rather than solve for multiple new c_p 's. After applying the adjustment of the c_g , the new c_p becomes:

$$c_{p,new} = [x, y, z] = [3.11, 0.368, -0.0379] \approx [3.11, 0.368, 0] \quad (99)$$

The results from this analysis imply that the flat plate should be moved up in the \hat{x} direction, inward in the negative \hat{y} direction to better match the Ball data.

If the single plate model is reconfigured with this new c_p , the predicted SRP torque data more closely matches the data provided by Ball (see Figure 54. , Figure 55. and Figure 56.).

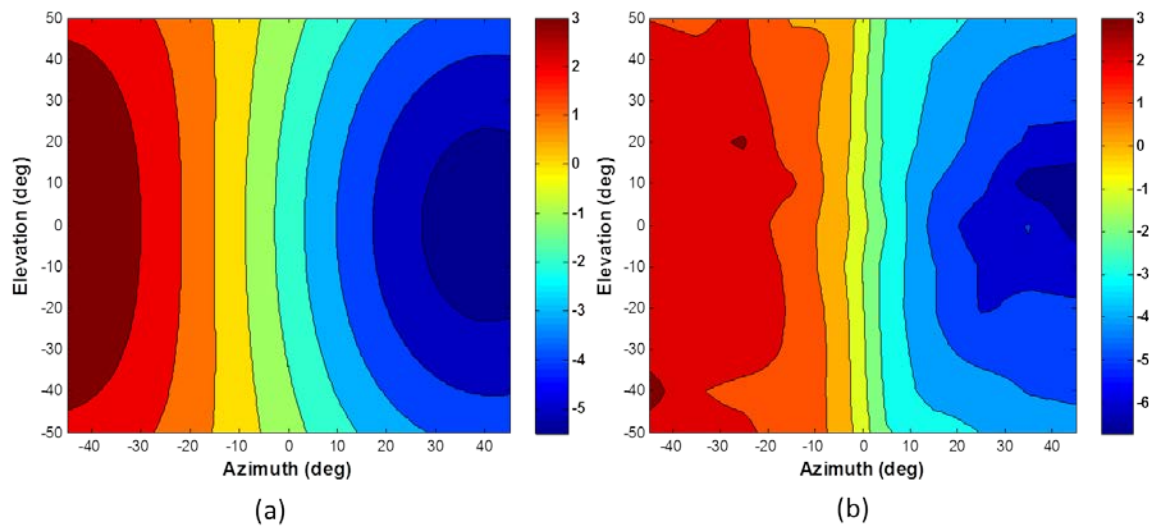


Figure 54. Solar torque ($\mu\text{N}\cdot\text{m}$) around the x -axis (a) flat plate model with $c_p=[3.11, 0.368, -0.0379]$ m, (b) Ball model, after [13]

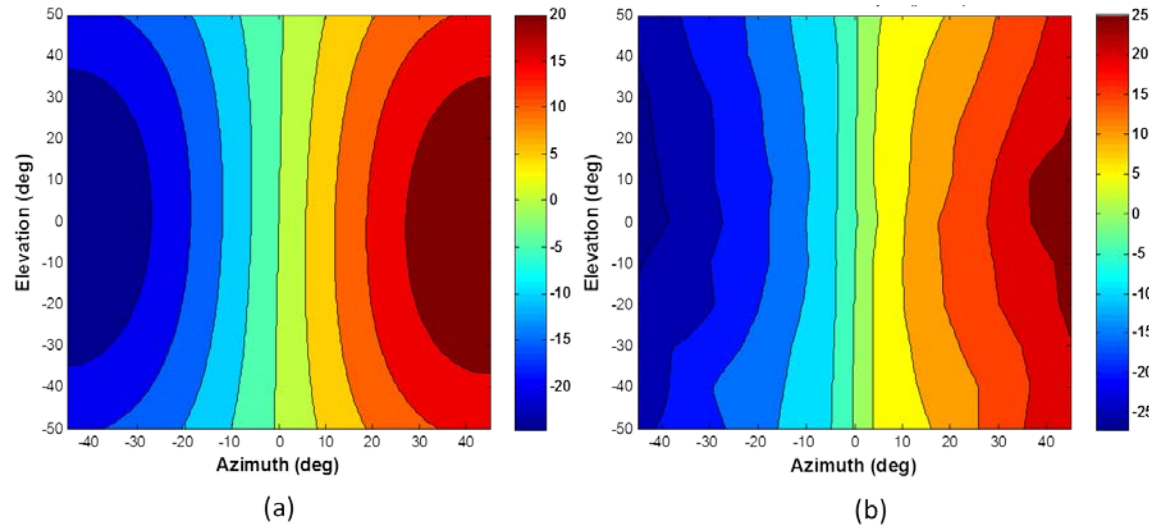


Figure 55. Solar torque ($\mu\text{N}\cdot\text{m}$) around the y-axis (a) flat plate model with $c_p=[3.11, 0.368, -0.0379]$ m, (b) Ball model, after [13]

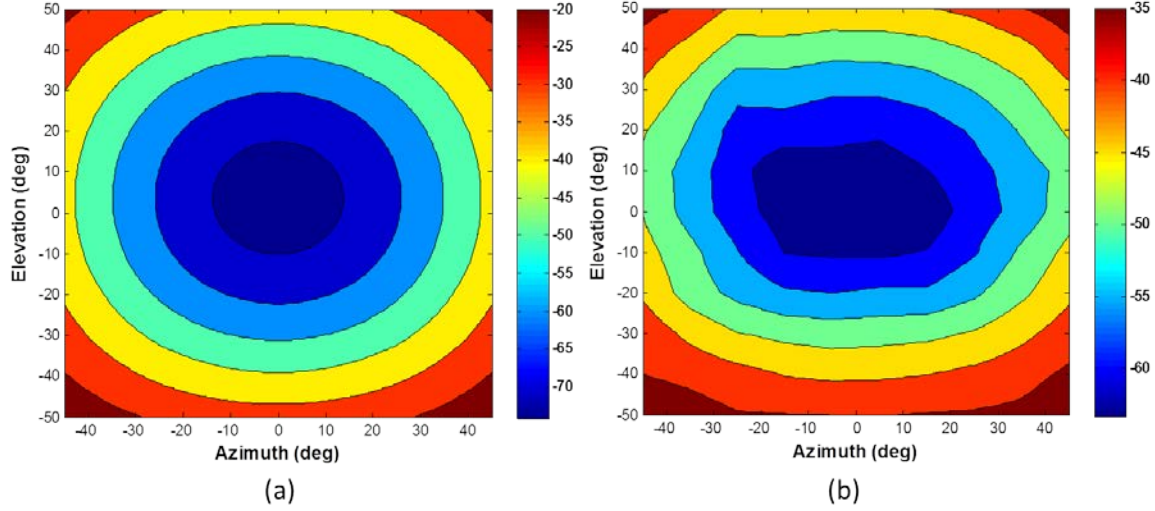


Figure 56. Solar torque ($\mu\text{N}\cdot\text{m}$) around the z -axis (a) flat plate model with $c_p=[3.11, 0.368, -0.0379]$ m, (b) Ball model, after [13]

The predicted torque magnitudes are much closer using the shifted c_p , while the overall shape of the contours is similar. The improvement of the optimized model is better displayed via a comparison of the errors at different rotations. Because some values are very close to zero it was chosen to compare the flat plate models to the data points from the Ball model using the per axis absolute error, e.g.:

$$\text{error}_i = |T_i - T_{i,B}| \quad (100)$$

The absolute errors for each solar torque component are shown in Figure 57. , Figure 58. and Figure 59. .

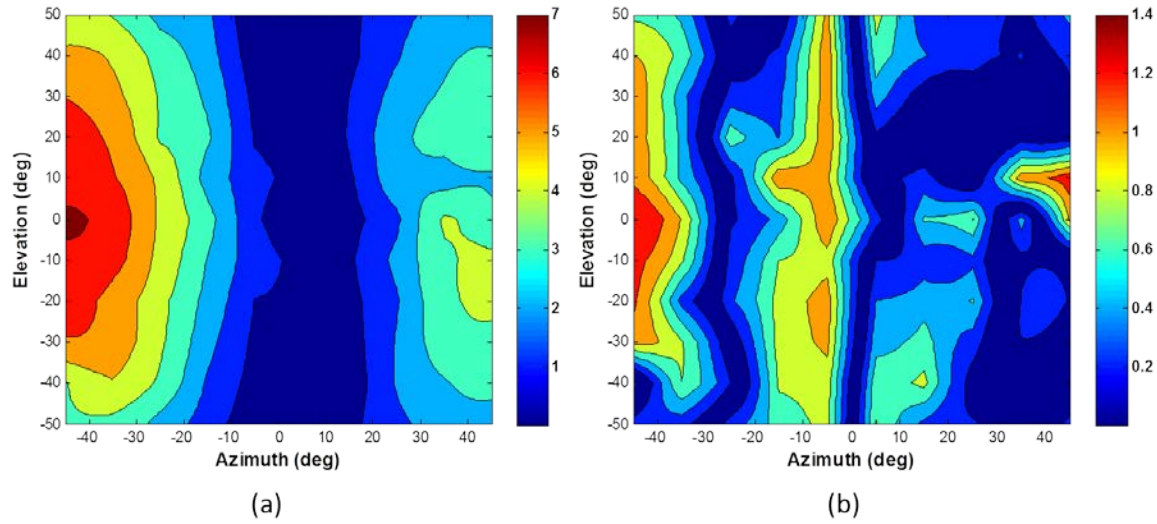


Figure 57. Absolute error ($\mu\text{N}\cdot\text{m}$) of solar torque around the x -axis (a) flat plate model with $c_p=[2.33, 0.752, 0.0]$ m (b) flat plate model with $c_p=[3.11, 0.368, -0.0379]$ m

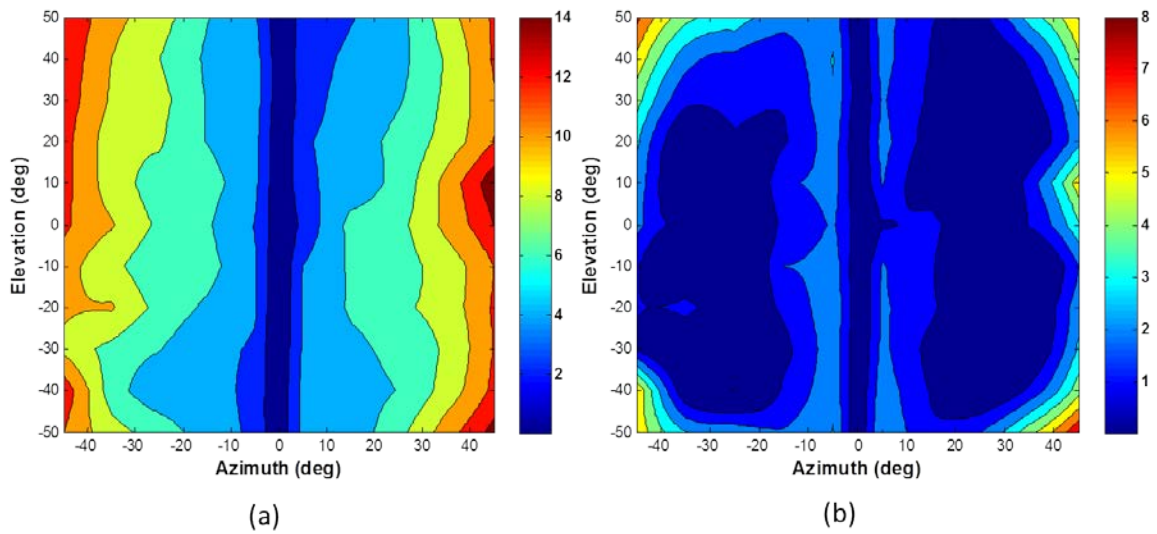


Figure 58. Absolute error ($\mu\text{N}\cdot\text{m}$) of solar torque around the y-axis (a) flat plate model with $c_p=[2.33, 0.752, 0.0]$ m (b) flat plate model with $c_p=[3.11, 0.368, -0.0379]$ m

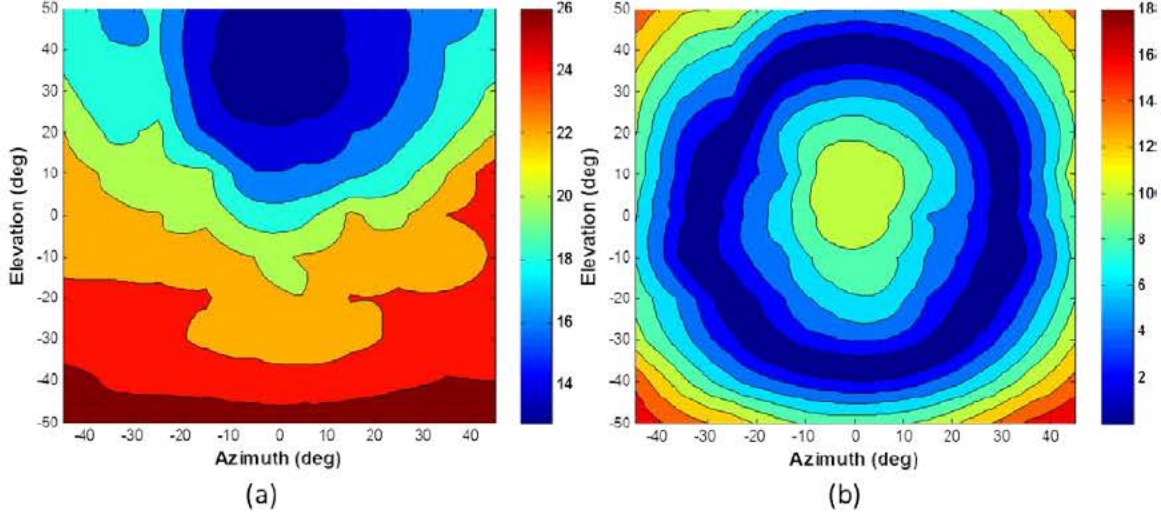


Figure 59. Absolute error ($\mu\text{N}\cdot\text{m}$) of solar torque around the z -axis (a) flat plate model with $c_p=[2.33, 0.752, 0.0]$ m (b) flat plate model with $c_p=[3.11, 0.368, -0.0379]$ m

Table 9. summarizes the maximum and minimum errors of the two models and it lists the least squares error similar to what was minimized in (98).

$$LSE = \left\| \left\| T_{B,x} - T_x \right\|_2 + \left\| T_{B,y} - T_y \right\|_2 + \left\| T_{B,z} - T_z \right\|_2 \right\|_2 \quad (101)$$

Table 9. highlights the fact that there is an improvement in predicting the torque when the center of pressure is adjusted. The absolute errors using the shifted flat plate model are now 25% of the original values.

Table 9. Summary of comparison of flat plate models

Flat Plate c_p (m)	error_x (max,min) ($\mu\text{N}\cdot\text{m}$)	error_y (max,min) ($\mu\text{N}\cdot\text{m}$)	error_z (max,min) ($\mu\text{N}\cdot\text{m}$)	LSE ($\mu\text{N}\cdot\text{m}$)
[2.33, 0.752, 0.0]	$(7.0, 1.2 \times 10^{-4})$	$(15, 8.3 \times 10^{-4})$	$(28, 13)$	3065
[3.11, 0.368, -0.0379]	$(1.4, 1.3 \times 10^{-5})$	$(8.0, 7.5 \times 10^{-5})$	$(18, 5.2 \times 10^{-3})$	727

Although there was an overall improvement using the shifted center of pressure, the torque around the x -axis became skewed to the left. Recall that originally, the torque around the z -axis was skewed. Nonetheless, the single plate model, particularly with the c_p shift provides a reasonable estimate of the solar radiation pressure torque and so this model will be used in the sequel.

E. SUMMARY

This chapter covered the work completed to determine the dimensions of Kepler and how those dimensions were used to create a flat plate solar torque model of Kepler. The flat plate model was then used to develop a prediction of SRP torque on Kepler. Finally, the predicted values were validated against the information provided from an available Ball model, which allowed parameters of the flat plate model to be optimized. It was determined that the flat plate model provides reasonable results and will be utilized in the next chapter, to explore the ability of the degraded reaction wheel system to maintain pointing in the presence of SRP torque.

VII. POINTING CAPABILITY USING TWO WHEELS

Kepler was designed with four reaction wheels, however it currently has only two fully functioning wheels [56]. This poses a problem because conventional control algorithms, like PD controllers, can only command attitude movements of the spacecraft in the plane of the reaction wheels. Two wheels alone cannot provide three-axis control. This degradation and the fact that Kepler has a high pointing accuracy requirement forces one to analyze the impact of the solar torques to determine how long Kepler can point in a desired direction. This chapter will analyze the drift characteristics of Kepler with two reaction wheels using the flat plate SRP model, developed in the last chapter.

A. SOLAR TORQUE RELATIVE IN THE REACTION WHEEL PLANE

As mentioned in the introduction two out of the four original reaction wheels have failed. A schematic of the position of the reaction wheels on Kepler is shown in Figure 60. with the two failed wheels, two and four, marked by a cross.

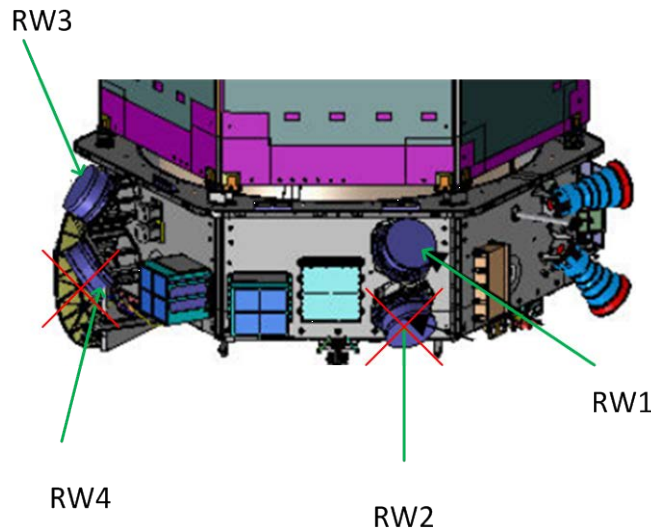


Figure 60. Schematic of reaction Kepler reaction wheels, after [13]

Calculating the component of solar torque in the plane and out of the plane of the reaction wheels will provide a quantifiable measure of how long Kepler can maintain its

pointing accuracy. If the solar torque is perpendicular to the normal vector to the reaction wheel plane then the solar torque vector lies in the RW-plane and can be rejected. Otherwise, the spacecraft will drift in the uncontrolled direction. The normal to the RW-plane is given by:

$$\hat{n}_{wheels} = \frac{\hat{r}_{w1} \times \hat{r}_{w3}}{\|\hat{r}_{w1} \times \hat{r}_{w3}\|} \quad (102)$$

where \hat{n}_{wheels} is the normal vector to RW-plane and r_{wi} is the unit describing the orientation of the reaction wheel for $i=1,3$.

In order to test if the solar torque vector is in the reaction wheel plane the dot product between the normal vector and solar torque is needed:

$$\cos(\theta) = \hat{n}_{wheels} \cdot {}^B\hat{T}_s \quad (103)$$

If $\cos(\theta)=0$ then the solar torque vector is perpendicular to the normal vector, meaning that the solar torque vector is completely in the RW-plane.

Figure 61. shows, a schematic of the plane made by the two reaction wheel vectors, the normal vector to the plane, the solar torque vector, and the angle between the normal and solar torque vector described in (103).

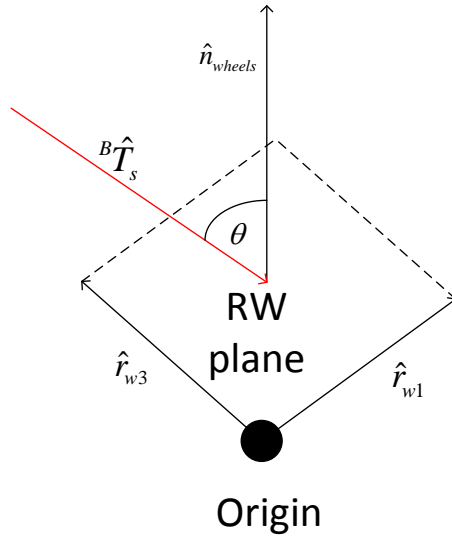


Figure 61. Schematic of reaction wheel plane

The reaction wheel vectors used in (102) are listed in Table 10. with the failed reaction wheels highlighted in red and the functioning wheels in green.

Table 10. Kepler RW vectors, after [13]

	RW 1	RW 2	RW 3	RW 4
X	0.574	-0.574	0.574	-0.574
Y	0.485	0.485	0.485	0.485
Z	0.660	0.660	-0.660	-0.660

The dot product of (103) solved for the same ranges for azimuth and elevation angles as the solar torque model are shown in Figure 62. .

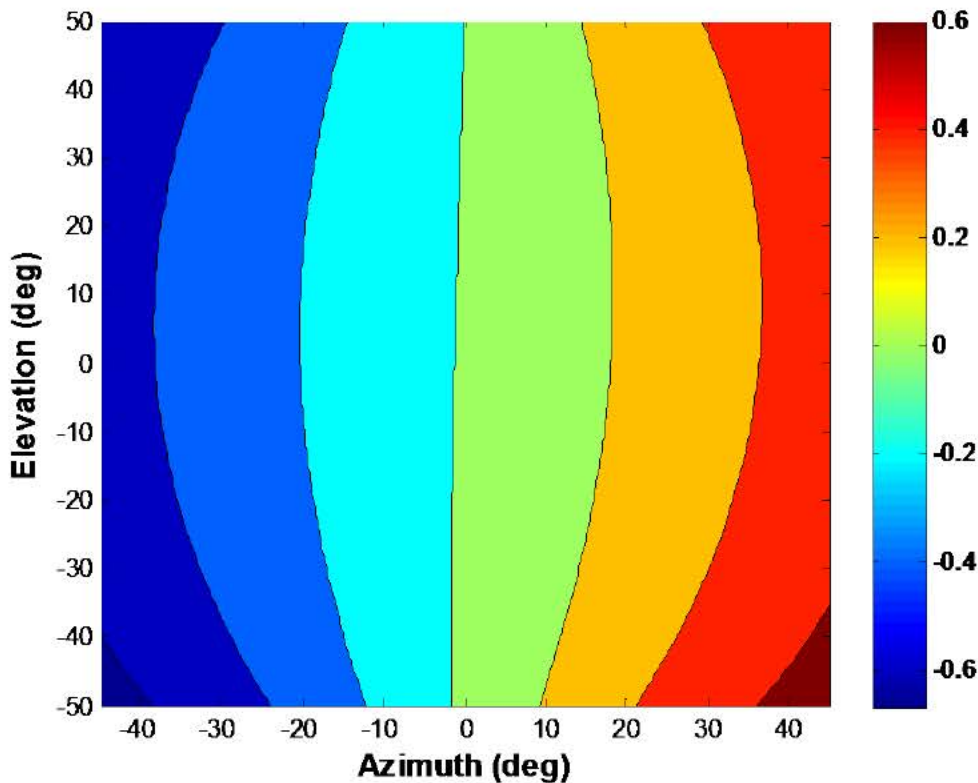


Figure 62. Cosine of the angle between RW plane normal and the solar torque vector

Figure 62. shows that there are many orientations where the RW plane normal and the solar torque vector are perpendicular or at least near perpendicular. This implies that there are many orientations of the spacecraft where the remaining reaction wheels may be able to maintain the necessary pointing accuracy. However, further analysis is required, since the values are not exactly zero.

Besides the simple calculation above, it is beneficial to determine the actual amount of solar torque that is in-plane and out of plane of the reaction wheels. This will help quantify how much torque can be compensated by the reaction wheels and how long before the out of plane disturbance torque creates a pointing drift greater than the tolerance required for science operations. Figure 63. depicts the components of solar torque that can be considered in-plane and out-of-plane, with \hat{t} corresponding to the vector parallel to the RW-plane.

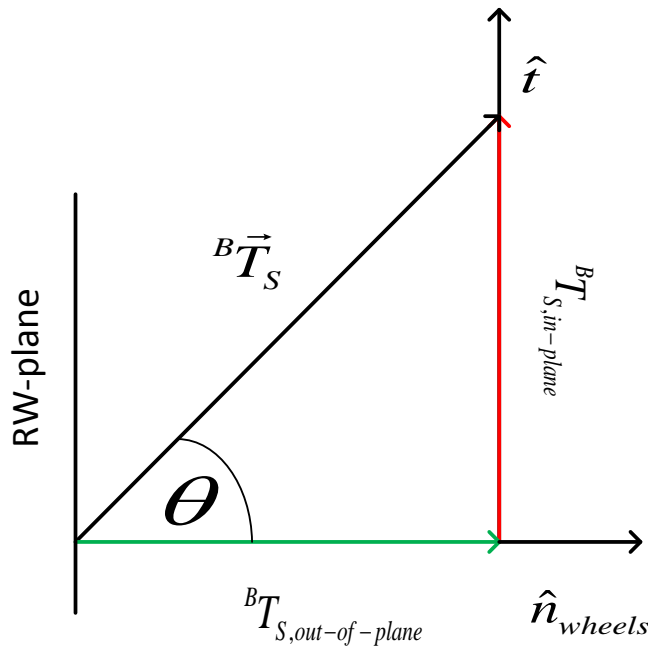


Figure 63. Projections of solar torque onto unit vector normal to reaction wheel plane

The vector projection may be used to calculate the out of plane torque.

$${}^B \vec{T}_{S,out-of-plane} = {}^B T_S \hat{n}_{wheels} = ({}^B \vec{T}_S \cdot \hat{n}_{wheels}) \hat{n}_{wheels} \quad (104)$$

Equation (105) gives the amount of torque expressed in the body-frame that is perpendicular to the normal vector to the reaction wheel plane, in other words the solar torque in the plane of the reaction wheels.

$${}^B\vec{T}_{S,in-plane} = {}^B\vec{T}_S \hat{t} = {}^B\vec{T}_S - {}^B\vec{T}_S \hat{n}_{wheels}, \hat{t} \quad (105)$$

After calculating the vectors for the in-plane and out of plane torque, it is useful to plot the magnitudes of the two torque components based on different orientations of the plate; this provides a visualization to determine if there are any orientations that give acceptable pointing accuracy requirements. This analysis assumes that only one side of the plate will provide solar torque so the angle between the solar torque and the normal vector to the reaction wheels is limited as in (106). The results of this analysis are shown in Figure 64. and Figure 65. .

$$\begin{aligned} {}^B\vec{T}_{S,out-of-plane} &= \left| {}^B\vec{T}_S \hat{n} \right|, 0 \leq \theta < \frac{\pi}{2} \\ {}^B\vec{T}_{S,out-of-plane} &= -\left| {}^B\vec{T}_S \hat{n} \right|, \frac{\pi}{2} \leq \theta \leq \pi \\ {}^B\vec{T}_{S,in-plane} &= \left| {}^B\vec{T}_S \hat{t} \right|, 0 \leq \theta \leq \pi \end{aligned} \quad (106)$$

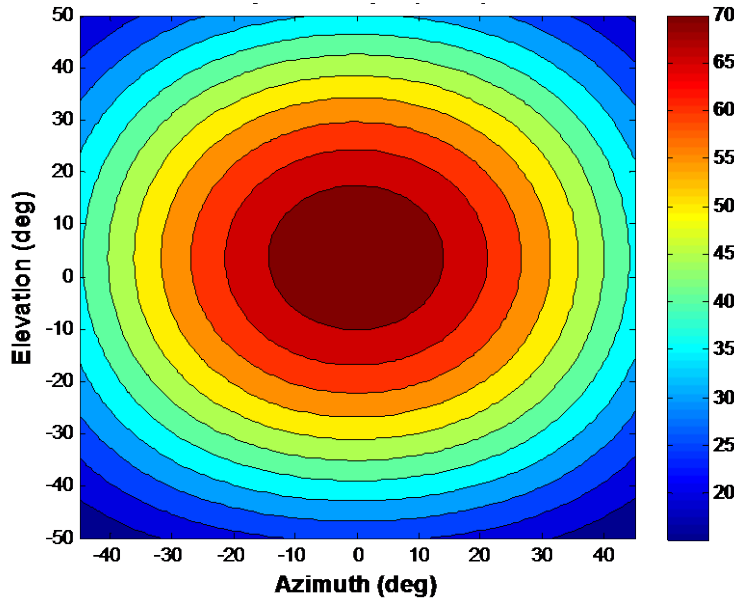


Figure 64. In-plane solar torque ($\mu\text{N}\cdot\text{m}$)

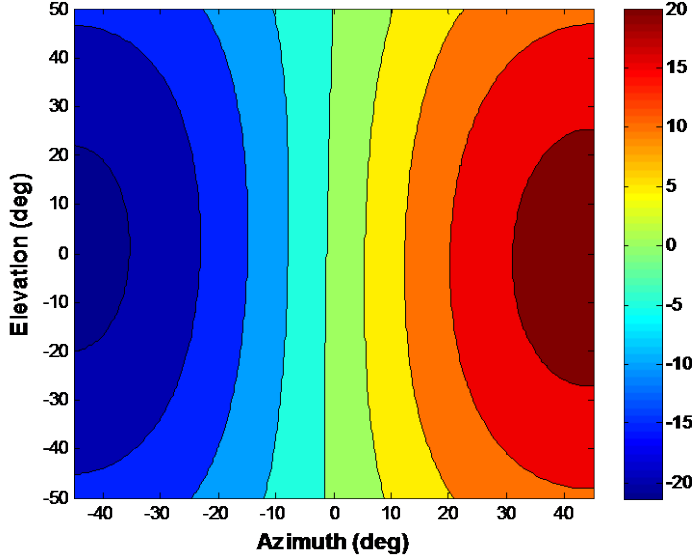


Figure 65. Out of plane solar torque ($\mu\text{N}\cdot\text{m}$)

As expected the results displayed in Figure 64. and Figure 65. provides a similar conclusion to Figure 63. , that there are many orientations such that the out-of-plane-torque is minimized. These orientations allow for a wide range of elevation angles, but are minimized around an azimuth of zero degrees. This explains the ecliptic orientation of the K2 mission, which results in an azimuth of approximately zero degrees.

Using the data above it is possible to determine how long it will take the spacecraft to rotate more than the required pointing stability. For this part of the analysis it is assumed that the reaction wheels can control the in-plane torque for a significantly longer period than a LC to any desired precision. This assumption is valid since the out-of-plane torque will cause the spacecraft to move outside of the tolerances before the momentum capacity of the reaction wheels is exhausted.

Predicting the spacecraft drift is a simple application of rotational dynamics. Equation (107) provides the relationship between angular momentum and torque projected on the principal body frame, where H is angular momentum and T is torque.

$$\dot{\vec{H}}_c + \vec{\omega} \times \vec{H}_c = \vec{T} \quad (107)$$

For this analysis two further assumptions were made: one the spacecraft has an initial rotation of zero ($\vec{\omega} \times \vec{H}_c = 0$) and the inertia matrix, \mathbf{J} , is constant. The analysis is

expected to provide conservative values, because the first assumption ignores the fact that while the spacecraft drifts it is obtaining an angular rate, which would affect the subsequent angular rates. The second assumption is a reasonable assumption, since in this analysis there is no concern about mass being lost due to thruster use. This allows (107) to be simplified into:

$$\dot{\vec{H}}_c = \mathbf{J} \dot{\vec{\omega}} = \vec{T} \quad (108)$$

This allows for the rate change in angular velocity to be calculated by:

$$\dot{\vec{\omega}} = \mathbf{J}^{-1} \vec{T} \quad (109)$$

This problem then becomes a simple double integrator; the rate of change in angular velocity can be integrated twice to derive an equation for an angle at time, t :

$$\begin{aligned} \vec{\omega}(t) &= \dot{\vec{\omega}} t + \vec{\omega}(0) \\ \vec{\theta}(t) &= \frac{1}{2} \dot{\vec{\omega}} t^2 + \vec{\omega}(0)t + \vec{\theta}(0) \end{aligned} \quad (110)$$

where $\vec{\omega}(0) = \vec{\theta}(0) = 0$

Using the assumption stated on the initial conditions of Kepler it is simple to solve for the time it takes for the spacecraft to rotate through an angle of $\theta_{\max}(t) = 0.009$ arcsec around any axis using:

$$t_i = \sqrt{\frac{2\theta_{\max}}{\dot{\phi}_i}} \quad (111)$$

where i=x,y,z

The results for the x -axis and y -axis are shown in Figure 66. and Figure 67. .

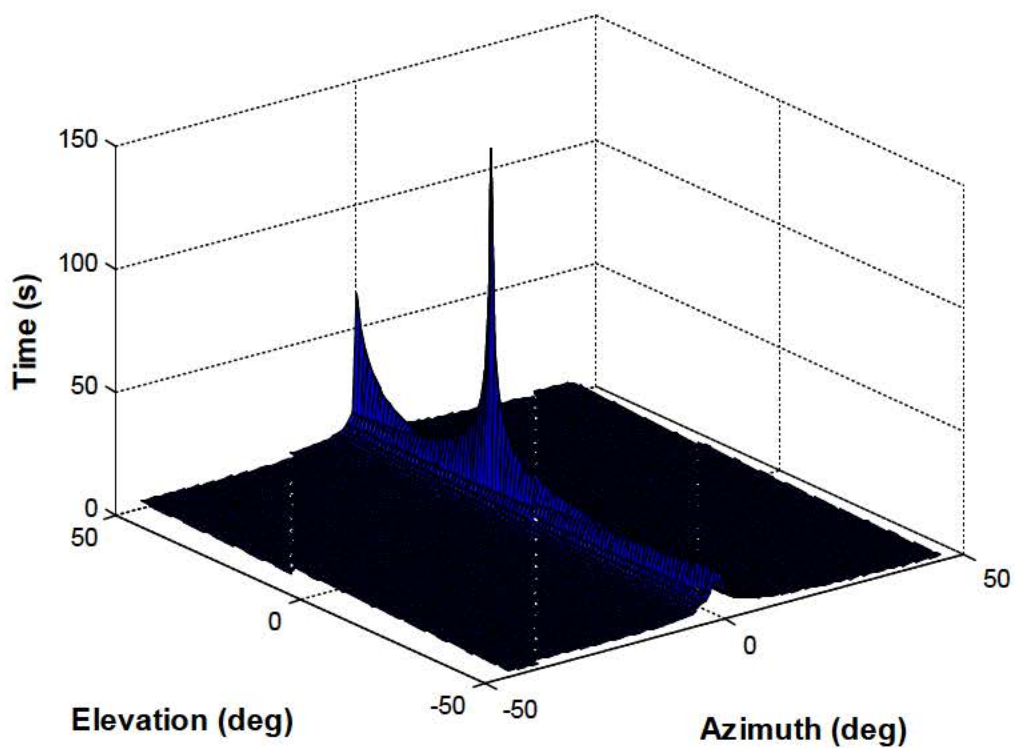


Figure 66. Time it takes to rotate around the x -axis by 0.009 arcsec for flat plate model

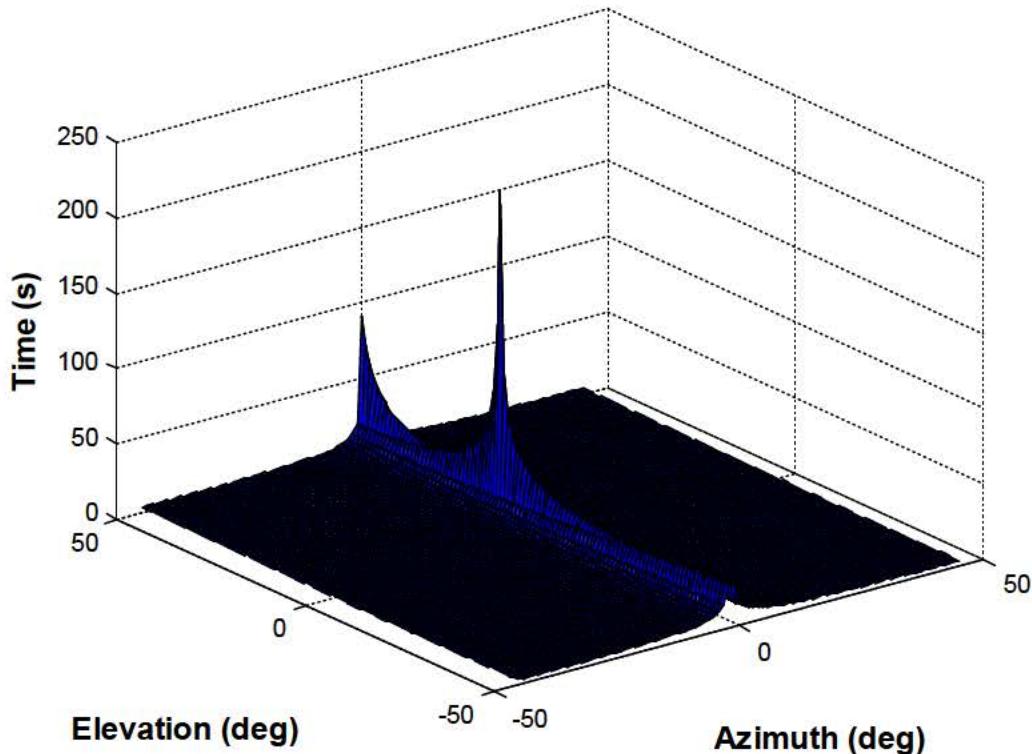


Figure 67. Time it takes to rotate around the y -axis by 0.009 arcsec for flat plate model

There is no figure for the z -axis that is because of the original assumption that the wheels can control any torque that is in the RW-plane, and all torque around the z -axis is in the reaction wheel plane and can be controlled. Another important point to make about Figure 66. and Figure 67. is that the spacecraft can maintain a pointing accuracy of less than 0.009 arcsec, for less than 10 seconds around both the x and y axes, unless the azimuth rotation is limited between ± 5 degrees. The maximum time to for Kepler to be within its design limits is about 149 seconds around the x -axis and about 219 seconds around the y -axis, both at a an attitude of $(Az, El) = (-1, 12)^\circ$. Furthermore, the analysis examines the x and y axes as if they cannot be controlled to see the impact of the drift in both directions.

The Kepler spacecraft functions with using a CCD where each pixel is read after the integration time of 6.54 seconds. These integration times are then combined into two different types of photometric targets referred to as short cadence, SC, and long cadence,

LC. An SC consists of at least 7 integration times with the default set for 9 for a total of 58.8 seconds while an LC is at least 15 SC's, but by default 30 SC's for a total of about 30 minutes [3]. Therefore, based on the controllability analysis most orientations would not be sufficient for even a SC and even the best orientation is not sufficient for the LC. This simple analysis seems to indicate that the Kepler spacecraft cannot meet its original mission requirements, using two reaction wheels.

B. VALIDATING RESULTS

It is beneficial before further analysis is conducted to confirm that the SRP flat plate model provides similar results to the model developed by Ball. This comparison was conducted by running the same controllability analysis on the Ball model as was done on the flat plate model, with the results shown in Figure 68. and Figure 69..

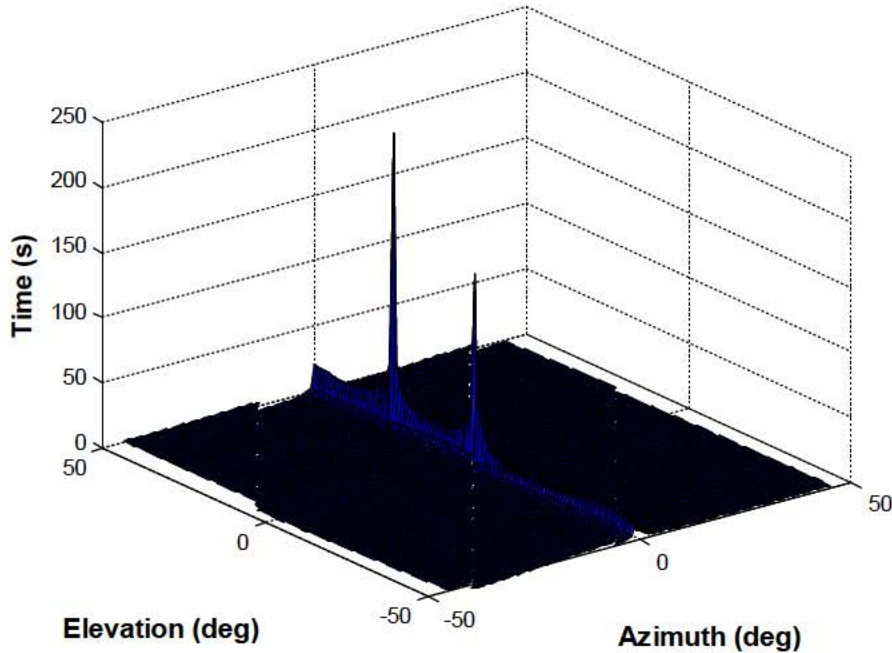


Figure 68. Time it takes to rotate around the x -axis by 0.009 arcsec for Ball model

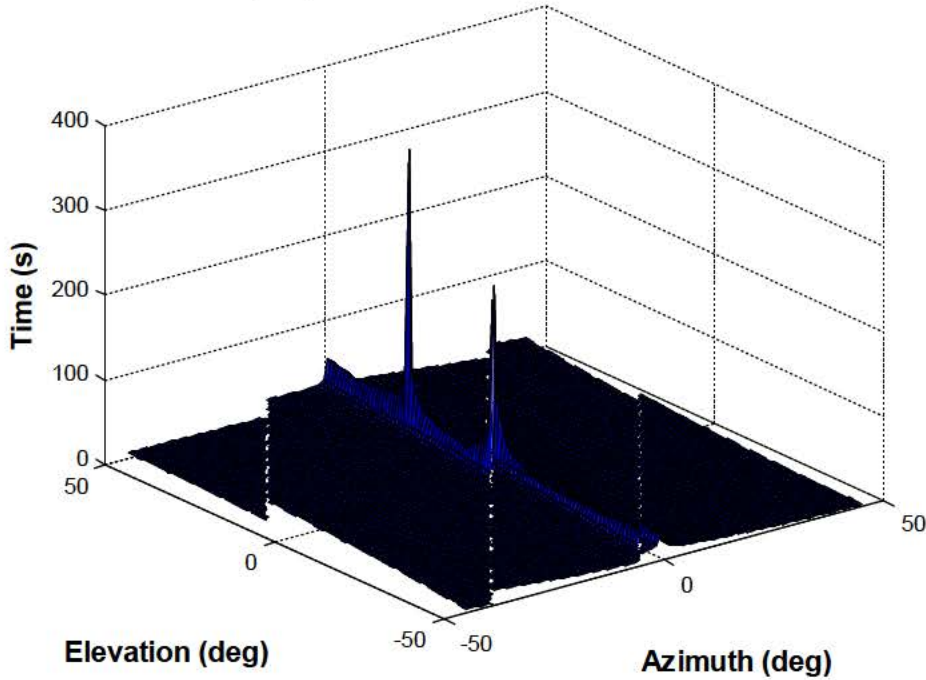


Figure 69. Time it takes to rotate around the y -axis by 0.009 arcsec for Ball model

As expected the rotation around the z -axis is zero like the flat plate model. Also the overall results from the x and y axes are very similar, besides for a very small set of azimuth angles the spacecraft cannot maintain pointing accuracy for very long. The difference is that the maximum values are a bit longer for the Ball model and with a slightly different orientation; for the x -axis the Ball model a maximum of about 228 seconds and for the y -axis about 338 seconds both with the orientation of $(Az, El) = (0, 26)^\circ$. Although the maximums are a bit higher they are not significantly higher, so the flat plate model is sufficient to provide a good estimate of the pointing performance of the failed spacecraft.

C. FURTHER ANALYSIS

It also useful to determine the maximum pointing error for a SC and a LC; this information will be useful in determining what kind of science maybe obtained with the degraded system. This analysis requires the use of (110), and for the times 58.8s will be

used for SC and 1800s will be used for the LC. The results are summarized in Figure 70. , Figure 71. , Figure 72. , Figure 73. and Table 11. .

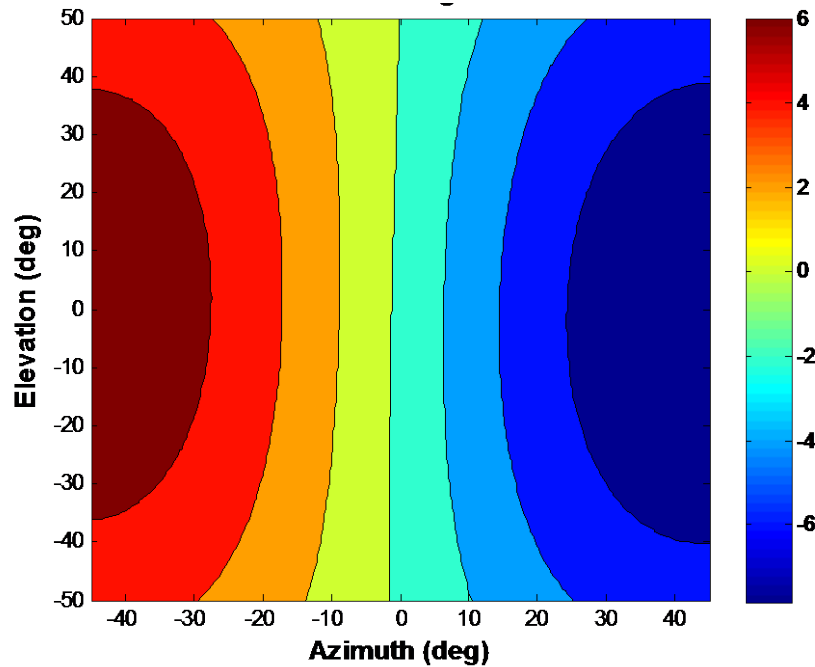


Figure 70. Pointing error around x -axis for SC (arcsec)

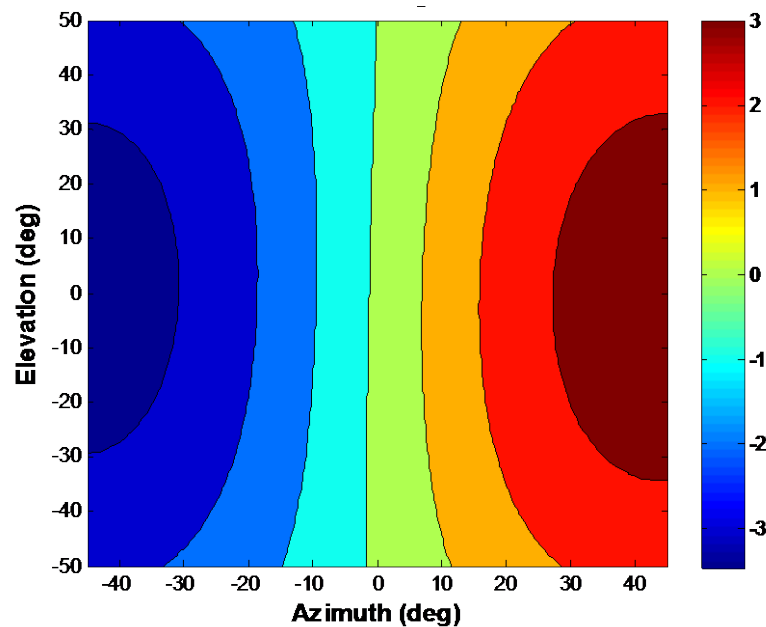


Figure 71. Pointing error around y -axis for SC (arcsec)

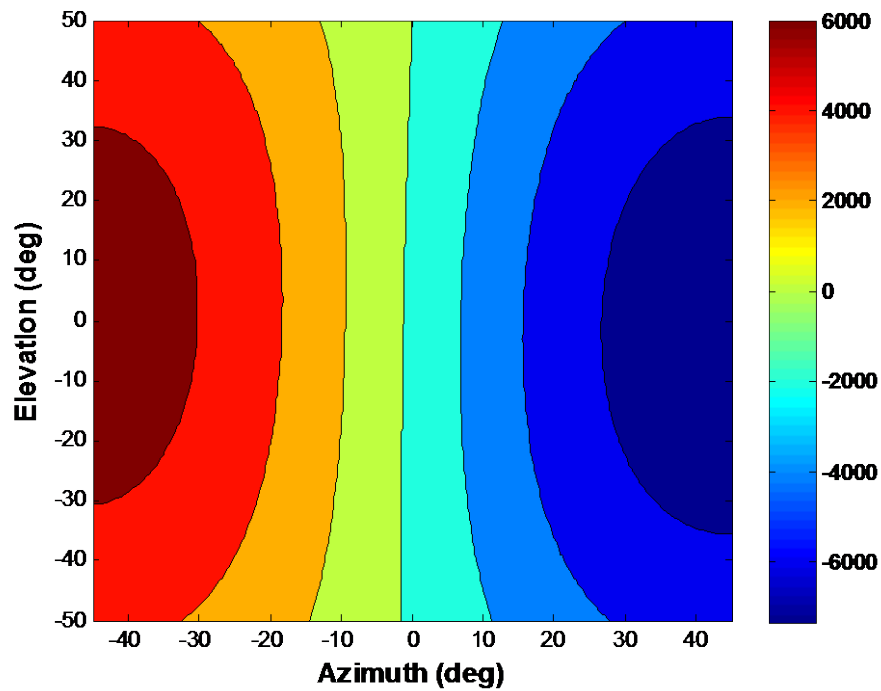


Figure 72. Pointing error around x -axis for LC (arcsec)

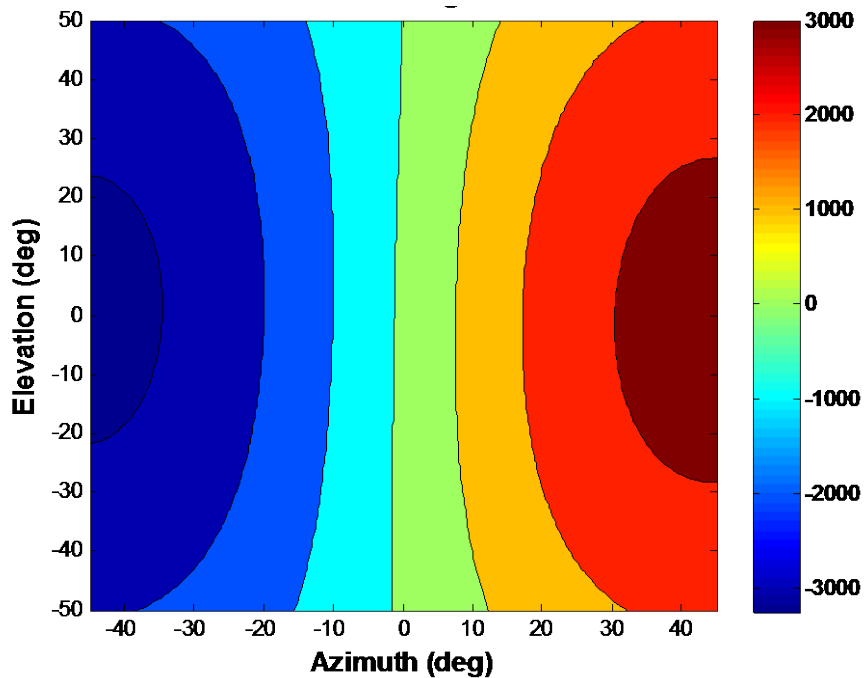


Figure 73. Pointing error around y -axis for LC (arcsec)

Table 11. Uncontrolled pointing errors for short and long cadences

Target Type	Maximum		Minimum	
	Rotation (Az,El)	Pointing Error (arcsec)	Rotation (Az,El)	Pointing Error (arcsec)
SC x-axis	(45,-1) $^{\circ}$	-7.8	(-1,12) $^{\circ}$	-1.4x10 $^{-3}$
LC x-axis	(45,-1) $^{\circ}$	-7325	(-1,12) $^{\circ}$	-1.34
SC y-axis	(45,-1) $^{\circ}$	3.6	(-1,12) $^{\circ}$	6.6x10 $^{-4}$
LC y-axis	(45,-1) $^{\circ}$	3390	(-1,12) $^{\circ}$	0.62

Similar to above, the information about the z -axis is such that there is no pointing error, so those figures were omitted. As expected the y -axis performed better, it had lower pointing errors. This was predicted by the previous analysis where the y -axis maintains pointing accuracy for longer.

As explained in IV.C.b.3 the pointing noise contributed by pointing error around the y -axis is almost 100 times worse than that contributed by the x -axis. Therefore, since the effects of the x -axis pointing error is similar to the y -axis pointing error, if both the y -axis and x -axis remain uncontrolled than the y -axis is the limiting case. However, the reaction wheels can control torque that is in the plane, so the reaction wheels can be used to control torque around the z -axis and one other axis. In the case of K2 it was decided to control around the y -axis and z -axis, while leaving the x -axis uncontrolled [13]. Ideally, the second axis is the one that would provide the worst pointing noise. Using (50), but dividing by two to remove the effects of z -axis rotations, it is simple to identify, which pointing error will be worse:

$$\eta = \frac{1}{2} \left(\frac{f\Delta\theta}{d\Delta\phi} \right)^2 = \frac{1}{2} \left(\frac{1399.20(0.62)}{150(1.34)} \right)^2 = 9.3 \quad (112)$$

The pointing noise due to rotations around the y -axis is about an order of magnitude greater than the pointing noise due to rotations around the x -axis. Therefore, it is preferable to make the second axis of control the y -axis. This effectively makes the y -axis drift negligible and makes the x -axis pointing error the limiting case.

The K2 mission uses a hybrid control technique with a momentum bias [13] and to reduce the x -axis pointing error. Momentum biasing is accomplished by evenly loading momentum “onto the two wheels to gyroscopically stabilize the third axis” [13]. Using

momentum biasing it is assumed that the angular rate around the y -axis and z -axis are minimal and can be ignored but leads to a different equation for computing the angular rate around the x -axis [57]:

$$\omega_x = \frac{bT_{s,x} - aT_{s,y}}{2ach} \quad (113)$$

where the constants are listed in Table 12. and the solar torque values are the same values that are used in the uncontrolled analysis.

Table 12. Constants needed for momentum bias angular rate estimate

a	b	c	\bar{h} (Nms)
0.574	0.485	0.660	15

Integrating (113) with respect to time provides a new equation for the pointing error, under momentum bias:

$$\theta(t) = \omega_x t \quad (114)$$

Using (114) it is possible to perform the same analysis on the momentum bias situation for the SC, and LC integration times as was performed for the uncontrolled situation. The results are shown in Figure 74., Figure 75. and summarized in Table 13. .

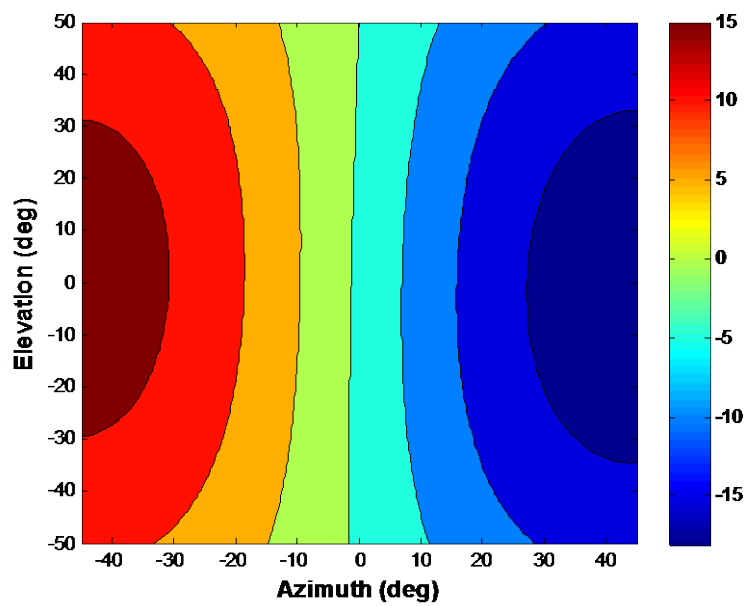


Figure 74. Pointing error around x -axis for SC using momentum bias, (arcsec)

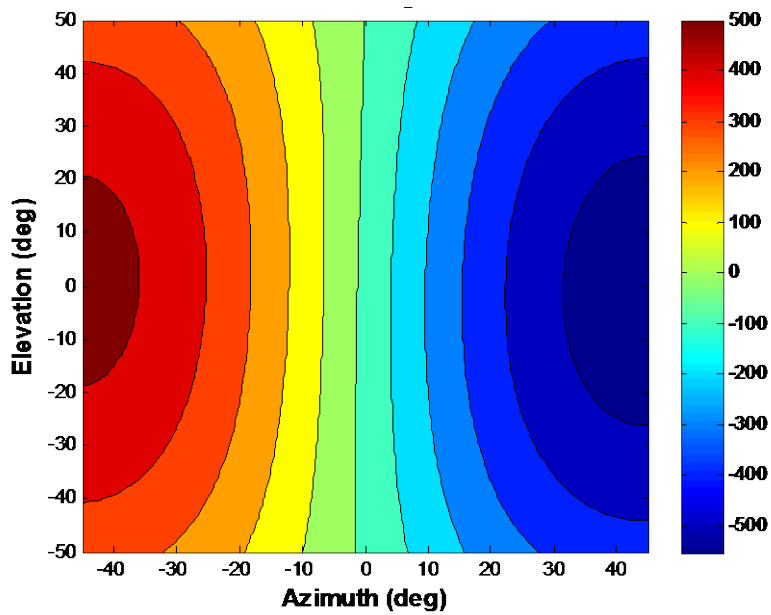


Figure 75. Pointing error around x -axis for LC using momentum bias, (arcsec)

Table 13. Significant results for pointing error using momentum bias

Target Type	Maximum		Minimum	
	Orientation (Az,El)	Pointing Error (arcsec)	Orientation (Az,El)	Pointing Error (arcsec)
SC x-axis	(45,-1) $^{\circ}$	-18	(-1,12) $^{\circ}$	-0.0032
LC x-axis	(45,-1) $^{\circ}$	-554	(-1,12) $^{\circ}$	-0.098

There are a few interesting things to note in a comparison between the results of the uncontrolled system to the control method using momentum bias. The SC integration time pointing errors are worse for the momentum bias. This is expected because in the case of momentum bias there is an initial angular rate around the x -axis that was assumed to be zero in the uncontrolled system. Ultimately, though the momentum bias shows significant improvements over the uncontrolled system; it is about one order of magnitude better using the hybrid control with momentum bias.

One more important thing to mention is that the results using the flat plate model are better than the average minimum drift provided by Ball of about 0.63 arcsec for a 30 minute period [13]. Differences are expected because the flat plate SRP provides similar but not identical results as the Ball model. In addition, the momentum bias used in this thesis was assumed to remain constant throughout the whole 30 minute time period, but the momentum bias actually reduces as a function of time and slowly changes during the 30 minute time period.

D. POSSIBLE SCIENCE

The analysis of the drift characteristics of the wheels is only important if it is related back to the science requirements discussed in the previous chapter. Figure 76. , uses the minimum pointing errors around the x -axis, provided in Table 11. and Table 13. to add a third and fourth curve to Figure 29. . The third curve depicts the minimum size planet detectable in the uncontrolled system, whereas the fourth curve represents what is possible using momentum bias analysis.

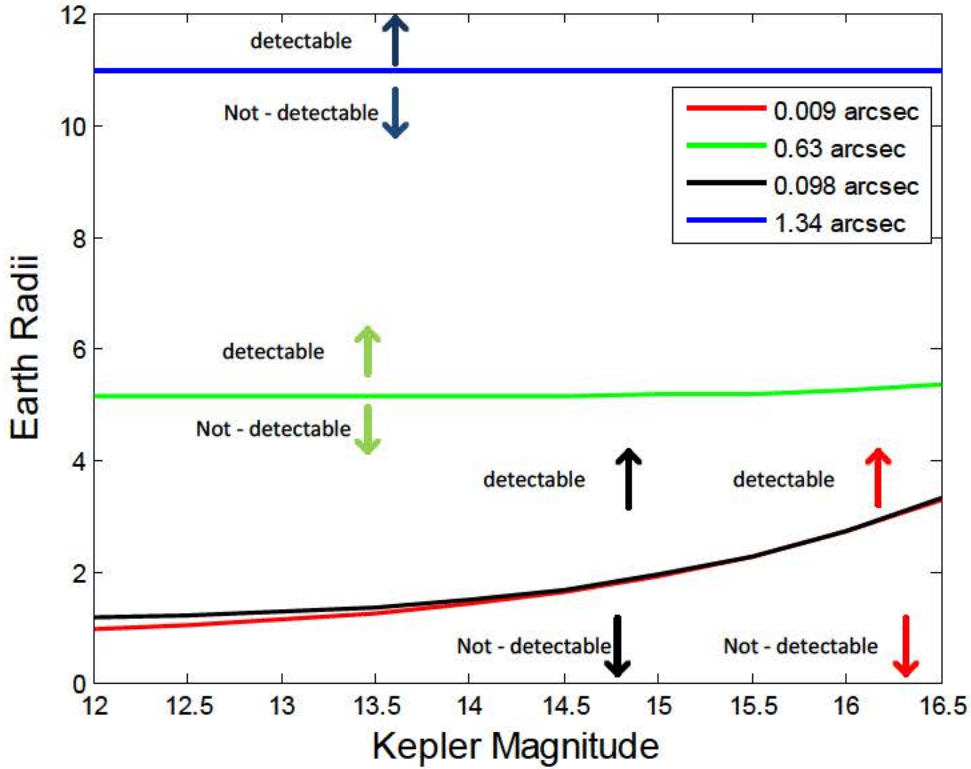


Figure 76. Possible planet detection ability with drift rates per LC for Case 1, Case 3, uncontrolled and momentum bias with flat plate model

The blue curve is based on the pointing error in the scenario where only the y -axis and z -axis are controlled and the x -axis is allowed to rotate uncontrolled with zero momentum bias. The minimum detectable planet is about $11R_{\oplus}$ or about the size of Jupiter; in this scenario Kepler provides an ability equivalent to ground systems to detecting planets [18], which calls into question the need to continue operating the system. It is clear from Figure 76. that in order to conduct science on par with the original Kepler mission allowing the x -axis to rotate uncontrolled is insufficient. The green curve and the black curve represent pointing error based on a hybrid control schema with momentum bias. The green curve as explained earlier is based on Ball's model and the analysis of reference [13]. The black curve is based on the minimum pointing error obtained for the flat plate SRP model using momentum bias. The black curve makes it seem possible to return to the original Kepler mission. However, similar to

Ball's model, this requires Kepler to point in the ecliptic. It is not possible to point at the original target between Cygnus and Lyra and continue science operations.

Finally, Figure 30. can be redone using the results of the momentum bias analysis as shown in Figure 77. . The uncontrolled case is not included because it provides a pointing noise around 2500ppm and would make the other information unreadable. This also reinforces the need for unique engineering solutions like momentum bias to be able to make good use of Kepler.

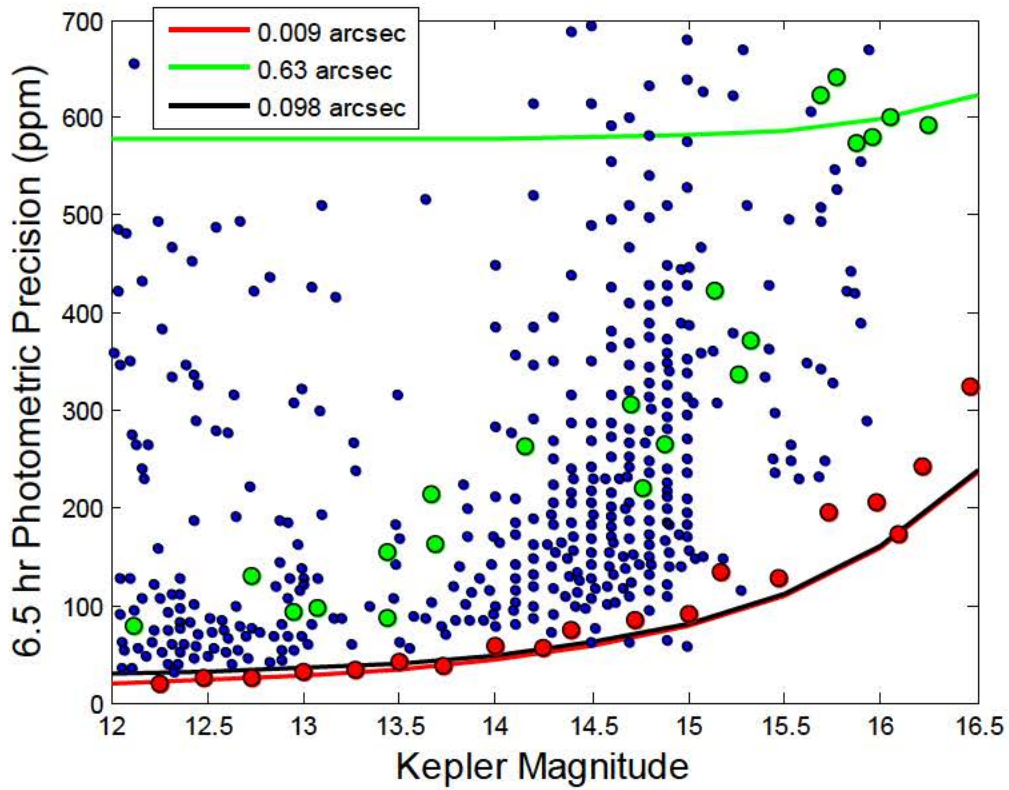


Figure 77. Predicted photometric precision with momentum bias curve vs. actual data, after [46]

Figure 77 shows that the analysis presented in this thesis has allowed reasonable bounds on the expected performance of the K2 mission to be determined. Moreover, these are consistent with the data obtained early in the K2 mission checkout.

E. SUMMARY

The flat plate model provided sufficient results to begin analyzing the ability of Kepler to maintain its original pointing accuracy requirements. Unfortunately, based on the original analysis, with only two reaction wheels it does not seem possible for Kepler to return to its original mission since the pointing error is now much greater than desired. The flat plate model demonstrated that Kepler is more prone to rotate around the x -axis and in an uncontrolled situation it was clear that Kepler could not return to its original mission and is not necessarily better than ground systems with regards to finding planets. Subsequent analysis added momentum bias to the flat plate model drift characteristic analysis to demonstrate the advantages provided by this control technique. The results were promising; Kepler may not be able to return to its original orientation, but it may still be able to detect Earth-size planets if the science field of view is properly chosen. One limitation to be aware of for Case 3 and the momentum bias, is both scenarios assume that the pointing error is similar for every 30 minute period and does not account for the errors that can occur when the target star drifts across pixels. The results may be overly optimistic and do not necessarily provide the ability to stare at one point in the celestial sky for a 6.5hr period to detect a planet transit. Case 3 and the flat plate momentum bias results provide an upper and lower bound and give a fairly good approximation of Kepler's current capabilities.

VIII. CONCLUSION

This thesis had two main objectives: to describe the physics behind Kepler's ability to detect planets and to develop a solar radiation pressure, SRP, model that could be used to illustrate why the original Kepler mission is no longer possible. Both of these objectives were sufficiently met, in addition, through the study of these objectives this thesis was able to bridge the gap between science requirements and engineering requirements.

The first objective was accomplished by providing an understanding of planets and star classification, an understanding of the different planet detection methods and a greater explanation of the transit method used by Kepler. Also, the photometric precision was explained in terms of various noise terms. The equations developed were then used to give a simple analysis of the possible science during the original Kepler mission and for the K2 mission.

The second part of the thesis focused on developing a simple solar torque model for Kepler. The SRP model was used to illustrate the effects of solar torque on pointing error. Using the flat plate SRP model it was shown that returning to the original Kepler mission is not possible, and showed the need for the hybrid control provided for the K2 mission over the uncontrolled scenario analyzed in this thesis.

One area of this work that could be improved upon is the model of photometric precision. A useful next step would be to develop a photometer numeric simulation for Kepler. This would make the pointing noise to be more precisely analyzed so that a greater correlation to K2 mission results could be obtained. A second area of research that would further the work of this thesis would be to use the developed flat plate SRP model and test it using different control mechanisms in the hopes of further improving pointing accuracy beyond hybrid control. This may also provide a better understanding of the difference in the results between the momentum bias when applied to the flat plate SRP model versus the Ball predicted results. The K2 mission focuses on the ecliptic and the hybrid architecture seems to be supporting the ability to perform the science objective.

However, there may be other unique control solutions that make areas of the celestial sky besides the ecliptic possible, for science activities.

LIST OF REFERENCES

- [1] NASA Discovery Program. (n. d.) NASA. [Online]. Available: <http://discovery.nasa.gov/program.cfm>. Accessed Oct. 3, 2014.
- [2] D. Koch *et al.* “Kepler: a space mission to detect earth-class exoplanets,” in *Proc. SPIE, Space Telescopes and Instruments V*, 1998, vol. 3356, pp. 599–607. doi:10.1117/12.324482
- [3] “Kepler: A search for terrestrial planets Kepler instrument handbook,” NASA, Moffett Field, CA, Rep. KSCI-19033-001, Jul. 2009.
- [4] NASA Discovery Program - Kepler. (n. d.). NASA. [Online]. Available: <http://discovery.nasa.gov/kepler.cfm>. Accessed Oct. 3, 2014.
- [5] W. J. Borucki *et al.* “The Kepler mission: a mission to determine the frequency of inner planets near the habitable zone of a wide range of stars,” presented at ASP Conf. Ser. 119, Planets Beyond Our Solar System and Next Generation Space Missions, 1996.
- [6] Kepler launch vehicle and orbit (2013, Oct. 22). NASA Ames Research Center. [Online]. Available: <http://kepler.nasa.gov/mission/QuickGuide/missiondesign/launch/>
- [7] R. L. Gilliland *et al.* (2010 Mar. 31). Initial characteristics of Kepler short cadence data. *ApJ.* [Online]. 713(2). pp. L160–163. doi:10.1088/2041-8205/713/2/L160
- [8] Kepler a search for potentially habitable planets. (2014, Nov. 21). NASA. [Online]. Available: http://www.nasa.gov/mission_pages/kepler/main/index.html#.VHNweovF-So
- [9] NASA’s Kepler space telescope discovers its first five exoplanets.(2010 Jan., 4). NASA. [Online]. Available: http://www.nasa.gov/mission_pages/kepler/news/kepler-5-exoplanets.html
- [10] Kepler planet announcements. (2014, Oct. 3). NASA. [Online]. Available: http://www.nasa.gov/mission_pages/kepler/news/index.html#.VHNxXYvF-So

- [11] M. Johnson and J. D. Harrington. (2014, Feb. 26). NASA's Kepler mission announces a planet bonanza, 715 new worlds. [Online]. Available: <http://www.nasa.gov/ames/kepler/nasas-kepler-mission-announces-a-planet-bonanza/#.VHN2XYvF-So>
- [12] Digital press kit - Kepler planet bonanza. (2014, Feb. 26). NASA. [Online]. Available: <http://www.nasa.gov/ames/kepler/digital-press-kit-kepler-planet-bonanza/#.VHOTaovF-Sr>.
- [13] D. Putnam and D. Wiemer, "Hybrid control architecture for the Kepler spacecraft," presented at AAS 14, Breckenridge, CO, 2014.
- [14] Call for white papers: soliciting community input for alternate science investigations for the Kepler spacecraft. (2013 Aug.). NASA Ames Research Center. Moffet Field, CA. [Online]. Available: <http://keplerscience.arc.nasa.gov/docs/Kepler-2wheels-call-1.pdf>
- [15] M. Karpenko *et al.*, "Precision pointing for a skewed 2-reaction wheel control system," presented at AAS 14, Breckenridge, CO, 2014.
- [16] K2 mission concept. (2014, May 29). NASA. [Online]. Available: <http://keplerscience.arc.nasa.gov/K2/MissionConcept.shtml>
- [17] K2 science motivations and potential. (2014, May 29). NASA. [Online]. Available: <http://keplerscience.arc.nasa.gov/K2/Science.shtml>
- [18] M. Perryman, *The Exoplanet Handbook*, 1st ed. Cambridge, NY: Cambridge University Press, 2011, pp. 1–4, 103–120.
- [19] The StarChild Team. (1999 Dec.). StarChild question of the month for December 1999. NASA Goddard Spaceflight Center, [Online]. Available: <http://starchild.gsfc.nasa.gov/docs/StarChild/questions/question16.html>
- [20] Planet Quest The Search for Another Earth: Exoplanet History - From Intuition to Discovery. (n. d.) NASA JPL. [Online]. Available: <http://planetquest.jpl.nasa.gov/page/history>. Accessed Sep. 29, 2014.
- [21] Kepler A search for habitable planets. (n. d.). NASA JPL. [Online]. Available: <http://kepler.nasa.gov/>. Accessed Sep. 29, 2014.
- [22] About the IAU. (n. d.). International Astronomical Union. [Online]. Available: <http://www.iau.org/about/>. Accessed Sep. 23, 2014.

- [23] Definition of a Planet in the Solar System, Resolution B5, International Astronomical Union, Prague, 2006, pp. 1–2.
- [24] D. G. Russel. (2014 Oct. 11). Solar and extrasolar planet taxonomy. ARXIV. [Online]. pp. 1–20. <http://arxiv.org/abs/1308.0616v3>
- [25] J. H. Luscombe, *Relativity and Cosmology*, unpublished.
- [26] D. Rothstein. (2003, Sep. 18). Curious about astronomy? Ask an astronomer. What is apparent magnitude? [Online]. Available: <http://curious.astro.cornell.edu/question.php?number=569>
- [27] D. Daunt and D. Yost. Color Indices and Surface Temperatures. (n. d.) [Online]. Available: <http://csep10.phys.utk.edu/astr162/lect/stars/cindex.html>. Accessed 23 September 2014.
- [28] D. D. R. Williams. (2013, Jul. 1). Sun fact sheet [Online]. Available: <http://nssdc.gsfc.nasa.gov/planetary/factsheet/sunfact.html>
- [29] O. Struve and V. Zebergs, *Astronomy of the 20th Century*, 1st ed. New York, NY: The MacMillan Company, 1962. pp. 186–283.
- [30] T. M. Brown *et. al.* (2011, Jul. 26). Kepler input catalog: photometric calibration and stellar classification. *Astronomical J.* [Online]. 142(4). pp. 112–130, 2011. doi: 10.1088/0004–6256/142/4/112
- [31] Planet quest the search for another earth: methods. NASA JPL. [Online]. Available: <http://planetquest.jpl.nasa.gov/page/methods>. Accessed Sep. 29, 2014.
- [32] Planet quest the search for another Earth: new worlds atlas. NASA JPL. [Online]. Available: <http://planetquest.jpl.nasa.gov/newworldsatlas>. Accessed Sep. 29, 2014.
- [33] Planet quest the search for another Earth: missions. NASA JPL. [Online]. Available: <http://planetquest.jpl.nasa.gov/page/missions>. Accessed Sep. 29, 2014.
- [34] J.-W. Xie. (2013, Aug. 19). Transit timing variation of near-resonant KOI pairs: confirmation of 12 multiple planet systems. *The ApJ. Suppl.* [Online]. 208(22). pp. 1–12. doi: 10.1088/0067–0049/208/2/22

- [35] S. Faigler *et al.* (2013, May 10). BEER analysis of Kepler and CoRoT light curves: I. Discovery of Kepler-76b: a hot Jupiter with evidence for superrotation. *The ApJ*. [Online]. 771(26). pp. 1–10. doi: 10.1088/0004–637X/771/1/26.
- [36] M. Salaris and S. Cassisi, *Evolution of Stars and Stellar Populations*, 1st ed. Chichester, West Sussex, England: John Wiley & Sons, 2005, p. 138.
- [37] A. Piterman and Z. Ninkov. (2002, May 22). Subpixel sensitivity maps for a back-illuminated charge-coupled device and the effects of nonuniform response on measurement accuracy. *Opt. Eng.* [Online]. 41(6). pp. 1192–1202. doi:10.1117/1.1476691:
- [38] J. W. Goodman, *Introduction to Fourier Optics*, 2nd ed., Boston, MA: McGraw Hill, 1996, pp. 32–95.
- [39] Lens Diffraction & Photography. (2014). Cambridge in Colour. [Online]. Available: <http://www.cambridgeincolour.com/tutorials/diffraction-photography.htm>. Accessed 5 November 2014.
- [40] Q. P. Remund *et al.* (2002, Feb. 6). Kepler system numerical model for the detection of extrasolar terrestrial planets. *Proc. SPIE*. [Online]. 4995. 182–191. doi: 10.1117/12.454773.
- [41] S. T. Bryson *et al.* (2010, Mar. 24). The Kepler Pixel Response Function. *The ApJ. Lett.* [Online]. 713(2). pp. L97–102. doi: 10.1088/2041–8205/713/2/L97.
- [42] MIT: Department of Physics, “Poisson Statistics,” unpublished.
- [43] S. B. Howell, *Handbook of CCD Astronomy*, 1st ed., Cambridge, NY: Cambridge University Press, 2006.
- [44] S. L. Chuang, *Physics of Optoelectronics Devices*, 1st ed., New York, NY: Wiley-Interscience, 1995, pp. 585–593.
- [45] M. W. Smith, private communication, Nov. 2014.
- [46] K2 Performance. (2014, May 29). NASA. [Online]. Available: <http://keplerscience.arc.nasa.gov/K2/Performance.shtml>
- [47] The Kepler Mission Star Field. (n. d.). NASA. [Online]. Available: http://www.nasa.gov/pdf/189566main_Kepler_Mission.pdf. Accessed 7 December 2014.

- [48] C. N. Schira and D. S. Putnam, “Kepler ADCS Overview and Early Mission Experiences,” presented at *AAS 10*, Breckenridge, CO, 2010.
- [49] S. R. Starin and J. Eterno, “Spacecraft Attitude Determination and Control Systems,” in *Space Mission Engineering: The New SMAD*, J. R. Wertz, D. F. Everett and J. J. Puschell, Eds., Hawthorne, CA: Microcosm Press, 2011, pp. 565–591.
- [50] C. B. Spence Jr., *Spacecraft Attitude Determination and Control*, Dordrecht, The Netherlands: Kluwer Academic Publishers, 1990, pp. 566–576.
- [51] “Spacecraft radiation torques,” NASA, Washington, D. C., NASA SP-8027, Oct. 1969.
- [52] A. H. Compton, “A Quantum Theory of the Scattering of X-rays by Light Elements,” *The Physical Rev.*, vol. 21, no. 5, pp. 483–502, May 1923.
- [53] J. Morrison, *Modern Physics for Scientists and Engineers*, 1st ed., Burlington, MA: Academic Press, 2009, ch. 7, sec. 3.2, pp. 158–162.
- [54] Mathworks, *Help file on lsqnonlin*, Mathworks, 2013.
- [55] Documentation Center Choosing a Solver. (n. d.). Mathworks. [Online]. Available: <http://www.mathworks.com/help/optim/ug/choosing-a-solver.html>. [Accessed 1 October 2014].
- [56] R. Hunter. (2013, Jul. 24). Kepler mission manager update: initial recovery tests. [Online]. Available: http://www.nasa.gov/content/kepler-mission-manager-update-initial-recovery-tests/#.U_eNRPldWSO
- [57] M. Argenziano, “Optimal attitude maneuvers for the Kepler K2 mission,” M. Sc. Thesis, MAE, Naval Postgraduate School, Monterey, CA, 2014.
- [59] D. D. R. Williams. (2013, Jul. 01). Earth fact sheet. [Online]. Available: <http://nssdc.gsfc.nasa.gov/planetary/factsheet/earthfact.html>. [Accessed 5 February 2014].
- [60] V. Dhillon. (2013, Oct. 11). Astronomical techniques phy217. [Online]. Available: http://www.vikdhillon.staff.shef.ac.uk/teaching/phy217/telescopes/phy217_tel_cataadioptric.html

- [61] D. D. R. Williams. (2014, Apr. 25). Planetary fact sheet – metric. [Online]. Available: <http://nssdc.gsfc.nasa.gov/planetary/factsheet/>
- [62] Kepler mission star field. (2009, Mar. 7). NASA. [Online]. Available: http://www.nasa.gov/mission_pages/kepler/multimedia/images/kepler-field-of-view-photo.html

INITIAL DISTRIBUTION LIST

1. Defense Technical Information Center
Ft. Belvoir, Virginia
2. Dudley Knox Library
Naval Postgraduate School
Monterey, California